NASA Contractor Report 185193

Unified Aeroacoustics Analysis for High Speed Turboprop Aerodynamics and Noise

Volume III - Application of Theory for Blade Loading, Wakes, Noise, and Wing Shielding

D.B. Hanson, C.J. McColgan, R.M. Ladden, and R.J. Klatte
United Technologies Corporation
Hamilton Standard Division
Windsor Locks, Connecticut

May 1991

Prepared for
Lewis Research Center
Under Contract Number NAS3-23720

National Aeronautics and
Space Administration

(NASA-CR-185193) UNIFIED AEROACOUSTICS ANALYSIS FOR HIGH SPEED TURBOPROP AERODYNAMICS AND NOISE. VOLUME 3: APPLICATION OF THEORY FOR BLADE LOADING, WAKES, NOISE, AND WING SHIELDING Final
N91-23850
G3/71
Unclas
0013657

NASA Contractor Report 185193

Unified Aeroacoustics Analysis for High Speed Turboprop Aerodynamics and Noise

Volume III - Application of Theory for Blade Loading, Wakes, Noise, and Wing Shielding

D.B. Hanson, C.J. McColgan, R.M. Ladden, and R.J. Klatte
United Technologies Corporation
Hamilton Standard Division
Windsor Locks, Connecticut

May 1991

Prepared for
Lewis Research Center
Under Contract Number NAS3-23720

NASA
National Aeronautics and
Space Administration

TABLE OF CONTENTS

SUMMARY

This is the 3rd volume in a 5 volume report on the aerodynamics and aeroacoustics of advanced turboprops. It presents applications of theoretical methods that have been developed in other volumes as follows. Derivations of the theoretical equations for aerodynamic performance, blade loading (steady and unsteady), wakes, and noise are given in Volume I. Theory for acoustic shielding of propeller sources by a swept wing is given in Volume II and theory for acoustic shielding by a fuselage boundary layer is given in Volume V. Finally, Volume IV is the user's manual for the computer code corresponding to the theory in Volume I.

The aerodynamic and acoustic methods are based on linear pressure potential theory with corrections for non-linearity associated with axial mass flux induction and vortex lift on the blades. Aerodynamic performance theory is compared with test results by comparing performance maps for swept and unswept Prop-Fans at takeoff and cruise conditions. Predictions of power absorption at cruise Mach numbers are satisfactory over a wide range of blade angles and advance ratios. At takeoff Mach numbers, theory tends to overpredict at high loading. This indicates that refinements are needed in the non-linear modeling.

Unsteady blade loading methodology is first evaluated by comparing with standard theories for gust and plunging blade response; then cases are run to establish regimes where lift response tends to be either 2 dimensional or 3 dimensional. Theory indicates for excitations at one and two times the shaft rotation frequency that quasi-steady 3D blade loading methods should be adequate; at high frequencies the blade response becomes 2 dimensional away from the blade tips.

The wake model is a combination of equations from the 3D acceleration potential method and a 2D treatment of the blade viscous wakes. Theory is compared with wake data from 3 Prop-Fan tests with generally good results.

Noise predictions are compared with test results for straight and swept blades operating at takeoff and cruise conditions. On a harmonic directivity basis the agreement is generally good with the best correlations occurring at the highest tip relative Mach numbers.

The potential for shielding of propeller noise by the wing in a wing-mounted installation was evaluated using a new theory developed for the purpose. By exploiting wing sweep and the correct direction of rotation, it appears that reductions of a few dB can be expected. More sophisticated modeling and experimental verification are needed. Shielding of propeller noise by the fuselage boundary layer also is a significant noise reduction factor, particularly for aft-mounted installations.

SECTION 1
INTRODUCTION

This report presents results of program for the generation of a computer prediction code for noise of advanced, single rotation, turboprops (Prop-Fans) such as the SR3 model shown in Figure 1. The code is based on a linearized theory developed at Hamilton Standard in which aerodynamics and acoustics are treated as a unified process. Both steady and unsteady blade loading are treated. Capabilities include prediction of steady airload distributions and associated aerodynamic performance, unsteady blade pressure response to gust interaction or blade vibration, noise fields associated with thickness and steady and unsteady loading, and wake velocity fields associated with steady loading. The code was developed on the Hamilton Standard IBM computer and has now been installed on the Cray XMP at NASA-Lewis.

The work had its genesis in the frequency domain acoustic theory developed at Hamilton Standard (refs. 1,2,3) in the late 1970's. It was found that the method used for near field noise predictions could be adapted as a lifting surface theory (ref. 4) for aerodynamic work via the pressure potential (or acceleration potential) technique that has been used for both wings and ducted turbomachinery. In the first realization of the theory for propellers (prior to the contract), the blade loading was represented in a quasi-vortex lattice form (ref. 5). Under the contract, this was upgraded to true lifting surface loading. Originally, it was believed that a purely linear approach for both aerodynamics and noise would be adequate. However, in the course of the contract, two sources of non-linearity in the steady aerodynamics became apparent and were found to be a significant factor at takeoff conditions. The first is related to the fact that the steady axial induced velocity may be of the same order of magnitude as the flight speed and the second is the formation of leading edge vortices which increase lift and redistribute loading. The contract was amended to deal with both of these phenomena. Discovery and properties of Prop-Fan leading edge vortices were reported in 2 technical papers during the contract effort (refs.6,7).

The final report is divided into 5 volumes as outlined in the Abstract. In Volume I, the theory for blade loading, wakes, and noise is derived from the linear wave equation with monopole and dipole source terms to represent the blade thickness and loading effects. The derivation is complete down to working formulas. The formulas are coded in a computer program called UAAP (for Unified AeroAcoustic Program). Volume IV is the user's manual. The subjects of the present volume (Volume III) are demonstration of the UAAP capabilities and verification of the theory by comparison of predictions from UAAP with data from tests at NASA-Lewis and the United Technologies Research Center. Separate sections are devoted to steady aerodynamic performance, unsteady blade loading, wakes, noise, and wing and boundary layer shielding.

SECTION 2

BACKGROUND

This section reviews the analytical methods used for predictions and shows how the loading, wake, and noise calculations are connected. Complete details of the theory are given in Volume I of this report including the derivation from fundamentals. However, since the derivation is lengthy, the summary below is presented to help understand the results of this volume.

The UAAP code performs 4 distinct aero/acoustic computational functions: aerodynamic blade loading (steady or unsteady), propeller performance, wakes, and noise. General output and input requirements are outlined in the table below.

INPUT AND OUTPUT OF CODE COMPONENTS

CODE	INPUT	OUTPUT
AERO LOADING	-BLADE GEOMETRY -OPERATING CONDITION -(Unsteady Boundary conditions)	-LIFT DISTRIBUTION -Steady (or Unsteady) -PROFILE DRAG
STEADY PERFORMANCE	-LIFT DISTRIBUTION -PROFILE DRAG -OPERATING CONDITION	-INDUCED DRAG -WAVE DRAG -THRUST DISTRIBUTION -TORQUE DISTRIBUTION -EFFICIENCY
FLOW FIELDS	-LIFT DISTRIBUTION -DRAG DISTRIBUTION -OPERATING CONDITION	-3 VELOCITY COMPONENTS (upstream or downstream)
NOISE	-LIFT DISTRIBUTION -DRAG DISTRIBUTION -OPERATING CONDITION	-SPECTRA -DIRECTIVITY -DIAGNOSTICS

The fundamental role of a lifting surface calculation is to establish the distribution of lift pressure over the blade surface. This is needed as input to any performance, noise, or wake calculation. Boundary conditions are input to the loading program in terms of the camber surface definition and twist distribution for steady loading calculations or in terms of blade motion or gust input (unsteady upwash) for unsteady calculations. More details on each type of calculation are given in succeeding sections of this report.

In outline, the theoretical development in Volume I is as follows. The starting point is the linear wave equation

$$\nabla^2 p - \frac{1}{c_o^2}\frac{\partial^2 p}{\partial t^2} = -\rho_o \frac{\partial q}{\partial t} + \nabla \cdot \underline{f} \qquad (2.1)$$

in which the left side is the wave operator acting on the pressure disturbance p and the right side is the source representation. Also, q is the monopole (volume injection) source strength used to represent the blade thickness effect and $\underline{f}$ is the force per unit volume acting on the fluid and is used to represent the blade loading. In the modeling, the volume sources act on the advance helicoid rather than on the actual camber surface. This amounts to linearizing the boundary conditions. If it is assumed that the source strengths are known on the blade surface, Equation 2.1 can be solved for the pressure anywhere in the field by a Green's function integral. The result can be expressed in generalized form as the sum of the loading and thickness effects:

$$p = p_L + p_T \tag{2.2}$$

where

$$p_L = \int \Delta C_p \, K_{pL} \, dA \tag{2.3}$$

and

$$p_T = \int \frac{h}{b} \, K_{pT} \, dA \tag{2.4}$$

Equations 2.3 and 2.4 are general forms of the radiation formulas for near or far field noise. The first simply states that the pressure disturbance due to loading can be represented as a linear sum (via the integral) of contributions from each element of blade area. ΔC_p is the coefficient of lift pressure and K_{pL} is the loading noise weighting function (or kernel function) that results from the Green's function integration. Similar remarks apply to Equation 2.4 for the thickness effect where h/b is the thickness source defined here in terms of blade chord b and h, the distribution of thickness over chord and span.

Since the thickness is known from geometry, Equation 2.4 can be solved directly. However, Equation 2.3 requires that the loading distribution be known or estimated. Aerodynamic loading is computed by an inversion of the equation via the acceleration potential method as follows. The acceleration potential is defined as

$$\psi(x,r,\phi,t) = \frac{-1}{\rho_o} \, p(x,r,\phi,t) \tag{2.5}$$

where ρ_o is the ambient density. This is converted into the velocity potential by integrating from upstream infinity along undisturbed streamlines according to a recipe given, for example, by Bisplinghoff, Ashley, and Halfman (ref. 8). The velocity potential can be differentiated in any direction to find the corresponding velocity component, again provided that the loading is known or estimated. In particular, differentiation normal to the blade helicoidal surfaces gives the upwash velocity w_L in the following form for the loading effect

$$w_L = \int \Delta C_p \, K_L \, dA \tag{2.6}$$

where K_L is the loading kernel function. Note that w_L is steady for performance calculations and unsteady for gust interaction or blade vibration problems. To invert this, the loading is expressed in discretized form as

$$\Delta C_p = \sum_{\nu} L_\nu \, S_\nu \tag{2.7}$$

where S_ν is a series of prescribed shape functions (defined in Section III) for loading and the L_ν's are their coefficients, which have to be found. When Equation 2.7 is inserted into Equation 2.6, the result is

$$w_L = \int \sum_{\nu} L_\nu \, S_\nu \, K_L \, dA \tag{2.8}$$

A critical step is moving the integral under the sum as follows

$$w_L = \sum_{\nu} L_\nu \int S_\nu \, K_L \, dA \tag{2.9}$$

Since the shape functions and the kernel function are known, the integrals can be evaluated without knowing the loading. If the integrals are performed for specific field points (or control points) on the blade surface counted by μ, they are functions of both the mode index ν and the control point index μ

$$K_{\mu\nu} = \int S_\nu \, K_L \, dA \tag{2.10}$$

converting Equation 2.9 into a matrix equation

$$W_\mu = \sum_{\nu} L_\nu \, K_{\mu\nu} \tag{2.11}$$

Control points are placed at strategic locations on the blade surface and it is arranged so that the number of loading modes equals the number of control points so that the matrix equation can be inverted

$$L_\nu = \sum_{\mu} K^{-1}_{\mu\nu} \, W_\mu \tag{2.12}$$

The boundary conditions are evaluated at the control points, giving the W's. The loading coefficients, L_ν, are computed from Equation 2.12. These are used with

Equation 2.7 to find the lift pressure. Given the lift pressure, formulas in the form of Equations 2.3 and 2.4 can be used to compute the acoustic pressure field.

SECTION 3
STEADY AERODYNAMIC PERFORMANCE COMPARISONS

This section presents a comparison of theoretical predictions of shaft power coefficient with measurements from wind tunnel experiments. Propellers with straight blades (SR-2) and swept blades (SR-3) are included at cruise Mach number (0.80) and takeoff Mach number (0.27). Sample curves show the contributions to shaft power of the non-linear effects of axial induction and vortex loading.

Overview of Aerodynamic Performance Method

Calculations of steady aerodynamic performance are made as follows. The blade is divided into panels as shown in Figure 2, each tapered at constant percent chord. The code will run from 2 to 20 panels; 10 were used for the calculations presented herein. Control points were placed in the centers of the panels at 8 radial stations: r/R=.20, .35, .45, .55, .65, .75, .85, and .95. The .20 station is inside the actual hub radius and was used to approximate image sources for smooth results in the root area since the centerbody is not represented explicitly. With control points at 8 radii, the spanwise loading is represented by an 8 term series of mode shapes having the general appearance shown at the top right of Figure 2. Chordwise loading is represented by 10 overlapping triangular pressure functions as shown at the lower left. The number 1 pressure panel has a square root singularity as suggested in the figure to give the correct mathematical behavior at the leading edge. Predicted distributions of lift pressure are given by the sum of the modal values as shown at the lower right in Figure 2.

For the specified paneling layout and operating condition, the matrix of influence coefficients (kernel matrix) is computed as in Equation 2.10. The elements give the downwash at each control point for each loading mode, assuming unit amplitude. Thus, if the loading were known, the downwash could be computed from Equation 2.11. However, it is the downwash that is known from the boundary conditions so that the loading is found from the inverse matrix as in Equation 2.12. Elements of the inverse matrix give the mode contribution for unit downwash at each control point.

Downwash is given by consideration of boundary conditions as shown in Figure 3. For flow tangency, the flow angle must match the angle of the blade camber surface at each of the control points (80 in this case). As indicated by the triangles in Figure 3, the flow angle is made up of the advance angle ϕ_o, any blockage caused by the centerbody and blade thickness, and the turning due to blade loading. Of these, the advance angle is given by the advance ratio and radius, the centerbody blockage is computed via a separate axisymmetric streamline program, and the blockage due to blade thickness is computed from formulas given in Volume I, Section 10 of this report. It is the remaining angle α_L that is produced by the loading and computed from Equations 2.11 and 2.7.

Distributions of lift pressure are considered to act normal to the local helical advance direction, that is, normal to the ϕ_o direction in Figure 3. This is the convention in wing lifting surface theories and is different from lifting line theories where the equivalent 2D lift vector is tilted back by the 3D induction angle. Lift pressure is integrated chordwise to find lift coefficient as a function

of radius. Then drag is accounted for in 3 components as follows. Profile drag is looked up in tables of experimental airfoil data using simple sweep theory to adjust camber, thickness ratio, and Mach number to equivalent 2D values. Drag coefficient is read out as a function of computed lift from the 3D calculation described above. Induced drag (or vortex drag or drag-due-to-lift) is computed in the Trefftz plane, or far wake, by computing the energy per unit length of wake from the lifting surface theory as described in Volume I, Section 11 of this report. Finally, wave drag is accounted for by computing the acoustic energy radiated as explained in Volume I, Sections 6 and 11. For a Prop-Fan at 80% efficiency in cruise, the 20 points that are lost are typically about 16 to vortex drag, 4 to profile effects, and about 0.1 to 0.5 to wave energy.

Calculations up to this point are based strictly on linear theory. However, modifications are included to deal with 2 aspects of non-linearity. First, the above calculation procedure is placed in the iteration loop shown in Figure 4 which is designed so that the axial momentum equation is satisfied at each radial station on a circumferentially averaged basis. This is described in Volume I, Section 11.

The second aspect of non-linearity treated is vortex loading. This is done as a direct adaptation of wing methods for leading edge and tip edge vortices as suggested in Figure 5. The sketch at the top shows the leading edge vortex which forms in the presence of sweep, relatively sharp leading edges, and high leading edge loading. Leading edge flow separates and reattaches producing a vortex. Reduced pressure associated with the vortex acting on the blade surface produces the extra lift known as vortex lift. A powerful method of computing the lift was developed by Polhamus (ref. 9) based on his "suction analogy". The principle is that the lift distribution is computed first with a potential method assuming that the flow is fully attached. Results are used to compute the leading edge thrust or suction. Then, it is recognized that with separated leading edge flow, the thrust cannot be supported. However, the critical assumption of the theory is that the thrust reorients and acts at the same strength in the lift direction as shown in the sketch at the top right in Figure 5. More detail on the treatment of vortex loading is given in the appendix, Section 9.

Lamar (ref. 10) extended Polhamus' suction analogy to deal with the tip edge flow shown in the middle sketch in Figure 5. Flow around the tip edge, if attached, produces a spanwise suction due to the centrifugal acceleration. With thin tip sections, this flow will typically separate and reattach producing extra lift as sketched at the middle right in the figure. As with the leading edge suction analogy, Lamar's method assumes that the magnitude of the extra lift is equal to the strength of the spanwise suction force that would be computed with an attached flow method. Lamar also developed the idea of augmented lift (ref. 11) shown at the bottom in Figure 5. Here it is recognized for wings with finite tip chord (as opposed to delta wings) that the vortex that is formed at the leading edge produces lift not only along the leading edge but also as it passes over the tip chord. The extra lift produced along the tip chord is Lamar's augmented lift.

Leading edge and tip edge suction are computed from the loading in the final iteration of the attached flow computation as described above in conjunction with Figure 4. Then each of the vortex loading elements is computed by adapting methods directly from the Polhamus and Lamar references. The suction analogy computes the distribution of leading edge vortex loading along the radius; it does not give guidance as to the distribution of this lift component along the chord. This is handled in the UAAP computer program with distribution functions derived based on early Prop-Fan flow visualization results. Similarly, the suction analogy computes

the distribution of side edge force along the tip edge but does not give the spanwise distribution of this component. This too is handled in the code via empirically derived shape functions.

Vortex loading is computed after the axial momentum loop in Figure 4 is converged. This feature is a direct mimic of the wing methodology. Since the code does not currently recognize that vortex loading will produce extra axial induction, the axial momentum/thrust balance is not maintained and blade loading is overpredicted. This problem does not occur in wing methods since wings do not produce axial induction. Computations described below indicate the magnitude of the problem and suggest that vortex loading should be brought inside the axial momentum loop.

Computed Results

This section presents comparisons of predicted and test power absorption for Prop-Fans with swept and unswept blades at simulated flight Mach numbers typical of cruise and takeoff. Cruise Mach numbers are of interest because they include the design condition where blade loading should be ideal. In particular, the leading edge incidence should be such as to produce little vortex flow. Of course, tip edge vortices are inevitable for loaded blades. The takeoff condition is very highly loaded and significant leading edge vortex loading is expected. Test conditions and the associated figures are given in the table below. Data are from wind tunnels at NASA Lewis and United Technologies Research Center

Tunnel Speed	SR2 (Unswept)	SR3 (Swept)
M=0.80	Figs 6 & 7	Figs 8 & 9
M=0.27	Figs 10 & 11	Figs 12 & 13

The test curves in Figure 6 give the power absorption for SR2 at M=0.80 as measured during the testing reported in Reference 12. (The data shown were not reported in the referenced report but were supplied in a private communication from R. J. Jeracki of NASA Lewis.) Each of the 4 curves shown at the bottom represents the increase of power with decreasing advance ratio (or increasing RPM) at constant blade angle. The corresponding predictions match very well, particularly at the high RPM end of the curves. Toward the low power end, the predictions are somewhat high, but only by the equivalent of a fraction of a degree in blade angle. Figure 7 repeats the prediction for 59 degrees blade angle (the upper theoretical curve) and also shows the prediction without non-linear effects (the lower curve). It can be seen that non-linear axial induction and vortex loading are very small factors for SR2 near the design point.

Figure 8 shows results for SR3 at M=0.80 plotted on a figure from Reference 13. The agreement is similar in form to that for SR2 except that the blade angle - power correspondence is not as good. The theoretical curves were run with an approximate accounting for blade flexibility. A NASTRAN calculation at the design condition gave the blade twist due to centrifugal force effects. Input data sets were formed by interpolating between the static blade and the deflected blade with a square law relationship for RPM. Camber effects and airloads were not included. The extra twist at the design point is computed to be 1.7 degrees at the 0.75 radius. How-

ever, the power curves are still off by the equivalent of approximately 2 degrees in blade angle. This is caused, at least in part, by flexibility in the blade retention system. Blades are geared to change pitch together by a pin/ring gear system inside the hub. This is known to be flexible; in fact, the pins and gear yielded during some of the tests. Analysis of the retention component flexibilities indicates a maximum blade angle reduction at the design point of 2.5 degrees for a zero friction system. With realistic friction, the pitch reduction is estimated to be 1 to 1.5 degrees. Considering the system flexibility and the uncertainty in its calculation, the agreement shown in Figure 8 is satisfactory. This figure does, however, point out the need for accurate deflected geometry definition for further verification of theoretical codes.

Figure 9 shows the non-linearity contributions for SR3 at M=0.80. Non-linearity in axial induction is seen to be small, as it was with SR2. However, vortex loading is more significant at the high power end of the curves.

The remaining curves in this section deal with the data at a takeoff or climb Mach number of 0.27 with data from Reference 14. The SR2 predictions in Figure 10 show good power tracking at low loading but, at the higher powers, there tends to be a significant over-prediction. This is believed to be caused by the fact that the thrust associated with vortex loading is not included in the thrust/axial momentum iteration loop, as was discussed above. Figure 11 shows the non-linearity contributions. It can be seen that the power tracking was good with axial momentum properly balanced (middle curve) but that vortex loading added by postprocessing outside the axial momentum loop caused the over-prediction.

Figures 12 and 13 show similar results for SR3. The vortex loading effect is stronger because of sweep. Hence, the overprediction is more than for unswept SR-2.

SECTION 4
UNSTEADY AERODYNAMIC LOADING STUDY

The general aerodynamic loading theory derived in Volume I of this report deals with both steady and unsteady boundary conditions. Thus, in Equation 2.12 of the present volume, the downwash vector W_μ can be real or complex. Real downwash represents constant conditions at the control points; complex values represent the amplitude and phase of the unsteady downwash at a specified frequency. The frequency can be any integer or non-integer multiple of the shaft rotation frequency. Conditions on different blades are assumed to be identical except for a phase difference specified by a variable k that can be interpreted as the number of nodal diameters (or cycles in the circumferential direction at any time) of the motion and loading pattern. k also gives the interblade phase angle as $\sigma = 2\pi k/B$, where B is the number of blades on the rotor. The matrix of influence functions K and the loading vector L in Equation 2.12 are also complex for unsteady loading. Equation 2.7 gives the complex lift pressure coefficient whose real and imaginary parts give the amplitude of the lift pressure everywhere on the blades and also its phase with respect to the input motion. The system of control points, load paneling, and pressure representation is the same as for steady flow in Figure 2.

By proper specification of the boundary conditions, the theory can treat rigid blades operating in a non-uniform flow field or vibrating blades in a uniform inflow (or a combination of the two). Thus, the method is an extension of the Sears gust interaction theory and the Theodorsen plunging and pitching airfoil theory to 3D, compressible flow. Background on both the Sears and Theodorsen theories is given by Bisplinghoff, Ashley, and Halfman (ref. 8). Since those theories are 2D, the pressure/downwash equations could be inverted analytically. In the 3D case, the inversion is numerical, as indicated by Equation 2.12. However, this permits any periodic blade motion, including deformations of the camber surface.

Volume I derives the theory in detail, shows how to interpret the input and output of the computer program, and presents a series of sample calculations. In particular, comparisons with the Sears and Theodorsen incompressible results and with Amiet's compressible 2D theory (ref. 15) are given. Blade planforms analyzed in Volume I were simple, constant chord rectangular and swept shapes so that 3 dimensionality and compressibility could be studied in simplest terms. In this volume, we study real geometry via the the SR3 Prop-Fan with angular inflow. However, first we review the comparison with the 2D Sears theory to orient the reader to the method input and output and to discuss some important conclusions regarding 3 dimensionality.

Comparison with Sears' 2D Theory

Sears' results are outlined in Figure 14. The airfoil with chord b is fixed at the origin in a flow field with mean velocity U. Superimposed on U, and convected with it, is the upwash gust w described by

$$w = w_o e^{i\omega(t - x/U)} \tag{4.1}$$

where the frequency f is $\omega/2\pi$. Here we use Sears' original convention with a + sign for time in the exponential ($+i\omega t$). Because $x = Ut$ is a constant phase point,

it is clear the Equation 4.1 represents a gust convected with the free stream.

The standard reduced frequency parameter is based on semi-chord

$$k_o = \frac{\omega b/2}{U} \tag{4.2}$$

Since wavelength $\lambda = U/f$ and $\omega = 2\pi f$, the reduced frequency can also be interpreted in terms of chord to wavelength ratio:

$$k_o = \frac{\pi b}{\lambda} \tag{4.3}$$

For a small steady upwash w_o, the incidence angle is $\alpha = w_o/U$ and the lift coefficient is $C_L = 2\pi\alpha$. Sears' result for the unsteady case with $\alpha = w/U$ is

$$C_L = 2\pi\alpha S(k_o) \tag{4.4}$$

where $S(k_o)$ is the Sears function which describes the deviation in amplitude and phase from the steady theory. This is plotted in Figure 14 with reduced frequency as the parameter. It can be seen that the function goes to 1 at 0 frequency, as required, and diminishes in amplitude at higher frequencies. The phase first leads the input then lags as frequency is increased.

Input for the gust cases was prepared as follows. With the $-i\omega t$ sign convention of Volume I used for the 3D analysis, a sinusoial gust is described by

$$w = w_o e^{i\omega(\gamma/U - t)} \tag{4.5}$$

where γ is a streamwise coordinate measured in the helicoidal advance surface at constant radius. γ corresponds to x in the 2D discussion above. The input vector W is obtained by dropping the $\exp(-i\omega t)$ and normalizing by the local section speed U to get the upwash angle:

$$W = \frac{w}{U} = \frac{w_o}{U} e^{i\omega\gamma/U} \tag{4.6}$$

Since the program expects input in degrees, w_o/U was set to 1 for a 1° gust amplitude. To convert $\omega\gamma/U$ to input recognized by the program, we substitute $\omega = q\Omega$, $x = bX_{\bar{n}}$, $b = 2r_T B_D$, $\Omega r_T/V = a$, and $U/V = \sigma$ with the result

$$W = \cos\left(\frac{2qaB_D}{\sigma} X_{\bar{n}}\right) + i \sin\left(\frac{2qaB_D}{\sigma} X_{\bar{n}}\right) \tag{4.7}$$

where q is the non-dimensional blade loading frequency, $\Omega/2\pi$ is the shaft rotation frequency, B_D is the chord-to-diameter ratio, $a=\pi/(\text{advance ratio})$, and V is the flight speed. Equation 4.7 is to be evaluated at the non-dimensional chordwise locations

$$X_{\bar{n}} = -0.5 + (\bar{n} - 0.5)/NCP \tag{4.8}$$

where $\bar{n}$ runs from 1 to NCP. 10 control points were arrayed across the 0.7 radius line so that NCP = 10 and NSM = 1. Cases for the geometry shown in Figure 15 were run for P orders from 0 to 20 with the results shown in comparison with the Sears function. To interpret the P order in terms of reduced frequency, the same substitutions used for Equation 4.7 can be used with the definition of k_o with the result

$$k_o = \frac{qaB_D}{\sigma} \tag{4.9}$$

For plotting on Figure 15, the lift output from the 3D lifting surface program was normalized by $2\pi\alpha$, which amounts to dividing by 0.1097 after converting to radians. Furthermore, the complex conjugate is plotted because of the difference in conventions on the sign of $i\omega t$ in the exponentials of Equations 4.1 and 4.5.

The comparison of 2D and 3D results in Figure 15 can be interpreted as follows. In the limit as frequency goes to 0, the steady result for a twisted flat plate blade is reached. The lift is about 1/2 of the 2D result because of the 3D induction. This lift reduction corresponds to the aspect ratio effect, well known in steady wing theory. More directly, the lift reduction corresponds to the tip loss effect treated by all propeller lifting line theories where the 3D incidence is split into an induction angle and an effective 2D incidence. At the high end of the frequency range, 20P, the 3D lift approaches the 2D value (at least away from the ends of the blade). This effect is also well known in unsteady wing theory (see for example, Jordan (ref. 16)) and is a very satisfying check of the 3D theory.

Since the high and low frequency ends of the 3D curve in Figure 15 could have been predicted a priori, the valuable part of the result is in the detail of the transition from steady 3D behavior at low frequencies to unsteady 2D behavior at high frequencies. The surprise was that at 1P there is almost no effect of unsteadiness. Thus, for this incompressible, unswept case, the 3D lifting surface theory gives results which should depart only minutely from a quasi-steady lifting line calculation. This is an important discovery and answers questions regarding unsteady lift response effects in 1P calculations that have been raised over the past 30 years. In the past at Hamilton Standard, various analysts have attempted to account for unsteadiness by performing a multi-azimuth steady lifting line calculation and then adjusting the amplitude and phase in a strip-wise sense by using the Sears function. Figure 15 shows clearly that this is not correct and that, fortuitously, the quasi-steady calculations should be adequate for 1P and 2P, at least for this unswept case.

This conclusion regarding unsteady effects can at this point only be applied rigorously to the cases run so far and shown in Figure 15. However, based on other experience with the program, it is expected to apply also up to high subsonic tip speeds for straight blades. More cases need to be run so that rules of thumb can be developed on the limits where quasi-steady multi-azimuth calculations can considered accurate.

The final portion of the Sears function check is a comparison of 2D and 3D unsteady pressure distributions. Sears' theory modifies the flat plate steady results in amplitude and phase only. The shape of the pressure distribution stays the same:

$$\Delta C_p = 4\alpha\sqrt{\frac{1-x}{x}}\, S(k_o) \qquad (4.10)$$

Comparisons are given in Figure 16. As might be expected, the 2D and 3D pressure agree closely at the high frequencies (20P) where the lift coefficients matched. This applies to both the real and imaginary parts (in phase and out of phase) and to the detailed behavior near the leading edge. At lower frequencies the pressures depart from the 2D results in a way that is consistent with the lift predictions.

The distributions at the upper right in Figure 16 have the shape given by the radical in Equation 4.10 with the characteristic square root singularity at the leading edge and the zero (Kutta condition) at the trailing edge. Later in this section, distributions with these characteristics are referred to as "flat plate like."

Loading at Shaft Rotation Frequency for the SR-3 Design Point

In the calculations shown above the blades had constant chord planforms to simplify interpretion of the results. In this section we use the actual SR-3 geometry to analyze 1P loading at the 0.8 Mach number design cruise condition with a 3° angular inflow. This case, of course, has subsonic section speeds over the inner parts of the blade and supersonic speeds beyond the 71% radius. Input unsteady boundary conditions were prepared as shown in Figure 17. The advance triangle shown at the left represents the undisturbed flow into the section at radius r. At flight speed V_x, inflow at an angle ψ can be represented by the crossflow velocity $V_x\tan\psi$. The maximum effect on angle of attack can be obtained by adding this to the tangential speed πNDz as shown at the right in Figure 17. It is assumed here that the maximum angle of attack, as given by the formulas in Figure 17 represents the magnitude of the 1P component, i.e. the harmonic contribution is ignored because the inflow is small. The table of W_0's shown was used to generate the 1P input for SR3.

The case was first run incompressibly with the results shown in Figure 18. Because of the low frequency, there is only a small phase variation along the span. In the mid-span area the chordwise distribution has flat plate characteristics but toward the tip the loading is even more leading edge dominated. Nothing unusual seems to be occuring in the root area. At 0.8 Mach number, as shown in Figure 19, the results are more interesting. The root shows considerable interference or cascade effects, as might be expected with 8 high solidity blades. The mid-span area results are very much like the incompressible results just shown in Figure 19. Recall in this regard that, although the section speeds are supersonic, the leading edges are subsonic in the sense that $M_{rel}\cos\Lambda < 1$. (Λ is the leading edge sweep angle.) At the 2 outer stations, there is a loss of lift behind the tip Mach cone as sketched at the lower right in Figure 19. This behavior is well known in wing theories (ref. 17); its appearance in the propeller results is an important part of the code validation. The 1P loading results are summarized in terms of lift coefficient amplitude and phase in Figure 20. It can be seen that the unsteady lift coefficient is quite flat across the span. Compressibility increases the magnitude and the phase lag.

The 3D unsteady theory currently doesn't include any vortex loading effects. At cruise, there shouldn't be much of a leading edge vortex. However, there may be enough lift loading from the tip edge vortex to cause significant bending stress. This speculation should be verified by working with the steady blade pressure data from the test in the ONERA S1 wind tunnel in Modane, France (ref. 18). An example is shown in Figure 21. It can be seen on the camber side (or suction side of the blade) plots, shown at the left, that there is increasing pressure at the outer measurement station. This will not be predicted by a linear theory and is probably caused by the tip vortex rolling up over the blade end and onto the upper surface.

The data from Modane have not been integrated into section lift coefficient or normal force coefficient form for Reference 18. However, for the purposes of this report, data from the 3 cases at the 0.5 Mach number cruise simulation were integrated approximately with the results shown in Figure 22. The middle curve has the loading per blade and the advance ratio corresponding to the design cruise condition. This shows a high tip loading that is undoubtedly not predicted by any of the linear methods. The non-linear buildup of this loading with blade angle is characteristic of a vortex effect.

SECTION 5

NON-UNIFORM WAKE COMPARISONS

The flow behind a loaded rotor has non-uniformities related to the blade loading. Circumferentially averaged axial and tangential velocity components are related to rotor thrust and torque, respectively. Blade-to-blade variations are related to viscosity, trailing vortex sheets, and bound thickness and loading effects. Wakes of Prop-Fan models have been measured with hot wire anemometers in the UTRC acoustic wind tunnel and with a laser-doppler velocimeter in the NASA-Lewis 8'x6' wind tunnel. Comparisons of these data with theory of Volume I of this report provide a valuable check of the analytical method and gives insight into the wake structure. In fact, it will be seen that most of the features of an apparently complex wake flow pattern can be sorted out with a relatively simple wake prediction method. Another reason for interest in the wake flow is that it is a major source of rotor-rotor interaction noise in counter rotation propellers. Blade-to-blade variations, which could be steady in the coordinate system of the front rotor, cause unsteady loading on the rear rotor. Unsteady loading is the dominant source of noise in counter rotation propellers at takeoff conditions.

This section presents comparisons of predictions from the UAAP wake prediction code with data from 3 experiments:

1. A 2 bladed SR-3 propeller model run in the UTRC acoustic wind tunnel at a flight Mach number of 0.32. Overspeeding the propeller simulated the cruise tip speed. Wakes were measured with a hot wire anemometer.

2. An SR-3 model with 8 blades run in the NASA 8'x6' tunnel at the design cruise condition. Wakes were measured with a laser-doppler velocimeter.

3. One rotor of the CRP-X1 propeller model run in the UTRC acoustic wind tunnel at the cruise power coefficient and advance ratio but with reduced flight Mach number. Wakes were measured with a hot wire anemometer.

Wake Prediction Method

Although designated a wake prediction method, the UAAP program actually computes velocity components upstream of the rotor and outside the tip radius as well as in the wake. Sources of the velocity disturbances are the same thickness and steady loading effects that radiate noise. Wake formulas are derived from the general potential theory in Volume I, Section 12 of this report. A viscous wake approximation is added with the 2 dimensional formulas of Silverstein, Katzoff, and Bullivant (ref. 19), which are based on section drag coefficient. Since the blade loading must be known for a wake prediction, a performance calculation run must be done first. The computed loads are then transferred to the wake prediction section.

The potential part of the predicted disturbance contains two components. The more important of these is the system of vortex sheets that trails the rotor to downstream infinity. The outer edges of these sheets include the theoretically infinite spanwise and radial components that cause a rollup of the actual wake into distinct tip vortices at some distance downstream of the rotor. The vortex sheet

model does not include the rollup and therefore will not be useful for very high loading cases and for field points far downstream of the rotor. However, for cruise design loading and field points where a downstream rotor would be located, the method works reasonably well. The other component of the potential field calculation is the near-field (or bound) effect. This was added under the current contract and represents the bound circulation and thickness disturbances that do not trail into the wake. At high speeds, however, they radiate as sound and some of this effect will be seen in the data to be discussed below.

Test/Theory Comparison for the 2 Bladed SR-3 Model

The test for this comparison was run in 1978 in the UTRC Acoustic Research Tunnel by Dr. William Patrick. Since preparation of the first draft of this report, an AIAA paper (ref. 20) was prepared. It includes more detail on the measuring techniques. The operating condition was as follows.

Advance ratio = 0.90
Power coefficient = 0.0901
Tunnel Mach number = 0.32

Since the tunnel speed and drive power were limited at the time of the test, this condition was the best means to simulate cruise operation. The tip relative Mach number was 1.17 and the section lift coefficients were in the range typical of those for the cruise condition.

Figure 23 shows the range of radii traversed by the hot wire probe system. The test values of radius ratio were .6, .7, .8, .85, .9, .925, .95, .975, 1.0, and 1.025. The radial traverse was 1/2 tip chord axially downstream of the tip trailing edge. Three specially designed probes were used in separate test runs to acquire data required to extract the 3 velocity components. The data were signal enhanced and digitized on-line and processed off-line to produce plots of v_{axial}, $v_{tangential}$, and v_{radial} as functions of time. Because of the rotation, time corresponds to angular location behind the rotor.

The following paragraphs present first a physical discussion of some of the flowfield features by comparison with isolated data traces. Then figures are presented showing all of the traces and how they compare with theoretical predictions. Figure 24 shows a typical plot of the tangential velocity component at the right. Time on the abscissa corresponds to slightly more than a blade passing period. Numbers shown with the trace correspond to features in the field that can be understood on a 2-dimensional basis using the sketch at the left in the figure. Consider the probe to be fixed in the flow as indicated by the X in the sketch. Also, consider the flow field to be locked to the blade section and rotating with it. This flow field would include (1) a bow shock, (2) a recovery region, and (3) a trailing shock, if the Mach number is high enough, and (4) a viscous wake. The flow pattern is dragged past the probe in the rotation direction so that the wake events are observed in the order shown. The shock waves are felt first; however, for this operating condition, the bow shock (which would be at location 1) is suppressed by leading edge sweep. That is, the section relative Mach number times the cosine of the leading edge sweep angle is less than unity. There is, however, a pulse from the mid-chord area at location 2 and a trailing edge shock is clearly seen at location 3. In fact, the pulse in the 1-3 area looks very much like a noise pulse as

measured by a microphone for this condition and reported, for example in Reference 22. The viscous wake produces the peak in the trace at location 4. The number 5 on the trace at the right indicates the beginning of the pulse from the next blade.

Figure 25 shows the axial and tangential components at radius ratio 0.7, which can be used to define sign conventions. The plots show clearly divided regions of viscous and potential flow. For the axial component at the top, velocity is positive in the downstream direction. Thus, the viscous wakes, which are at the vortex sheets, are negative, representing retarded flow. The potential contribution is positive at the vortex sheets, representing a downstream impulse. This illustrates one of the difficulties in wake prediction, namely that the viscous and potential effects are opposed for the axial component so that partial cancellation is predicted. In the tangential component shown at the bottom in Figure 25, positive values correspond to components in the direction of rotor rotation. Thus, viscosity drags the wake flow in the direction of rotation and the potential flow imparts an impulse in the same direction. This can be seen more clearly in Figure 26 which shows a data trace at the top and the corresponding theoretical prediction at the bottom.

As was just shown, much of the axial and tangential flow is explainable in 2D terms. However, the radial velocity component is exclusively a 3D effect and is discussed in the context of Figure 27. The planform at the top could represent either a wing or a propeller blade. The variation of the loading, or circulation, along the span produces the trailing vortex system. In fact, if Γ is the circulation at any radius r, then the strength of the trailing vorticity at that radius is proportional to $\partial\Gamma/\partial r$. Since the circulation drops very rapidly to zero at the tip, the vorticity is strongest there. The vortex sheet is a slip surface. Underneath the sheet, on the side corresponding to the pressure side of the blade, the flow near the tip is radially outward and above the sheet it is radially inward. Simplistically, the flow leaks around the tip from the pressure side to the suction side. At the sheet, there is a velocity jump of the form suggested at the bottom in Figure 27. This characteristic jump does occur in the data as shown by the sample trace in Figure 28. The sign of the jump is, of course, given by the sign of $\partial\Gamma/\partial r$. At the point along the span where the circulation has its maximum value, $\partial\Gamma/\partial r$ changes sign, providing a powerful diagnostic tool for checking loading distributions.

Prepared by this physical discussion, we now examine the remainder of the data. Figure 29 shows all of the experimental results: 3 velocity components at 10 radial stations. As would be expected, the disturbances are most violent in the tip area. The axial and tangential components there are strong and local as opposed to their weaker, more spread out character at $r/R = 0.6$. In the axial velocity traces, the sign of the potential flow pulse changes between $r/R = 0.95$ and 0.975 indicating that the tip vortex lies between these 2 radii. This sign change seems to be a very reliable locater for the vortex and is used on-line for guidance during tests. The radial velocity component at the right in Figure 29 exhibits the jump linked above to the variation in circulation. At $r/R = 0.7$ the sign of the jump changes indicating that the circulation peak is near that radius.

Figures 30 to 32 show the theory/data comparisons for the 3 velocity components. In generating these figures certain liberties were taken which must be explained. First, the theory curves were shifted horizontally and vertically for the best fit. The vertical shift is justified because the blockage of the centerbody, which produces axial and radial offsets in the mean flow, is not included in the theory. The mean value of the tangential component was very difficult to mea-

sure accurately because of critical dependence on probe alignment. The horizontal shift was justified because distortion due to swirl also is not included in the analysis. Finally, the analysis does not recognize contraction of the slipstream behind the rotor so that the tip of the theoretical vortex sheet always lies at r/R = 1. To compensate for this, the radial stations calculated were adjusted so that the tip flow fell between the r/R = 0.95 and .975 stations as required by the flip in axial component shown in Figure 29. The stations were adjusted on an annular area basis according to the table below.

data	calc	data	calc
.6	.616	.925	.954
.7	.720	.95	.979
.8	.824	.975	1.005
.85	.876	1.000	1.031
.9	.927	1.025	1.060

Tangential velocity predictions are shown first in Figure 30. They are seen to agree well with data over the entire radial range. In particular, the split between viscous and potential effects and between bound and trailing effects is well represented. In reducing the data at r/R = 0.975, convergence difficulties were encountered in the data reduction program so that this trace probably includes some extra uncertainty. At the outer radii, the predicted pulse associated with bound effects does not have the strength or sharpness of the data trace. At first this was believed to be a failure of the velocity predictions, but further thinking suggests that the data trace is responding to density as well as velocity waves. The data acquisition and reduction scheme assumed incompressible flow. This was justified because the mean flow over the hot wire probes is basically the tunnel speed (M = 0.32) plus the small amount of axial induction. Hot wires measure ρu, which in incompressible flow varies only with velocity. However, the acoustic pulse is a density wave which influences this portion of the data trace. Analysis of data from microphones very near the blade tips (Reference 20) indicates pressure variations large enough to explain the pulse circled for r/R in Figure 30.

Figure 31 compares the predicted and measured axial velocity components. The agreement in the tip area is satisfactory, particularly regarding the flip in sign of the velocity pulse at the tip vortex. At inboard radii, it can be seen for this component that the viscous wake is underpredicted. Since the vector sum of the axial and tangential components is approximately correct, the error may be due to neglect of changes in flow direction induced by rotor loading. Also, at radius ratios from .8 to .9 the potential velocity pulse is predicted to be much stronger than the test indicates. The reason for this has not yet been established but could also be associated with angle changes in the mean flow.

Finally, Figure 32 gives the comparisons for the radial velocity component. Again the general characteristics are well predicted, particularly in the tip area. The major discrepancies are at the inner radii where the magnitude of the velocity jump is overpredicted. The change in the sign of the velocity jump is predicted to occur slightly outboard of that for the data. This suggests that the loading distribution may not be quite correct. There seems to be some radial viscous flow shed from the blade boundary layer. This effect is not included in the theoretical model. At r/R = .90 and .925 the negative part of the pulse after the jump is not correctly predicted. Separate analysis suggests that this is caused by rollup of the wake, which is currently neglected in the theory.

Test/Theory Comparison for the SR-3 Prop-Fan

Data in this section were acquired and reported by Serafini, Sullivan, and Neumann ref. 22). The test was in the NASA-Lewis 8'x6' wind tunnel using the 2' diameter 8 bladed SR-3 model. This seems to be the only data at the full cruise Mach number (0.8), the design advance ratio (3.06), and the design power coefficient (actually slightly higher at 1.8). A laser velocimeter was used to obtain the 3 velocity components. This was required since hot wires are difficult to use in high speed, compressible flows due to fragility and difficulties in data reduction. In principle, the LV system measures velocity specifically so that questions of density waves mentioned above do not arise.

Comparisons are made with data from the 2 traversing planes indicated in Figure 33. The closest axial station, x/R = 0.89, was nearly grazing the blade tip. The UAAP wake program has not been designed to converge well this close to the blades and produces unreliable results, as will be seen. This is not an intrinsic limitation of the method; wake predictions are not usually needed in this region and the extra coding effort needed to improve accuracy in this region could not be justified.

Figure 34 compares the circumferentially averaged tangential velocity with predictions. This is related to the radial distribution of torque on the rotor and indicates a good airload prediction. The variations in the first 3 data points are not reproduced but otherwise agreement with data is excellent.

The remaining figures in this section deal with blade to blade variations in velocity components. For reasons given above in conjunction with the hot wire data, placement of the theoretical curves was adjusted horizontally and vertically with respect to the data curves to produce the best fit. Actual test radii were used for the calculations. Figure 35 shows the radial velocity at a station just outside the tip to be well predicted at both axial stations. The difference between the two curves is mainly a phase shift.

Figure 36 shows the corresponding axial velocity curves outside the blade tips at r/R = 1.08. Agreement at the downstream station is excellent but the prediction at the x/R = 0.89 station shows too strong a velocity pulse, possibly because of the convergence problem mentioned above. Axial velocity curves at radii just inside and just outside the tip vortex are shown in Figure 37. These exhibit the required inversion of the pulse at the tip and are qualitatively quite good. Detailed agreement suffers from being too close to the blade tip. The tangential component is shown in Figure 38; similar remarks apply.

Test/Theory Comparison for a Single Rotor from CRP-X1

The rear rotor of the CRP-X1 Prop-Fan model was run alone in the Acoustic Research Tunnel at UTRC for hot wire measurements of its wake. Data were acquired and reduced by J. Simonich and G. Tillman. The cruise condition was simulated at a tunnel speed of 0.25 Mach by setting the design advance ratio (J = 2.85) and a blade angle to produce the design power coefficient (C_p = 1.0). This kind of simulation reproduces the correct distribution of flow angles across the span and yields a distribution of lift coefficient nearly the same as that at the higher Mach number; only the compressibility effects are absent. Wake rollup and vortex loading should

be about the same as in the actual cruise case. Some data acquisition problems were encountered and only the data considered reliable at the time this report was written are shown herein. Since writing this report, Tillman, Simonich, and Wagner have revised the data reduction process enabling data from all of the radial stations to be presented (reference 23).

Axial and radial locations used for the probe traverse are shown in Figure 39. Theory/data comparisons are shown in Figures 40 to 42. Axial velocity traces in Figure 40 exhibit characteristics similar to those seen for the other two sets of data and similar remarks apply. The pulse inversion occurs between $r/R = 0.96$ and 1.04 indicating the presence of the tip vortex between these two radial stations. Similar effects are found in the tangential component traces in Figure 41. Figure 42 shows the radial velocity traces.

Conclusions from this section on wakes and others are summarized in Section 8.

SECTION 6
NOISE THEORY VERIFICATION

Harmonic noise of single rotation Prop-Fans with steady blade loading is caused by blade thickness and loading sources. Loading may have the classic potential flow characteristics or it may be dominated by vortex flow effects. Which of the sources is most important depends on propeller operating conditions. At cruise conditions, conventional thickness and loading sources tend to dominate whereas, at takeoff conditons, vortex loading sources become very significant. The noise test/theory comparisons of this section are presented in two major categories: high and low flight Mach number. Of the several sets of experimental data that could be used for the comparisons, the NASA Jet Star flight test results for the SR-2 model (straight blades) and the SR-3 model (swept blades) were chosen as most reliable for the high speed conditions. For the low flight speeds, data from a single rotor of the CRP-X1 Prop-Fan model in the UTRC Acoustic Research Facility were chosen. Before the results are presented, the noise prediction methodolgy is reviewed.

Review of Noise Calculation Methodology

The radiation formulas used for noise predictions are based on the linear wave equation with monopole and dipole sources. The derivation is given in Volume I of this report. Except for minor notational differences, the formulas are equivalent to those published previously by Hanson in References 1 and 3. They give the noise harmonic levels and directivity for specified values of the thickness and loading sources. A new feature of the present work is that a means to evaluate the source strengths via a linearized lifting surface theory as described in Section 3 of this volume is also provided. In earlier applications of the noise theory, the thickness source was given strictly by the blade geometry and the loading was assumed to be potential. However, in the current application, the thickness source has been modified to include the boundary layer displacement thickness as well as the blade metal thickness. This is analogous to the standard boundary layer effect in airfoil aerodynamic methods. Also, the loading source has been modified to include the effects of the various vortex loading components shown in Figure 5. These modifications to the thickness and loading sources are described in the next paragraphs.

Treatment of Noise Sources - Data from tests of a model Prop-Fan suggested that the addition of the boundary layer and wake displacement to the airfoil thickness would improve prediction of noise waveforms. In Figure 43 it can be seen that the amplitude of the positive peak is overpredicted by the theory. It appeared that including the displacement terms would "soften" the thickness profile at the trailing edge, thereby reducing the amplitude of the trailing wave, as shown at the top in Figure 44. In order to verify this hypothesis, an analytical model of the boundary layer and wake displacement thickness was developed.

The displacement is modelled in five sections; three in the boundary layer and two in the wake. The boundary layer model was developed from a data base of two-dimensional airfoil calculations using the TRANDES transonic computer code (ref. 25), while the wake model is based on a series of experiments performed by Cook (ref. 26). The boundary layer is approximated by two straight lines followed by an exponential increase to the trailing edge as shown by the curve labeled "boundary layer disp thickness" in the top 1/2 of Figure 44. The thickness at the trailing edge is a function of local blade section drag coefficient. In the wake, the displacement thickness decays exponentially from the trailing edge value to an asymptotic value which extends to infinity downstream as suggested also in Figure 44.

The use of straight line and exponential curve fits allowed the thickness function to be transformed analytically for use in the noise calculation. The chordwise Fourier transform for the thickness functions at the top in Figure 44 are shown at the bottom of the same figure. There it can be seen that the displacement thickness does not modify the airfoil transform to large degree at low wavenumbers, but has a significant effect at wavenumbers above 10. Thus, the noise at blade passing frequency might be unaffected, while a noise waveform (which is composed of many harmonics) may be affected.

Figure 45 shows the effect of adding the displacement thickness term to a noise waveform calculation. This figure indicates that the calculated trailing wave amplitude is reduced by the addition of displacement sources, giving improved agreement with data. It should be pointed out that Tam has shown that non-linear propagation, in the sense of sonic boom theory, has a similar effect on noise pulses (ref. 27).

Treatment of Loading Elements - In order to determine the blade loading, an aerodynamic calculation is done as described in Section 3 of this report with a manual iteration on blade angle in order to obtain a close match between calculated and measured power. Because of the power prediction errors explained in Section 3, this procedure is necessary to obtain a realistic estimate of loading noise levels, particularly for low speed, high power cases. For the cases considered herein the final value of calculated power is within 3% of the test value.

The choice of vortex load components to be applied is implicit in the aerodynamic calculation, since all vortex components (leading edge, tip edge, and augmented lift vortex) are selected by default. A further choice is determining whether the tip edge vortex force acts in the lift (default) or radial direction. For the power iterations, the default values were used. However, for some noise calculations the tip edge force was assumed to be radial in order to demonstrate the magnitude of the radial loading noise source.

The noise calculations were carried out in three steps. First, the potential loads were calculated (using the non-linear iteration procedure) and the results written to an intermediate data set. The vortex loading calculation then used this information to calculate the overall blade loading and propeller performance, after iterating manually to match shaft power, as described above. The appropriate information was written to a second intermediate data set and these stored data were then used to calculate radiated noise. Saving the intermediate data sets allows minor variations, such as changing observer positions, to be run without re-running the entire case.

A sample of the magnitude of the vortex loading and its effect on noise predictions for a takeoff case are shown in Figure 46. The upper part of the figure shows the spanwise loading distribution associated with potential flow and the added effects of the leading edge vortex, the tip edge vortex, and the tip lift produced by the leading edge vortex (augmented lift). The lower portion of Figure 46 gives directivity patterns for the BPF levels associated with each of the above loading curves. For the tip edge vortex, the suction analogy gives the magnitude and chordwise distribution of the loading. For performance purposes this is adequate. However, for propeller noise prediction, the spanwise distribution of the load is important because radiation efficiency increases rapidly with radius. This effect is strong enough that the width of the shape functions in Figure 46 cannot be chosen arbitrarily. The widths were chosen after some experimentation but are not necessarily optimal.

Noise Theory Evaluation for High Flight Mach Numbers

The noise levels used for comparison with calculations are those taken on the microphone boom of the NASA JetStar (ref. 21) with tone levels reduced by 4 dB to account for pressure reinforcement at the boom surface using the theory of Reference 29. Figure 47, taken from Reference 21, is a photograph showing the test airplane with the SR-3 Prop-Fan installed. Test conditions for the SR-3 and SR-2 models are listed in Table 6-I. The two columns at the right give the figure numbers where the noise comparisons are presented. The first of those two columns relates to calculations performed using the "standard" or default input. The last column relates to calculations presented to illustrate the effect of radial loading. Radial loading noise calculations have the tip vortex load acting in the radial direction.

TABLE 6-I
TEST CONDITIONS AND FIGURE NUMBERS FOR HIGH SPEED CASES

Model designation	Flight Mach number	Advance ratio J	Power coeff Cp	Pressure alt, ft	Noise directivity figures: Standard Calculation	Noise directivity figures: Radial Load Calculation
SR-3	.511	2.918	1.888	20000	48	56
SR-3	.620	2.961	1.948	30000	49	57
SR-3	.713	3.062	1.837	30000	50	58
SR-3	.787	3.029	1.828	30000	51	59
SR-2	.520	3.178	2.372	20000	52	
SR-2	.617	3.174	1.818	30000	53	
SR-2	.710	3.151	1.985	30000	54	
SR-2	.787	3.186	2.094	30000	55	

Directivity and Mach Number Trends - For high speed cruise of a single rotation Prop-Fan, the directivity of the blade passing frequency (BPF) harmonic is considered to have the greatest impact on passenger comfort. Comparisons of measured and calculated BPF harmonic directivities are shown in Figures 48 to 55. Positive values of observer position represent positions forward of the plane of rotation. Note that the microphone located at the 0.525 ft visual position was inoperative during the SR-3 flight test. The following general observations can be made. First, the noise levels for the SR-2 and SR-3 models are similar (at a given position) for the lower flight Mach numbers, but SR-2 is significantly noisier at the higher flight Mach numbers. Second, the calculated directivity and peak noise levels tend to match test data better as the flight Mach number increases. Agreement of the theory and test data is considered very good at 0.8 Mach. At the lowest Mach number there is a tendency to underprecict in the forward quadrant and overpredict in the aft quadrant. Since this trend does not appear in the low speed wind tunnel data (discussed below in this section), it may be caused by some aspect of the flight test environment. For example, aircraft incidence increases as flight speed is reduced, probably causing non-uniform inflow. Also, some simple calculations with a theory similar to that in Reference 29 indicate that reflections from the fuselage at the boom location may be significant, despite the fact that the fuselage surface is convex. Finally, the 4 dB boom correction is based on an infinite cylinder model and may be too simplistic.

Noise due to Radial Loads. - Simple potential flow methods assume that flow leaking from the pressure side of a wing or blade tip to the suction side stays attached and thus produces a spanwise or radial force. For thin, highly loaded tips, however, the flow is more like the center sketch of Figure 5. The flow separates and reattaches in a manner such that the radial force reorients to the lift direction as shown in the sketch. In fact, the assumption of the suction analogy[10] is that the force magnitude is the same whether in the radial or lift direction. Since it is not known to what extent the flow separates in any particular case, a numerical experiment was conducted to determine the role of the radial loading noise source. Noise calculations were done with the tip edge force oriented radially and results can be compared with those presented above. Although changing the side edge force from the lift direction to the radial direction reduces the predicted power coefficient by about 5%, no further iterations to match power were done since the intent is to show relative magnitudes of the noise sources.

Figure 56 through 59 are plots of the BPF directivities for the SR-3 test data and calculated noise including radial loading. Comparison of these plots with Figures 48 through 51 indicate that radial loading makes a slight improvement to the predictions with a small increase in the forward direction at 0.79 Mach number and a small decrease aft at lower Mach numbers. However, it must be recognized that these figures are provided for reference purposes only since they were done by arbitrarily assuming that the full potential radial load could be supported at the tip. In fact, most of the calculations produced radial load coefficients that correspond to negative absolute pressures acting on the blade end, which, of course, is not possible. This is taken to mean that the flow cannot remain fully attached and must indeed separate as sketched in Figure 5.

In comparing Figures 48 through 51 run in the default mode with the tip edge suction force acting normal to the blade surface with their conterparts in Figures 56 through 59 where the edge force is radial, the reader may notice that the monopole levels are slightly different. This is caused by an interaction between the drag component of the rotated normal force and the boundary layer displacement effect described in conjunction with Figure 44, which is driven by drag. This interaction in the code is probably not representative of the real flow condition; however, the effect is so small (a fraction of a dB) that no attempt was made to eliminate it.

Trends of Peak Noise with Increasing Mach Number. A valuable way to evaluate noise trends is to conduct an experiment at constant advance ratio and constant blade angle but with varying flight Mach number. Under these conditions the advance angle distribution across the blade span stays constant and non-dimensional measures of blade loading such as power coefficient, lift coefficient, and pressure coefficient remain constant except for compressibility effects. (Reynolds number influence is generally small.) Dittmar has presented noise results from this kind of test[28] in which he plotted the maximum value of the BPF harmonic along the sideline at any condition as a function of the tip relative Mach number. Obviously, noise levels generally tend to increase with increasing Mach number. However, Dittmar's results have generated considerable interest because some of his noise curves tend to level off or even decrease at high Mach number. This has prompted speculation that designs for higher tip speeds may be desirable.

Trends from the current study for SR-2 and SR-3 are plotted in this manner in Figures 60 and 61. Blade angle and advance ratio (and measured power coefficient) are almost constant for these curves. Note that the noise levels at the lowest Mach number have been corrected to account for the difference in pressure altitude. For both propellers, the curves exhibit a slight reduction in slope starting at a tip relative Mach number of 1.0 but the effect is more pronounced for the SR-3 model (with swept blades). There is no indication from the Jet Star data that the noise levels will decrease with increasing Mach number or even level off. It is not clear why Dittmar's plots show a more pronounced slope change but it was noted that the slope changes in his plots were accompanied with a significant reduction in shaft power coefficient. By contrast, power coefficient was more nearly constant for the curves in Figures 60 and 61.

The more pronounced slope reduction for the SR-3 model data in Figure 61 compared with that for SR-2 in Figure 60 can be explained by the fact that noise cancellation due to blade sweep increases with increasing flight Mach number. Consider the 0.5 Mach number case where the peak measured noise radiation angle is 60°. By using formulas from Reference 2, it is computed that the geometric sweep (the difference in mid-chord alignment measured at the root and tip) is about 30% of the acoustic wavelength. At 0.8 Mach number, the peak measured noise radiation angle is 58° and the geometric sweep is found to be 56% of the acoustic wave length. Since ideal cancellation between 2 radii occurs with a 1/2 wavelength difference, it can be seen that sweep is much more effective at the higher Mach number. Similar trends were shown in Reference 2.

Noise Theory Evaluation for Low Flight Mach Number

The CRP-X1 noise levels used for comparison with calculations were measured in the Acoustic Research Facility at the United Technologies Research Center (ref. 23) with only the rear rotor installed. The facility and microphone locations are shown in Figure 62. Harmonic levels were obtained from narrow-band spectrum analyses which were corrected for propagation through the shear layer. Test conditions are listed in Table 6-II. The tunnel Mach number was 0.26 in all cases. The 3 columns at the right give the figure numbers where the noise comparisons are presented.

TABLE 6-II
TEST CONDITIONS AND FIGURE NUMBERS FOR LOW SPEED CASES

Advance ratio J	Power coeff Cp	Noise directivity figures BPF	2X	3X
1.178	.3487	63	68	71
1.178	.6988	64	69	72
1.151	.1445	65		
1.151	.4767	66		
1.151	.6781	67	70	

Comparisons of measured and predicted BPF tone directivities are shown in Figures 63 - 67. Test data which were contaminated by wind tunnel background noise have been corrected or eliminated from the plots. Again positive microphone locations are forward of the plane of rotation. Predicted noise directivities are generally good, with the best agreement at the peak and aft locations and poorer agreement forward of the plane of rotation. The theory underpredicts the peak noise by 2 to 5 dB, with better agreement at high power levels. Similar results are evi-

dent for the 2xBFP harmonic (Figures 68 - 70) and the 3xBPF harmonic (Figures 71 and 6.30), where the underprediction of the peak is from 3 to 5 dB. Reasons for these underpredictions are explored below.

The prediction system used for the above noise comparisons is a direct application of the acoustic analogy and, in principle, should produce more accurate results. The sources available in the acoustic analogy are the monopole (to represent the linear thickness effect of the blade sections), the dipole (to represent blade loading), and the quadrupole (to represent the total of the non-linear effects). The thickness effect is far too low at these Mach numbers to be a candidate for major improvement. Similarly, the quadrupole source terms can be estimated with enough accuracy to show that they are not significant at low speed. This leaves the dipole loading term as the prime candidate for improving noise predictions. The noise predictions can only be as good as the loading representation input to the program. At this point, the sole control of the loading input is that the test and theoretical power (and torque) match closely. In the scope of the current effort, it has not been possible to verify details of load distributions by comparison with data. It is not known to what extent the predicted thrust matches measurements. For the low tip speed cases in the takeoff regime, noise predictions are very sensitive to details of load distribution in the tip area. The tip edge vortex and augmented lift vortex loading have been distributed using simplistic assumptions that may be adequate for performance calculations but not for noise. The accuracy of this modelling needs to be examined.

Conclusions from this and other sections are summarized in Section 8.

SECTION 7

WING AND BOUNDARY LAYER SHIELDING STUDIES

The majority of this report treats noise and aerodynamics of propellers operating without any surfaces to modify flow fields or propagation paths. However, installation effects can modify propeller inflow and cause unsteady blade loading. Noise formulas for this effect are presented in Volume I of this report. Installation can also cause various shielding effects and two of these effects are studied in this section. The first is shielding by the wing of noise propagating to the fuselage wall; the second is shielding (via refraction) of noise at the wall by its own boundary layer.

Flight conditions typical of takeoff (or climb), approach and cruise were studied using the airplane shown in Figure 73. The flight Mach numbers associated with these conditions were chosen to be 0.25, 0.15, and 0.8, respectively. The propeller tip speed was 800 ft/sec for the takeoff and cruise cases, and 700 ft/sec for the approach case. The altitude at cruise was assumed to be 35000 ft, and sea level for the other conditions. Standard atmospheric conditions were used for the calculations.

Wing Shielding Study

The theory for this study was developed by Amiet and is presented in Volume II of this report. The wing is modelled as a semi-infinite plane with source and observer locations anywhere in the flow field. Refraction at barriers has been treated in the literature in the past but, under this contract, Amiet has added the effects of flow and sweep of the leading edge.

The airplane used for the shielding studies is shown in Figure 73. The wing shielding concept depends on the fact that, for high speed blades, the important source region on the propeller disk is that area where the blades approach the observer point at the highest Mach number. For the sense of rotation shown, this is near the bottom of the disk. This fact, in conjunction with wing sweep, can provide some noise shielding along the line of windows in the region indicated in Figure 73. If the propeller rotated in the opposite direction, noise in the same region would come from both the direct path and a reflection from the top of the wing. Since this would cause a noise increase, the most desirable configuration would be as shown in Figure 73 with the propellers on opposite sides of the fuselage rotating in opposite directions.

If noise propagated strictly as rays, then Figure 73 would provide all the information to compute the shielded region. But, of course, at the frequencies of interest, the refraction effects addressed by Amiet's theory must be considered. For calculation purposes, the noise source region was assumed to be at 80% radius on the blade directly approaching the observer location as shown in Figure 73. The objective was to determine changes in noise level along the window line above the wing due to the presence of the wing. Geometry for Amiet's theory is shown in Figure 74. The effect of diffraction can be presented in either of two ways. The first is as the ratio of sound pressure at the observer including diffraction effects to the pressure which would exist in the absence of the wing. The second addresses the fact that Amiet's monopole source does not necessarily have the same directivity as the propeller source. In this case results are presented as the ratio of the sound pressure at the observer to that which would exist for the sound

ray incident on the wing leading edge at an equal observer radius. The former best applies outside the shadow zone and the latter best represents results in the shadow zone. Computed results are presented in the appropriate form.

Calculations are shown in Figures 75 to 77 for the three flight Mach numbers. It can be seen that the wing shielding has a stronger effect at the high Mach number condition, but is not as strong a function of frequency at cruise as at the low Mach number cases. This is partly due to the different Mach number, but the different speed of sound at the cruise altitude has some effect since a characteristic variable is sound frequency/speed of sound. In order to determine the noise levels at the observer, the values shown in Figures 75-77 should be added to calculated noise levels. For the wing shadow zone, the appropriate noise level to be corrected is that calculated at the intersection of the propagation path with the wing leading edge.

Boundary Layer Transmission and Fuselage Reflection

The theory for this study was developed by Hanson and Magliozzi and presented in Volume V of this report, and is somewhat condensed form in Reference 29. It models the fuselage as an infinitely long circular cylinder with a boundary layer profile that is constant along its length and circumference. The propeller is modelled as a compact thickness source rotating at an effective radius which is user selected. The default value of 0.8 times the propeller radius was used for the study reported herein. The theory works by matching solutions to the acoustic wave equation at the boundary layer edge. Outside the boundary layer, the convected wave equation is used without shear terms and includes the wave incident from the propeller and the reflected wave. Inside the layer the shear term is included in the solution and the pressure is found by numerical integration. The method was originally developed to help understand noise data from the Jet Star (Figure 47), which showed large attenuation of noise forward of the plane of rotation for high flight numbers. The objective of the present work is to assess the effect of boundary layer refraction and fuselage scattering for more representative geometry and scale.

For the purpose of this study, the boundary layer velocity profile was assumed to follow a 1/7 power law (typical of a turbulent boundary layer) and its thickness was assumed to be 10 cm (4 in.). Calculated results for noise transmission through a boundary layer are in the form of a noise level with boundary layer effects referenced to the direct path noise level at the observer. Effects of scattering at the fuselage (which for an infinite fuselage radius would give a 6 dB noise increase) are included in the calculation. Scattering effects for the configuration studied are predicted to be from +4.5 to +6.0 dB, depending on frequency. Boundary layer effects were found to be less than 1 dB for the first three harmonics of blade passing frequency at 0.15 and 0.25 flight Mach numbers and therefore are not plotted here. The studies in Volume V have shown that boundary layer effects are relatively small up to 0.6 Mach number, where a rapid increase in the effect begins. The calculated results for 0.8 Mach number are presented in Figure 78. Here it can be seen that boundary layer effects can cause substantial noise reductions at forward locations, even at the blade passing frequency harmonic. Aft locations are not significantly affected by boundary layer shielding. As was the case for wing shielding, the noise level at the fuselage surface is obtained by adding the values from Figure 78 to calculated free space noise levels.

The calculations for Figure 78 were based on a compact representation of the thickness source. Theory has been derived in Volume V for distributed thickness and

loading sources, but these more general equations have not yet been coded. It is felt that the incremental levels shown in Figure 78 are representative of the more general problem because frequency and Mach number are probably the dominant parameters. However, this is speculation at this point and it would be best to code the general theory so as to have a more powerful prediction tool.

Summary of Propagation Effects

Wing shielding can reduce noise levels at the fuselage surface for all flight conditions studied. However, boundary layer effects become important only at high flight Mach number. For the cruise condition it appears that a proper choice of wing-propeller geometry could substantially lower cabin interior noise levels. Boundary layer shielding would be a benefit at forward locations; wing shielding would be a benefit at aft locations. However, opposite rotation of the propellers on either side of the aircraft would be required to take full advantage of wing shielding.

Conclusions from this and other sections are summarized in Section 8.

SECTION 8
CONCLUSIONS

A lifting surface aerodynamic panel method has been programmed for prediction of steady and unsteady blade loading, aerodynamic performance, wakes, and noise. The method is based on a pressure potential theory derived from the linearized wave equation with monopole sources representing the blade thickness effect and dipole sources representing blade loading. Two aspects of non-linearity are treated in approximate fashion. First, the circumferentially averaged axial momentum equation is satisfied at each radial station by an iterative method. Second, vortex loading is added via the suction analogy.

Steady or unsteady blade loading distributions can be computed from a prescription of blade geometry and motion. Once the loading is available, performance, wakes, and noise can be computed by running different parts of the program. This report presents results of analytical studies and test correlations with this new prediction system. Also included are results of studies of boundary layer and wing shielding based on separate theoretical developments. Conclusions from the previous sections of this report are summarized below under the appropriate headings.

Steady Aerodynamic Performance

Power absorption curves for Prop-Fans with straight and swept blades were compared with theoretical predictions at M=0.80 and M=0.27. Contributions of the 2 non-linear factors mentioned above were examined.

At the higher Mach number, representing cruise conditions, power absorption was well predicted over a large range of blade angles and advance ratios. Non-linear effects were a minor factor, particularly for the straight bladed rotor.

At the lower Mach number (0.27), representing takeoff, power absorption is well predicted only at low powers. For blade angles and advance ratios that produced the climb power coefficient in the model tests, the theoretical program is subject to overprediction of power absorption that can be 50% or more. The reason for this appears to be that vortex loading was added to the panel method as a "one shot" calculation after the potential blade loading was computed. This is a direct adaptation of the wing methods, as originally planned. However, on the basis of the evaluation reported in this volume, it appears that the vortex loading should be brought inside the axial momentum iteration loop for better results. Until this change is introduced, blade loading for wake or noise prediction is to be computed by adjusting blade angle manually in the calculation to achieve the desired power coefficient.

Unsteady Blade Loading

The unsteady version of the blade loading theory accepts as input a vector of downwash angles representing unsteady boundary conditions at each of the control points on the blade. Output is the distribution of unsteady lift pressure. Because of its generality, the program can deal with non-uniform inflow problems, blade vibration problems, or combinations of both. Blade motion can consist of pitching, plunging, or any type of camber and twist deformation. Operating conditions with

subsonic relative speeds at the root and supersonic speeds at the tip are permitted. Some theory verification cases were presented in Volume I of this report. Cases presented in this volume lead to the following conclusions.

A comparison was made with the Sears 2D unsteady, incompressible lift response theory by running sinusoidal gust input at the 0.75 radius. It was found at high frequency that the 3D results approached the Sears 2D theory, as required. At low frequency, the 3D theory showed a significant lift reduction due to induced effects as expected from classic wing or propeller theory. At the once-per-revolution frequency, there is only a negligible amplitude and phase shift due to unsteadiness, a property not expected from 2D considerations.

Calculations were made for the SR-3 propeller with a 3 degree angular inflow at the cruise condition. Pressure distribution, amplitude, and phase all showed strong effects of compressibility. Indications are that vortex loading at the tip, which currently is included in the steady prediction method but not in the unsteady method, contributes significantly to blade unsteady bending stresses.

Wakes

The theoretical model for wake prediction includes effects of viscosity, trailing vortex sheets, and near field thickness and loading effects that do not contribute to the vortex sheets. Predictions were compared with hot wire and laser velocimeter data from 3 tests of model Prop-Fan rotors. All 3 velocity components were measured for 2 subsonic tip speed conditions and one supersonic tip speed condition. The theory generally agrees well with the data and explains nearly all of the observed features of the measured velocity waveforms.

The radial velocity signal has a sawtooth behavior in which the jump occurs at the vortex sheet. The amplitude of the jump is proportional to the radial derivative of the blade circulation curve and changes sign at the maximum load point along the radius.

Trailing vortex sheets produce a variation in the tangential direction that is relatively smooth at middle radii and much sharper near the tips. Viscosity produces a velocity defect that is much narrower than the potential effect in the mid blade area. In the tangential component, the velocity pulses due to viscous and potential effects have the same sign and are therefore additive. For the axial component the opposite condition occurs so that some cancellation occurs.

The bound thickness and loading effects only seem to be important at high Mach numbers and produce a distinctive pulse within the axial and tangential velocity waveforms. For the supersonic tip speed case, this bound effect changes to a propagating acoustic wave at the outer radii.

Noise

The noise theory accounts for the linear acoustic sources: monopoles for the thickness effect and dipoles for the loading effect. However, some degree of nonlinearity is included in the aerodynamic calculations used to evaluate the acoustic sources. The thickness source includes the displacement thickness of the blade boundary layer and the loading sources include the extra loading caused by vortex

flow. The extra loading at the tip from the tip vortex and the augmented lift effect from the leading edge vortex produce significant noise increases.

Comparisons of noise predictions with data were presented in 2 series. The first was the high Mach number data from the Jet Star flight tests of the SR-2 and SR-3 Prop-Fans. The second was acoustic wind tunnel data from the front rotor of the CRP-X1 model running near the takeoff and climb conditions.

At the high Mach number conditions (0.5 to 0.8 Mach), directivity shapes and levels were generally well predicted, particularly at the highest Mach numbers. Plots of peak sideline noise with increasing flight Mach number are also well predicted for both the SR-2 and SR-3 Prop-Fans. These plots (Figures 60 and 61) increase monotonically with Mach number and exhibit only a slight reduction in slope at the high Mach number ends of the curves. There is no reason from the Jet Star microphone boom data or from theory to expect a noise reduction with increased Mach number if shaft power coefficient is held constant.

For the data at takeoff and climb conditions, agreement with test directivity and shape was also generally good. There is a general tendency to underpredict by 2 to 3 dB. This lack of agreement is believed to be related to deficiencies in the vortex loading models used. It appears that these models must be refined to address the noise characteristics found in Prop-Fan measurements. The first work in vortex modelling should be in the aerodynamic performance area as described above.

Wing and Boundary Layer Shielding

For studies of these effects, the twin engine, tractor, wing mount configuration shown in Figure 73 was used. The wing can provide significant shielding provided that the starboard propeller rotates counterclockwise and the port propeller rotates clockwise as viewed from the front. Reductions up to 5 dB for the BPF fundamental and higher for the higher harmonics are predicted along the line of windows at locations aft of the wing leading edge.

Shielding of the noise at the fuselage surface by refraction in its boundary layer is inconsequential at Mach numbers below cruise values. However, at 0.8 Mach, substantial benefits occur at locations forward of the plane of rotation. These conclusions are based on a compact thickness source model. This model should be refined to include loading sources and distribution of the sources over the chord and span.

It is concluded that, for propellers with directions of rotation chosen as described above, the combination of wing shielding at aft locations and boundary layer shielding at forward locations will reduce noise levels considerably compared to predictions based on free space levels plus amplification at the fuselage surface.

SECTION 9
APPENDIX
VORTEX LOAD MODELING

This appendix explains how the suction analogy used commonly to calculate vortex loading in wing aerodynamics has been applied to propellers. The intent was to adapt the methods of Polhamus (ref. 9) and Lamar (refs. 10,11,30) as directly as possible and to evaluate the results before attempting any refinements. It was shown in the main text that this was reasonably successful except that the extra mass induction caused by the vortex loading needs to be included in the momentum iteration for performance calculations. The load distribution method described below is used for both performance and for noise due to steady loading. No attempt has yet been made to deal with unsteady vortex loading. In the following, a brief review of wing vortex methods is given before the propeller application is descibed.

Background from Wing Methods

The three components of vortex lift are sketched in Figure 5. At the top, the flow separates at the leading edge and reattaches further downstream. The vortex trapped between the leading edge and the reattachment point has a reduced pressure that adds to the blade lift. Separation is enhanced by a sharp (i.e. thin) leading edge, sweep, and high loading. Sweep enables reattachment and permits operation at angles of attack where 2D airfoils would be well into stall. The middle sketch in Figure 5 shows the tip edge (or side edge) vortex. There too the flow separates and reattaches on the wing (or blade) upper surface and causes extra lift.

The leading edge vortex lift can be computed from the suction analogy developed by Polhamus and extended to the side edge vortex by Lamar. The suction analogy works as follows. With attached flow, leading edge thrust develops because flow accelerates to high speed from the stagnation point on the pressure side of the wing around the leading edge. In theory, the suction force is independent of leading edge thickness because the effect of smaller frontal area is offset by higher acceleration. In practice with sharp edges and high loading however, the flow separates as shown in Section A-A of Figure 5 and a vortex forms on the forward part of upper surface. The basic tenet of the suction analogy is that the magnitude of the additional lift force is the same as that of the leading edge thrust; only the orientation changes. Thus, if a means exists to compute leading edge thrust under the assumption of attached flow, the vortex lift is simply a vector with the same magnitude but oriented normal to the surface on which it acts. Exactly the same principle applies for the tip edge vortex as suggested in the middle sketch of Figure 5. In this case, the radial suction force is computed under the assumption of attached flow and then rotated into the direction normal to the blade upper surface.

Augmented lift, suggested by the bottom sketch in Figure 5 is slightly different. The idea here is that the leading edge vortex which forms and acts at the leading edge also sweeps across the tip and produces extra lift in that region. This effect was first recognized by Lamar (ref. 11) who applied it to clipped delta wings. Since Prop-Fan tips have similar geometry, it is assumed that the effect is valid for them also.

Application to Propeller Loading

The formula for computing leading edge thrust can be found in several textbooks or in Polhamus' paper (ref. 9). The procedure is to find the potential lift distribution using, for example, a panel method. The leading edge thrust is given directly by the strength of the singularity in the pressure distribution at the leading edge. The tip edge radial force is computed from a similar analysis as explained by Lamar (ref. 30). The procedure was also reviewed in the propeller context by Hanson in a paper resulting from this work (ref. 6). A limitation of the suction analogy method is that is only predicts a force per unit length along an edge. It provides no guidance regarding distribution in the direction normal to the edge. For example, for the leading edge vortex the method cannot give the chordwise distribution of the vortex lift force. For a first application to the propeller problem, it was decided to distribute these forces according to simple analytical functions whose widths are input to the computer program by the user. The resulting shape functions are defined as follows.

$F_{LE}(x)$ for the leading edge vortex

$F_R(z)$ for the tip edge vortex

and

$F_{AUG}(z)$ for the augmented vortex effect at the tip

where x is normalized chordwise distance and z is normalized radial distance.

Once the vortex loading components have been found by the above methods, they must be manipulated to get lift and drag coefficient distributions for performance computation. The results can be written down immediately by inspection of Figure 79 with the understanding that, by convention, lift and drag are the force components perpendicular and parallel to the local advance direction. In the figure α is the local 3 dimensional angle of attack, i.e. the angle between the advance direction and the chord. θ_{LE} is the angle between the camber line at the leading edge and the local advance direction. With these definitions, it follows that

$$C_L = C_{L_{pot}} + C_{SLE} \cos(\alpha-\theta_{LE}) + C_R F_R(z) \cos\alpha + C_{SAUG} F_{AUG}(z) \cos\alpha - C_{TLE} \sin(\alpha-\theta_{LE}) \quad \text{(A-1)}$$

and

$$C_D = C_{D_{skin}} + C_{D_{induced}} + C_{SLE} \sin(\alpha-\theta_{LE}) + C_R F_R(z) \sin\alpha + C_{SAUG} F_{AUG}(z) \sin\alpha + C_{TLE}\cos(\alpha-\theta_{LE}) \quad \text{(A-2)}$$

where

$C_{L_{pot}}$ is the potential lift as computed by the panel method

C_{SLE} is the leading edge suction coefficient

C_R is the tip radial force coefficient (ref. 6)

C_{SAUG} is the augmented vortex coefficient

C_{TLE} is the leading edge thrust coefficient

$C_{D_{skin}}$ is the skin drag coefficient from 2D airfoil tables

$C_{D_{induced}}$ is induced drag from Treftz plane analysis

From the form of Equations A-1 and A-2 it can be seen that the orientation of the lift from the leading edge vortex (via the coefficient C_{SLE}) is taken to be normal to the airfoil surface near the leading edge (through the α-θ_{LE} arguments in the sines and cosines). Similarly, the leading edge thrust, which is lost in the presence of vortex flow, would act parallel to the surface at the leading edge. Also, it can be seen from the terms with sines and cosines of α that the force from the tip edge vortex and the augmented effect are assumed to act normal to the chord line.

Some comments on computation of the vortex lift coefficients are in order. The radial suction coefficient C_R is a straightforward application of Lamar's theory as given in Reference 6. The result is a non-constant distribution of force along the tip edge. The leading edge suction coefficient C_{SLE} involves the leading edge sweep angle Λ as shown in Figure 80. First the leading edge thrust is computed using the potential lift from the panel method. This is considered to be the component in the relative air direction of the leading edge suction, which acts normal to the leading edge in the planform plane of Figure 80. Thus, the leading edge suction is given by the thrust divided by cosine Λ. It is this suction force that is rotated with constant magnitude to the surface normal direction.

The augmented lift is more difficult to adapt from wing methods because they depend on coefficients based on the uniform flight speed. For propellers, the variation in velocity along the span require modification of the method. Physically, the strength of the augmented lift vortex must be given by the amount of vorticity trailing into the downstream flow by the leading edge vortex. In the wing procedure, this is found from the spanwise average of the circulation in the leading edge vortex. Since the vortex lift is computed first from the potential solution, an equivalent circulation can be determined based on the relationship Lift = ρ_o U Γ_{vortex}, where ρ_o and U are the local density and advance ratio. The circulation for the leading edge vortex is averaged over the span, and the resulting lift is determined based on the density, advance velocity, and chord at an effective radius.

Equations A-1 and A-2 give the radial distributions of lift and drag coefficient for direct use in performance calculation. Equations for lift pressure coefficient to be used in noise calculations are similar except that the shape factor $F_{LE}(x)$ for the leading edge vortex force is used to distribute the pressure along the chord.

A comparison of the propeller vortex loading predictions with Lamar's wing theory was attempted by running a high advance ratio ($J=2\pi$) case. Lamar's calculation for a cropped delta wing are shown in Figure 81. Reading from the bottom, the 4 lift components are potential, side edge, leading edge, and augmented. Figure 82 shows the potential lift comparison and Figure 83 shows comparisons of the vortex loading components. Overall lift is shown in Figure 84. The vortex loading components are significantly underpredicted for reasons that are not understood at the present. It could be that computational problems develop when the propeller code is run at high advance ratio or it could be that there is a problem with the modeling. Vortex load estimates depend on the linear panel method being accurate at the blade edges; this needs to be checked. At any rate, any further work on the vortex loading models should address these issues.

SECTION 10

REFERENCES

1. Hanson, D. B., "Helicoidal Surface Theory for Harmonic Noise of Propellers in the Far Field", AIAA Journal, Vol. 18, No. 10, October 1980, pp. 1213-1220.

2. Hanson, D. B., "Influence of Propeller Design Parameters on Far-Field Harmonic Noise in Forward Flight", AIAA Journal, Vol. 18, No. 11, November 1980, pp. 1313-1319.

3. Hanson, D. B., Near-field Frequency Domain Theory for Propeller Noise", AIAA Journal, Vol. 23, No. 4, April 1985, pp.499-504.

4. Hanson, D. B., "Compressible Helicoidal Surface Theory for Propeller Aerodynamics and Noise," AIAA Journal, Vol. 21, No. 6, June 1983, pp. 881-889.

5. Hanson, D. B., "Compressible Lifting Surface Theory for Propeller Performance Calculation," Journal of Aircraft, Vol. 22, No. 1, January 1985, pp. 19-27.

6. Hanson, D. B., "Propeller Noise Caused by Blade Tip Radial Forces", AIAA Paper No. 86-1892, presented at AIAA 10th Aeroacoustics Conference, July 9-11, 1986, Seattle, Washington.

7. Vaczy, C. M. and McCormick, D. C., "A Study of the Leading Edge Vortex and Tip Vortex on Prop-Fan Blades," ASME Journal of Turbomachinery, Vol. 109, July 1987, pp. 325-331.

8. Bisplinghoff, R. L., Ashley, H., and Halfman, R. L., Aeroelasticity, Addison-Wesley Publishing Company, Reading, Massachusetts, 1955.

9. Polhamus, E. C., "A Concept of the Vortex Lift of Sharp-Edge Delta Wings Based on a Leading-Edge-Suction Analogy", NASA TN D-3767, 1966.

10. Lamar, J. E., "Prediction of Vortex Flow Characteristics of Wings at Subsonic and Supersonic Speeds," J. Aircraft, Vol. 13, No. 7, p. 490, 1976.

11. Lamar, J. E., "Some Recent Applications of the Suction Analogy to Vortex-Lift Estimates", NASA SP-347, Part II, pp. 985-1011, 1975.

12. Jeracki, R., Mikkelson, D. C., and Blaha, B. J., "Wind Tunnel Performance of Four Energy Efficient Propellers Designed for Mach 0.8 Cruise", NASA TM-79124, 1979.

13. Rohrbach, C., Metzger, F. B., Black, D. M., and Ladden, R. M., "Evaluation of Wind Tunnel Performance Testings of an Advanced 45 Degree Swept Eight-Bladed Propeller at Mach Numbers from 0.45 to 0.85", NASA CR-3505, March, 1982.

14. Stefko, G. L. and Jeracki, R. J. "Wind Tunnel Results of Advanced High Speed Propellers at Takeoff, Climb, and Landing Mach Numbers", NASA TM-87030, November, 1985.

15. Amiet, R. K., "Computer Programs for Calculation of the Forces on and Sound Produced by an Airfoil in a Turbulent Flow", UTRC Report # R76-111204-1, June 1976.

16. Jordan, P. F., "Reliable Lifting Surface Solutions for Unsteady Flow", AIAA Paper Number 78-228, AIAA 16th Aerospace Sciences Meeting, Huntsville, Alabama, January 1978.

17. Cohen, D., "Formulas for the Supersonic Loading, Lift, and Drag of Flat Swept-Back Wings with Leading Edges Behind the Mach Lines", NACA Report No. 1050, 1950.

18. Bushnell, P., "Measurement of the Steady Surface Pressure Distribution of a Single Rotation Large Scale Advanced Prop-Fan Blade at Mach Numbers from 0.03 to 0.78", NASA CR 182124.

19. Silverstein, A., Katzoff, S., and Bullivant, W. K., "Downwash and Wake Flow Behind Plain and Flapped Airfoils", NACA Tech. Rept. No. 651, 1939.

20. Hanson, D. B. and Patrick, W. P., "Near Wakes of Advanced Turbopropellers", Paper presented at Symposium IUTAM Aero et Hydro-Acoustique, Ecole Central de Lyon, France, July, 1985.

21. Brooks, B. M., "Analysis of Jetstar Prop-Fan Acoustic Flight Test Data", Hamilton Standard Engineering Report, HSER 8882, November, 1983.

22. Serafini, J. S., Sullivan, J. P., and Newman, H. E., "Laser-velocimeter measurements of an Advanced Turboprop", AIAA Paper # 81-1568, 1981.

23. Tillman, T. G., Simonich, J.C., and Wagner, J.H., "Hot Wire Measurements Downstream of a Prop-Fan", AIAA Paper No. 89-2698, July, 1989.

24. Magliozzi, B., Brown, P., and Parzych, D., "Acoustic Test and Analysis of a Counter-rotating Prop-Fan Model", NASA CR 179590, October 1987.

25. Carlson, L. A., "TRANDES",: a Fortran Program for Transonic Airfoil Analysis or Design," NASA Rept. CR-2821, 1977.

26. Cook, T. A., "Measurements of the Boundary Layer and Wake of Two Aerofoil Sections at High Reynolds Numbers and High-Subsonic Mach Numbers," ARC R&M No. 3722, Aeronautical Research Council of Great Britain, June 1971.

27. Tam, C. K. W. and Salikuddin, M., "Weakly Nonlinear Acoustic and Shock-wave Theory of the Noise of Advanced High-speed Turbopropellers", Journal of Fluid Mechanics, Vol. 164, pp. 127-154, 1986.

28. Dittmar, J. H., Jeracki, R. J., and Blaha, B. J., "Tone Noise of Three Supersonic Tip Speed Propellers in a Wind Tunnel", NASA TM 79167, June 1979.

29. Hanson, D. B. and Magliozzi, B., "Propagation of Propeller Tone Noise Through a Fuselage Boundary Layer", J. Aircraft, Vol. 22, No. 1, January 1985, pp 63-70.

30. Lamar, J. E., "Extension of Leading Edge Suction Analogy to Wings with Separated Flow Around the Side Edges at Subsonic Speeds", NASA TR R-428, October, 1974.

SECTION 11
LIST OF SYMBOLS

a - ratio of tip rotational speed to flight speed - π/J

b - blade section chord measured at constant radius

c_o - ambient speed of sound

$\underline{f}$ - body force in wave equation

h - section thickness distribution

i - $\sqrt{-1}$, also index for control points in radial direction when used as a subscript

j - index for radial mode shapes, R_j

k_o - reduced frequency - $\omega b/U$

$\bar{m}$ - index counting control points in chordwise direction - Figure 2

$\bar{n}$ - index counting load elements in chordwise direction - Figure 2

p - disturbance pressure

q - source(monopole) strength, used to represent thickness effect

r - radius in cylindrical coordinates

t - time

t_b - ratio of section maximum thickness to chord

x - distance forward of pitch change axis in acoustic context, normalized chordwise distance γ/b in unsteady aerodynamic context

z_i - radius ratio at control point radius # i

B - number of blades

B_D - b/D, chord to diameter ratio

C_L - section lift coefficient

C_D - section drag coefficient

$C_{\bar{n}}$ - load element shape functions - see Figure 2

ΔC_p - coefficient of lift pressure

C_P - power coeffient, $SHP/(\rho_o N^3 D^5)$

C_T - thrust coefficient, thrust/($\rho_o N^2 D^4$)

D - propeller diameter

$K_{\mu\nu}$ - kernel function elements

L_ν - loading coefficient

M - flight Mach number

NCP - number of loading panels

NSM - number of spanwise mode shape functions

R - propeller tip radius

R_j - shape function for radial loading elements - see Figure 2

S - Sears function

U - blade section relative speed, - σV

V - flight speed

W_μ - vector of downwash angles at control points

X - normalized chordwise distance, zero at mid-chord

α - blade section angle of attack

$\beta_{3/4}$ - blade angle at 3/4 radius

γ - coordinate at constant radius in section advance direction

ϕ - angle in cylindrical coordinates to field point

μ - index for control points

ν - index for load elements

ρ_o - ambient density

σ - $\sqrt{1+a^2z^2}$, ratio of local blade section speed to flight speed at radius ratio z

ω - unsteady loading frequency times 2π

Ω - propeller angular speed, 2π times shaft rotation frequency

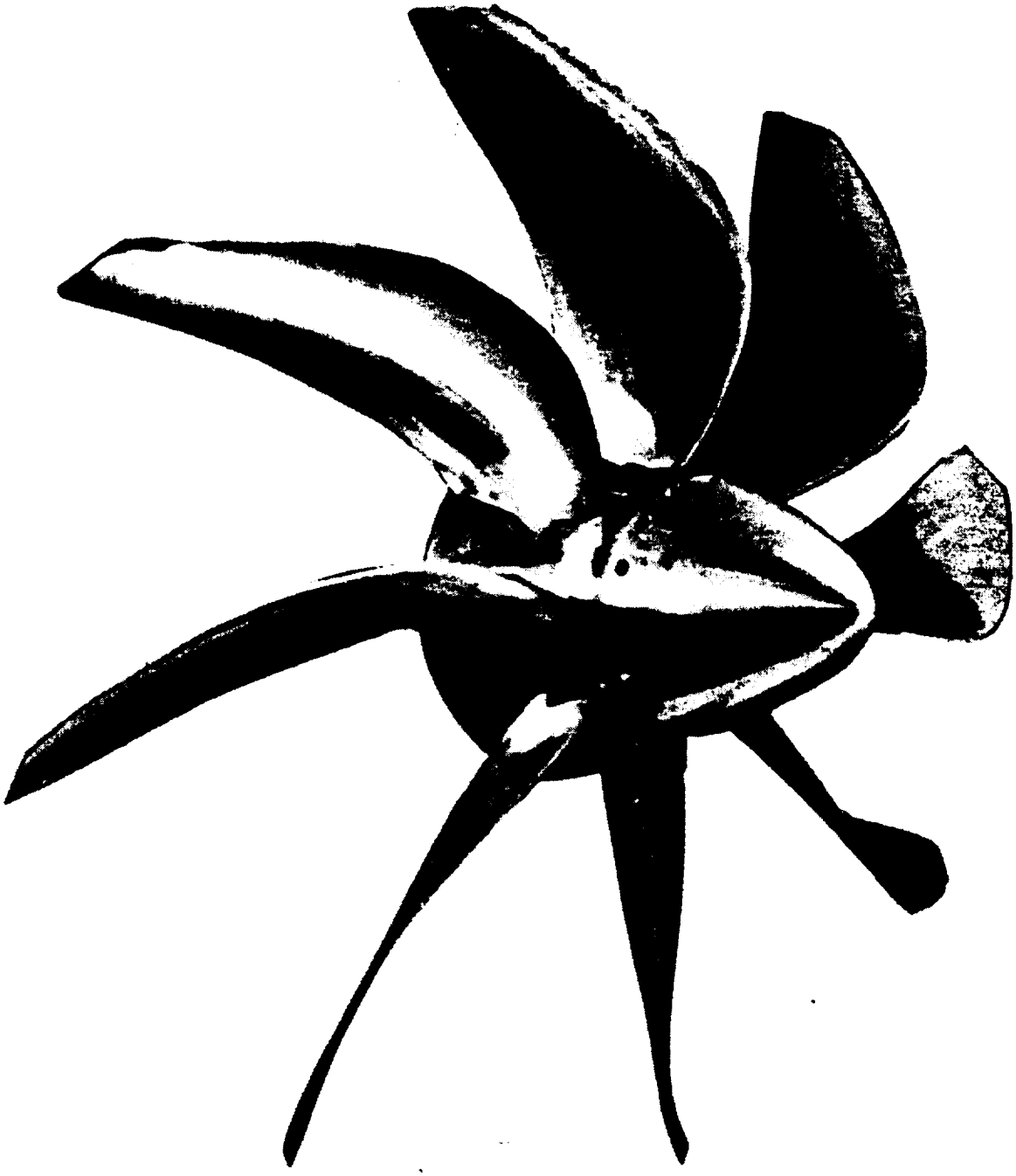

Figure 1. Prop-Fan model SR-3

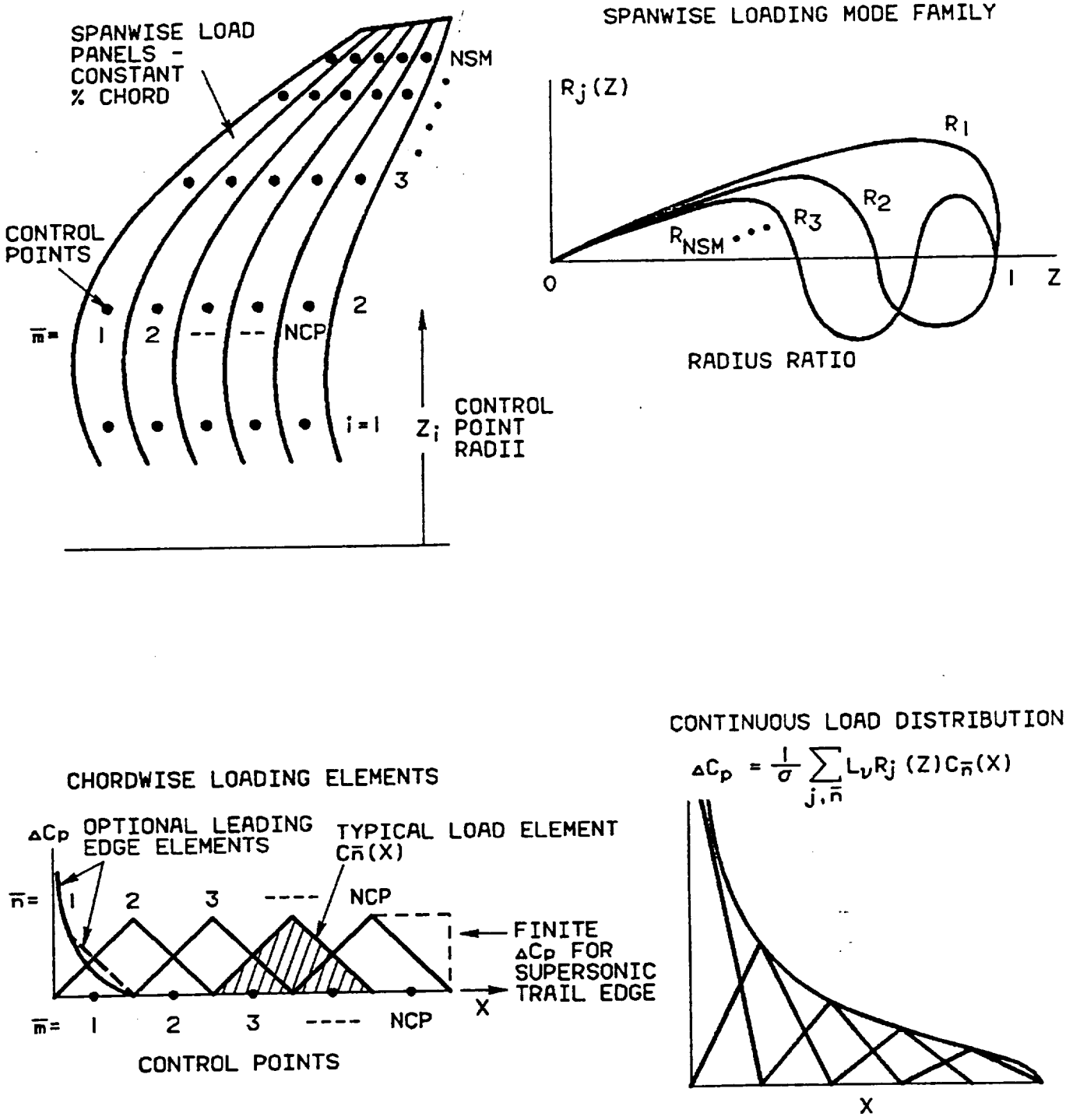

Figure 2. Load paneling system

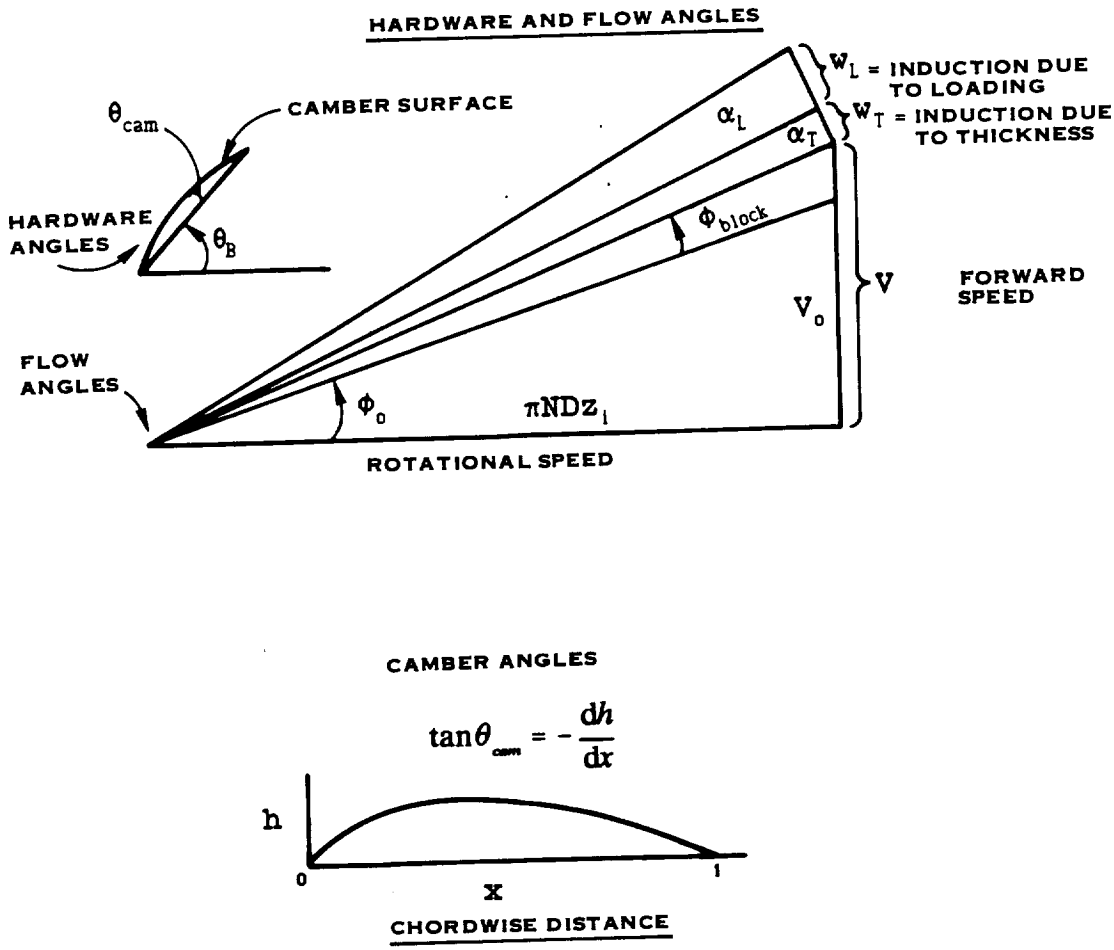

Figure 3. Angles used to define boundary conditions

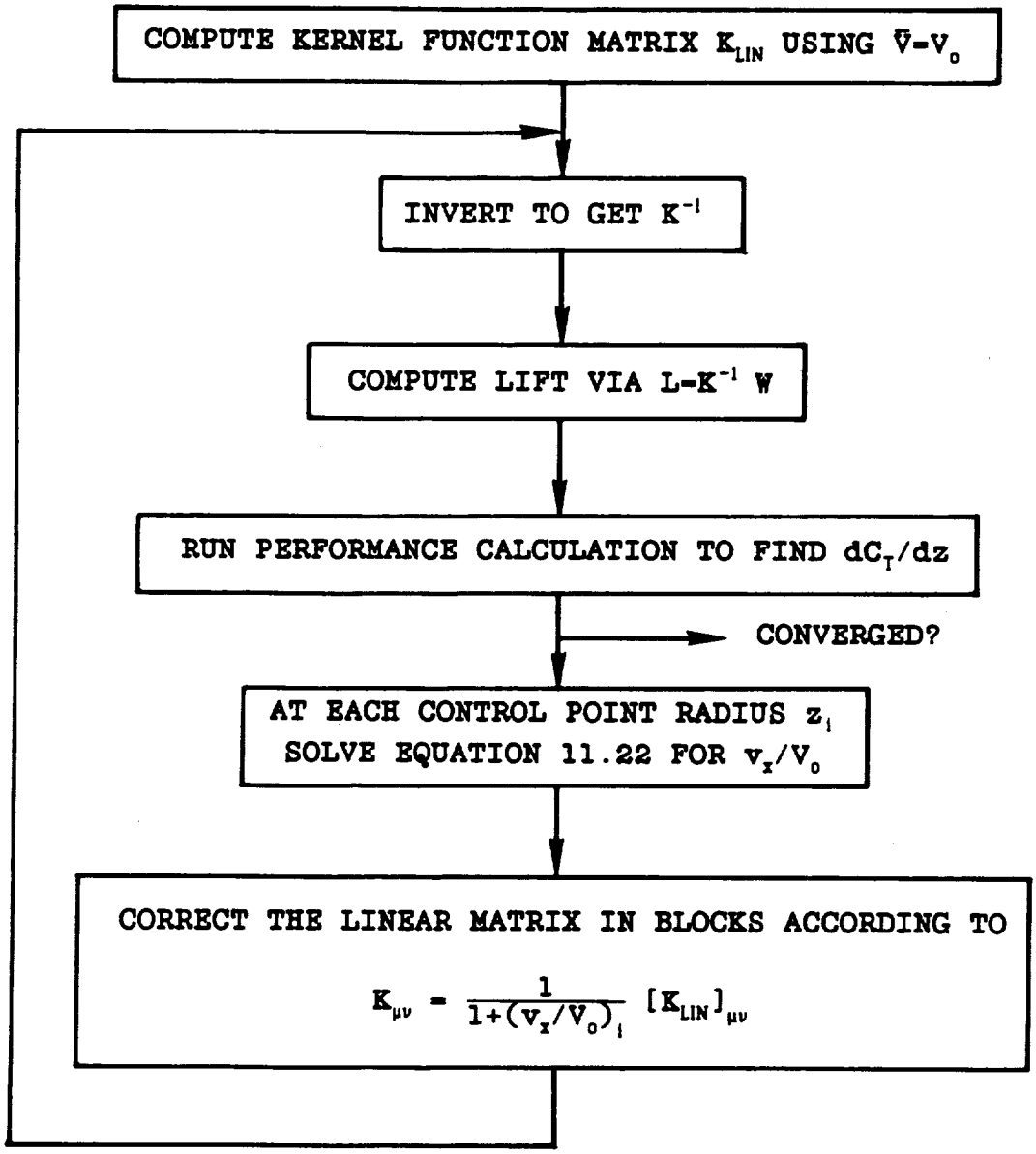

Figure 4. Iteration scheme for non-linearity associated with finite axial induction

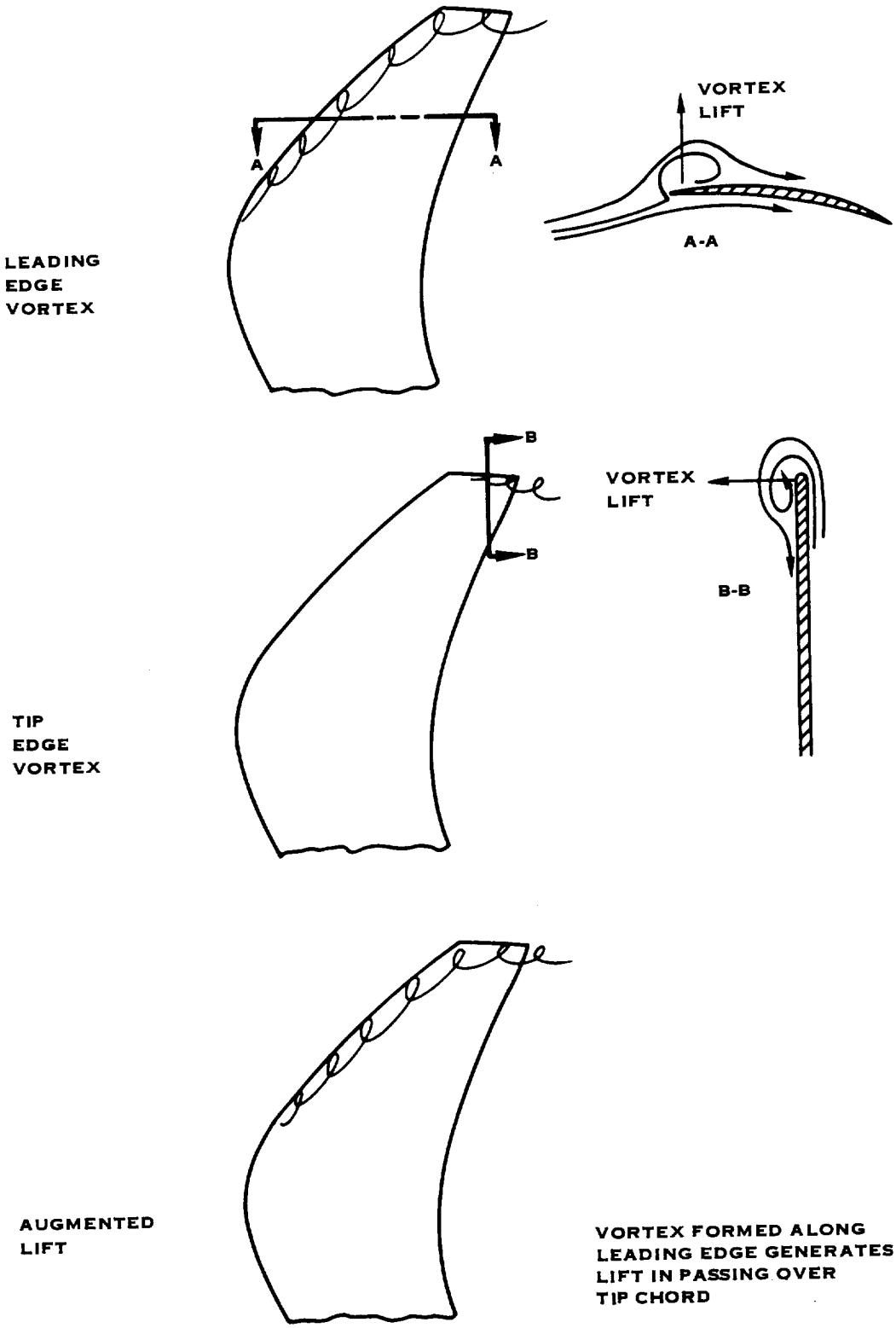

Figure 5. Vortex loading elements

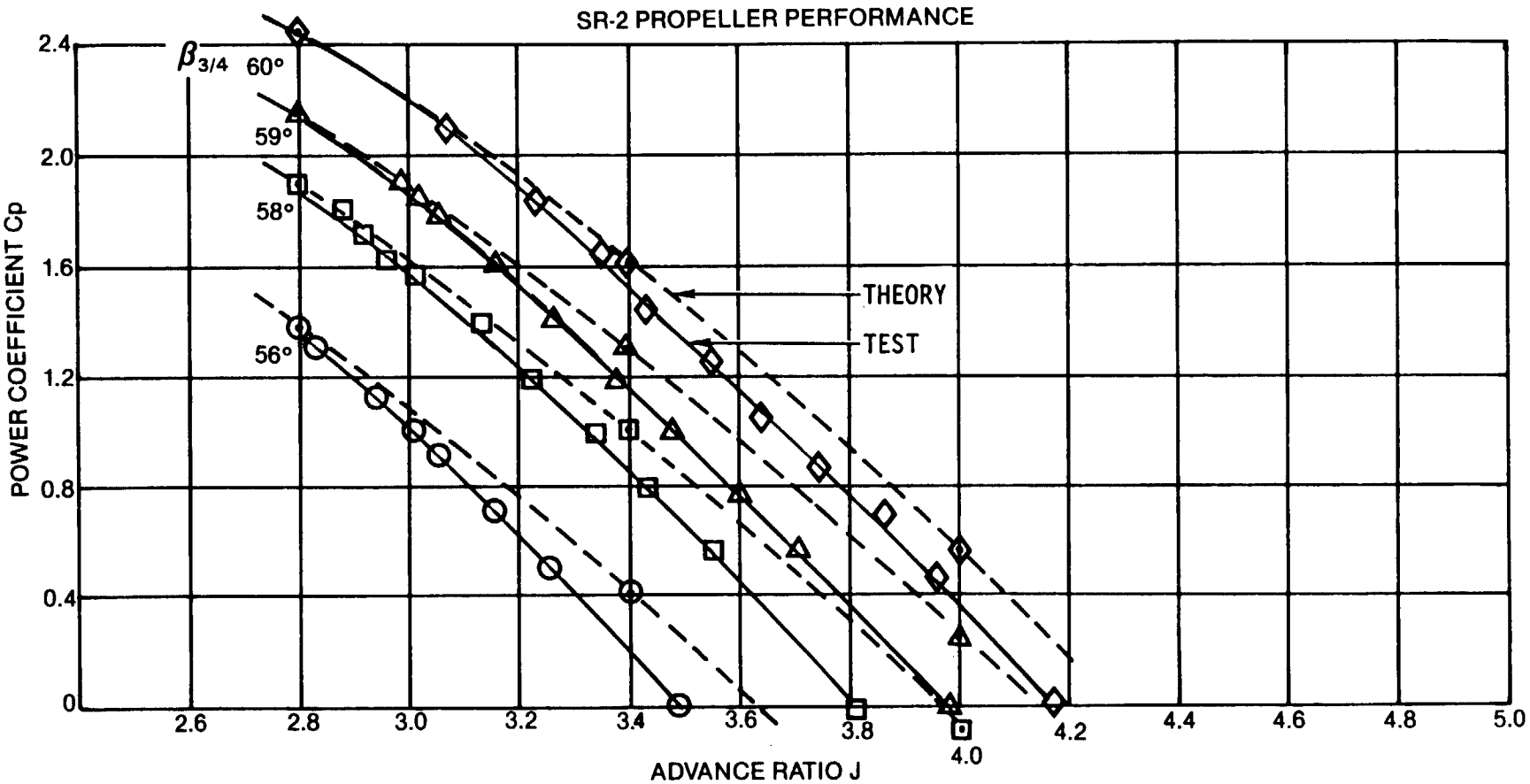

Figure 6. Power absorbtion comparison for SR-2 Prop-Fan at M=0.80 tunnel speed. Test reference: NASA TM-79124.

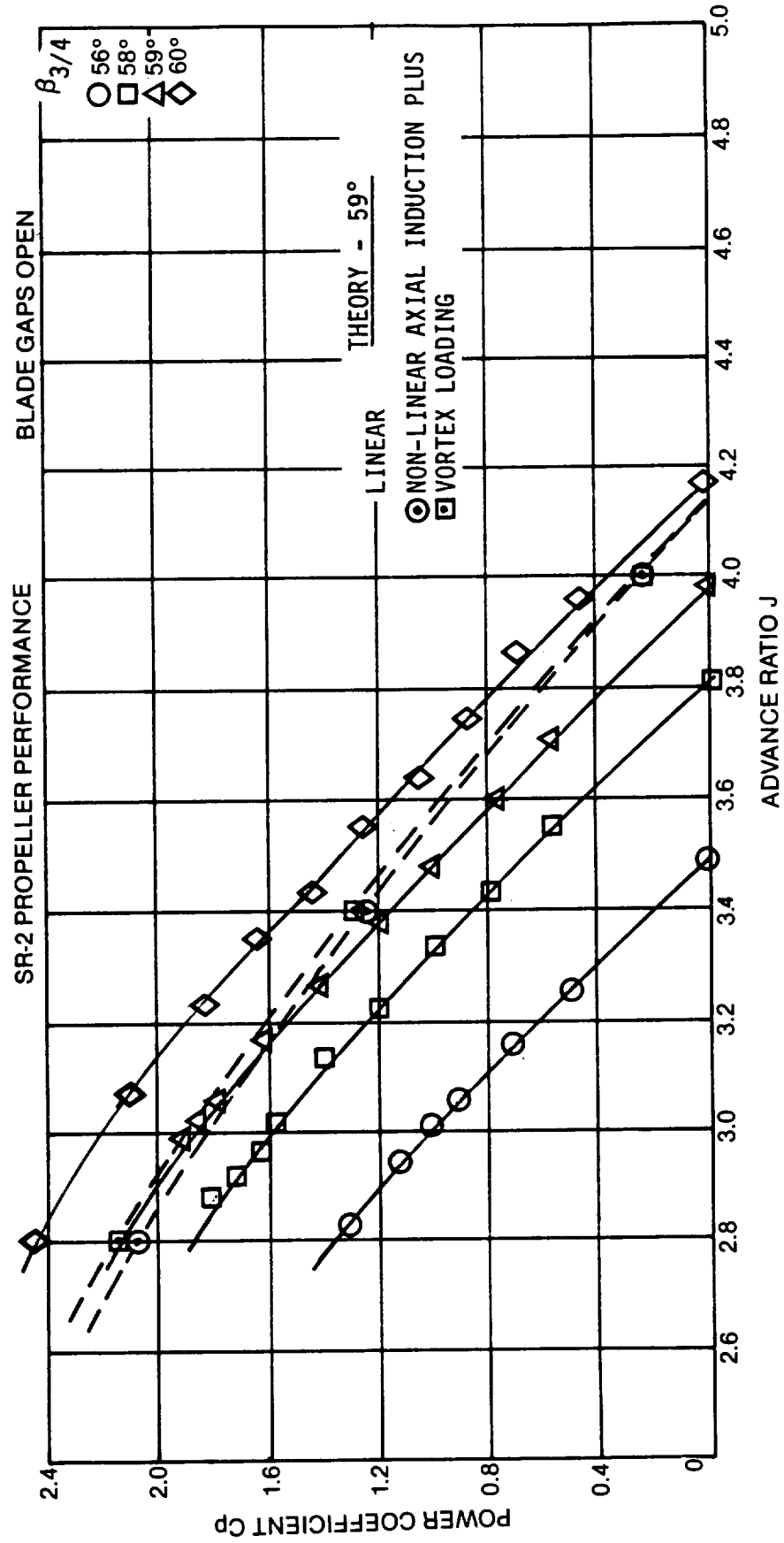

Figure 7. Effects of non-linearity on SR-2 at M=0.80.

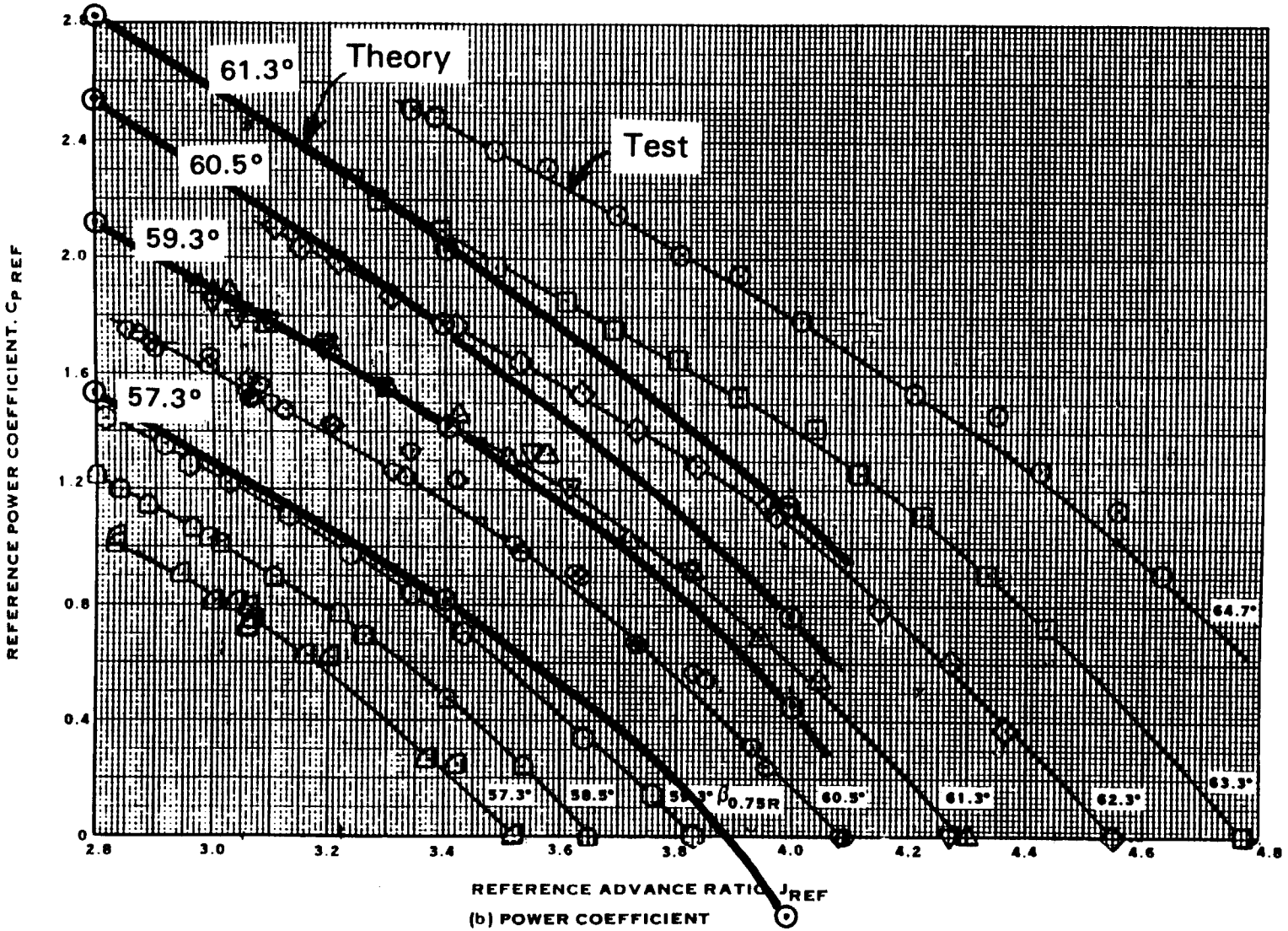

Figure 8. Power absorbtion comparison for SR-3 Prop-Fan at M=0.80 tunnel speed. Test reference: NASA CR-3505. Retention flexibility not included in blade angle labels.

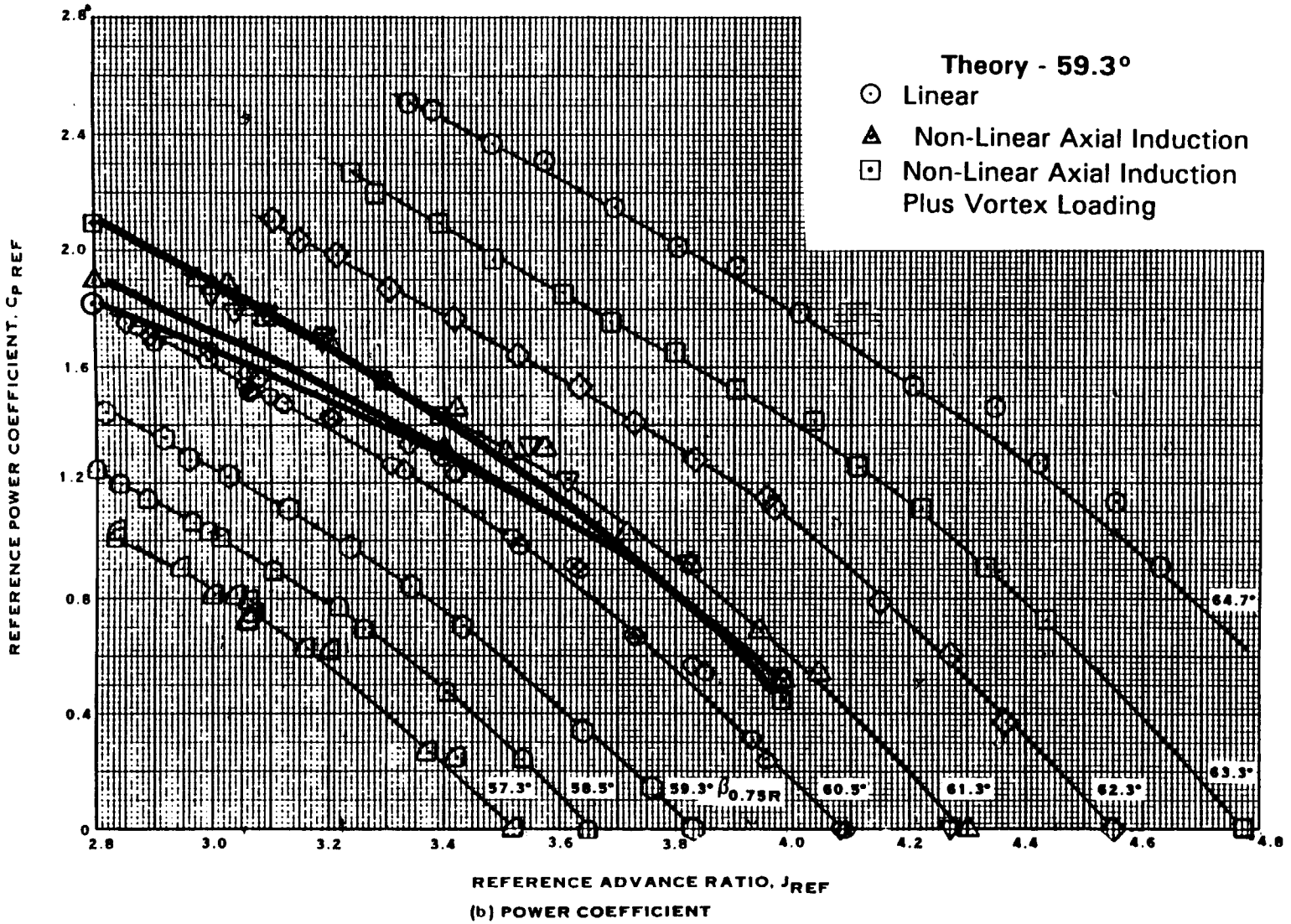

Figure 9. Effects of non-linearity on SR-3 at M=0.80.

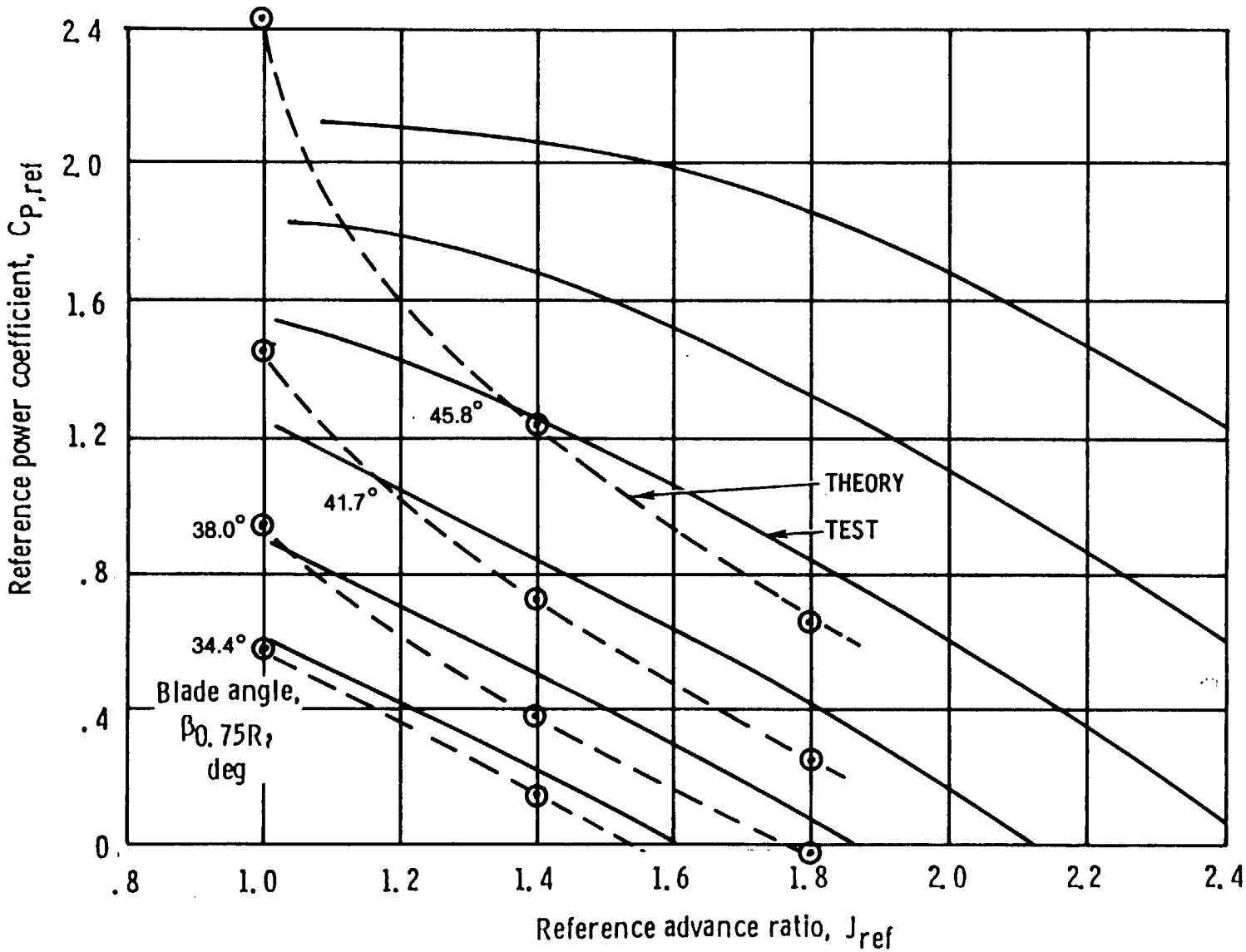

Figure 10 Power absorption comparison for SR-2 Prop-Fan at M=0.27 tunnel speed. Test reference: NASA TM-87030.

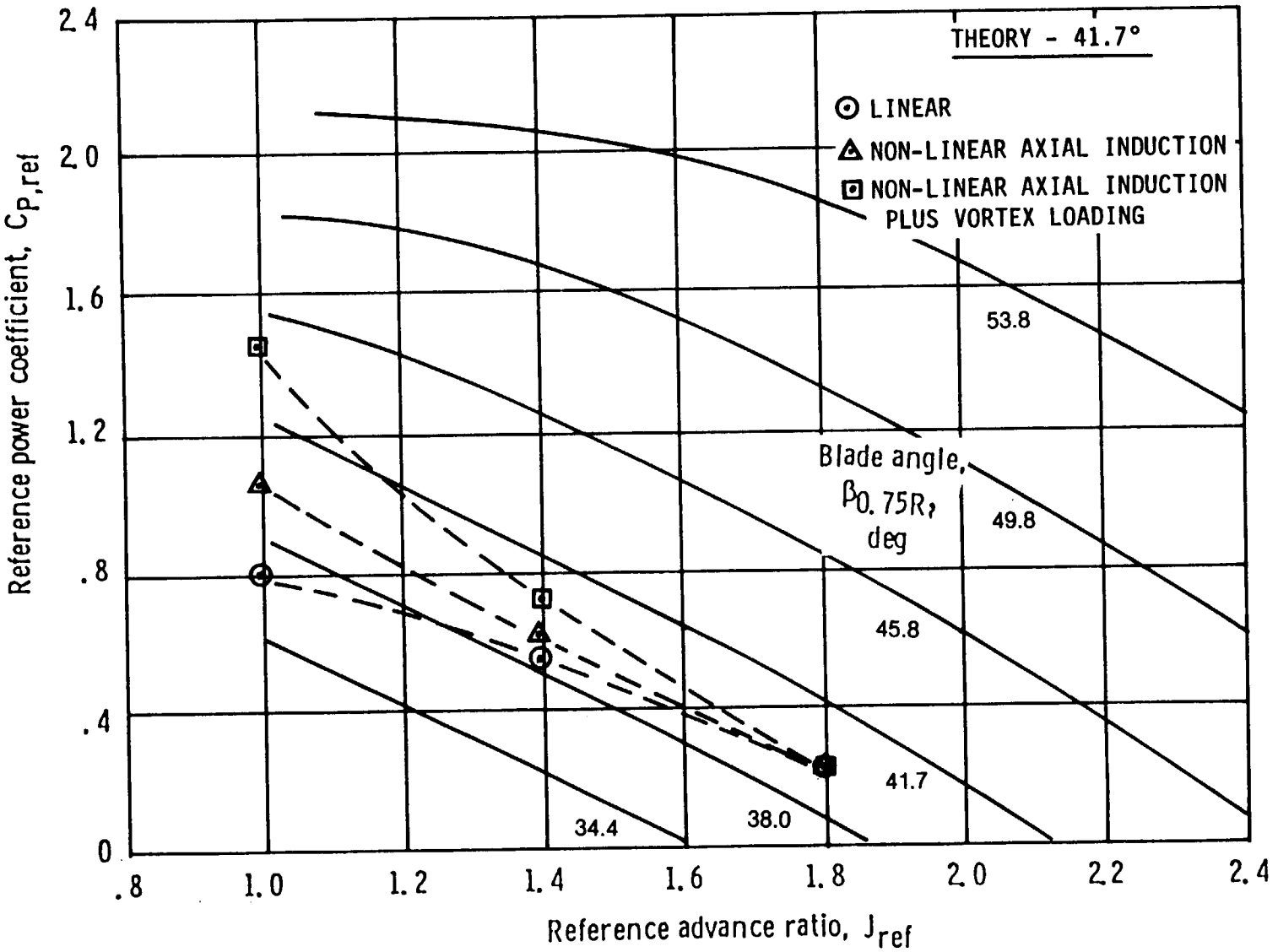

Figure 11 Effects of non-linearity on SR-2 at M=0.27

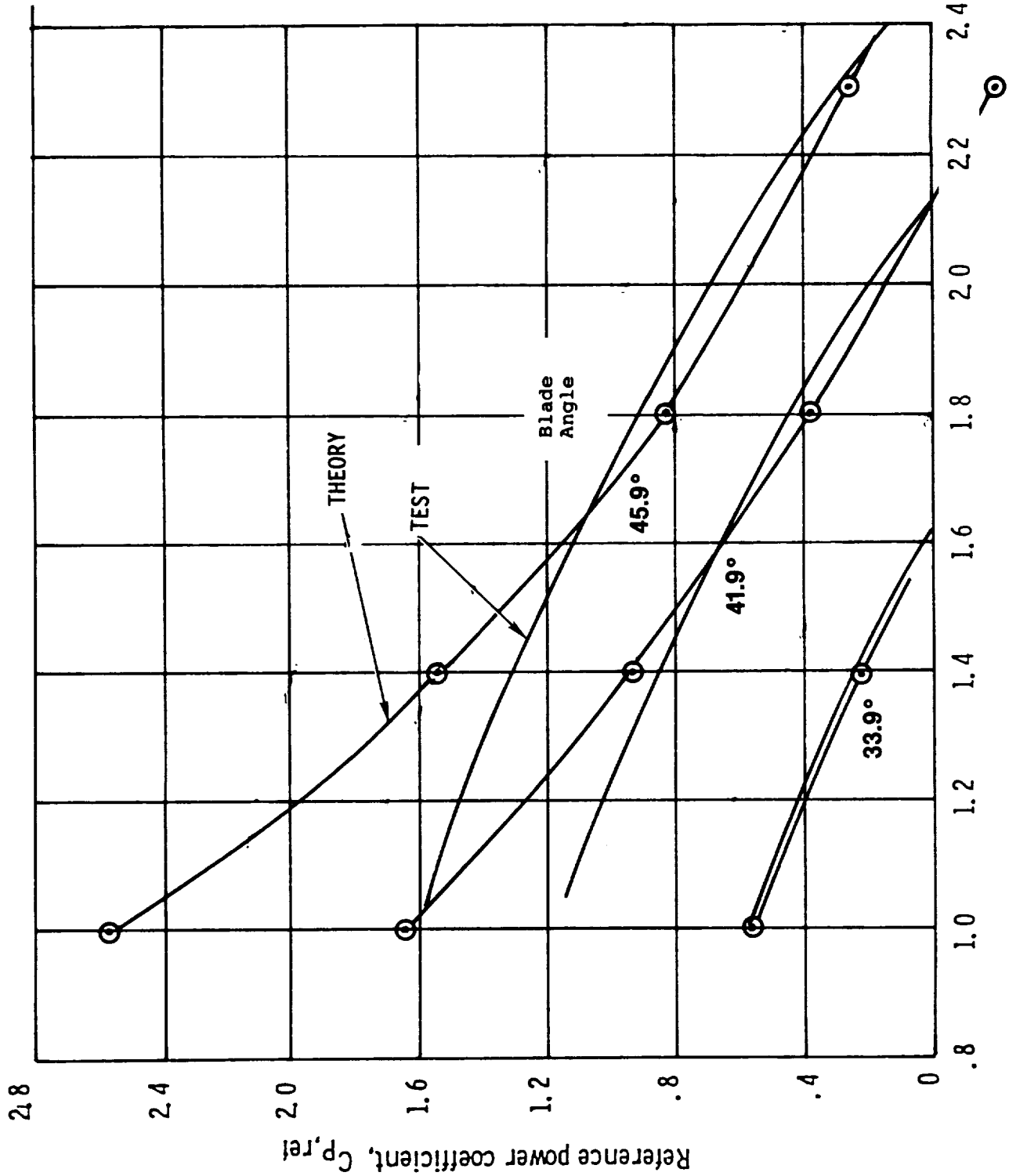

Figure 12 Power absorption comparison for SR-3 Prop-Fan at M=0.27 tunnel speed. Test reference: NASA TM-87030.

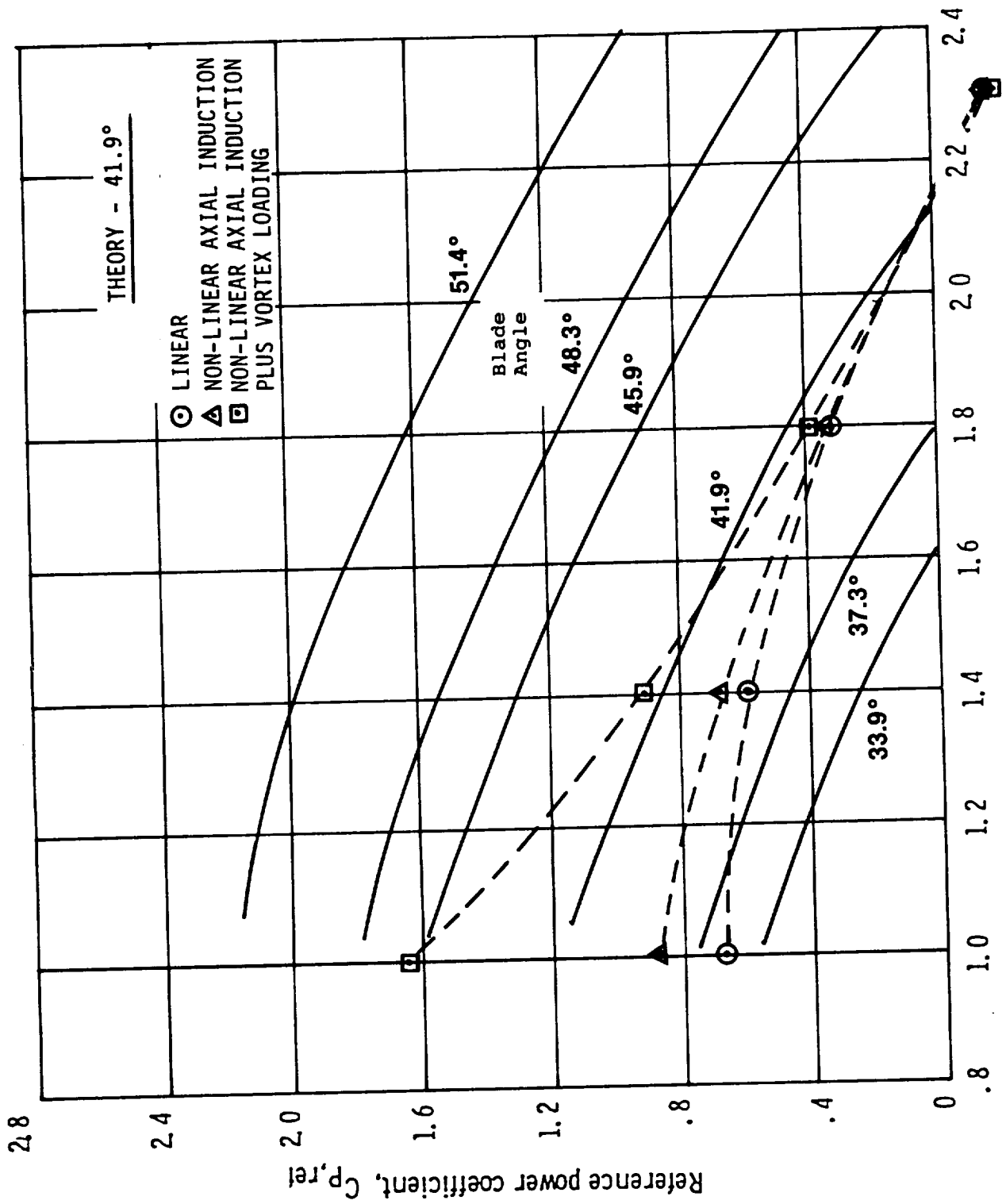

Figure 13 Effects of non-linearity on SR-3 at M=0.27.

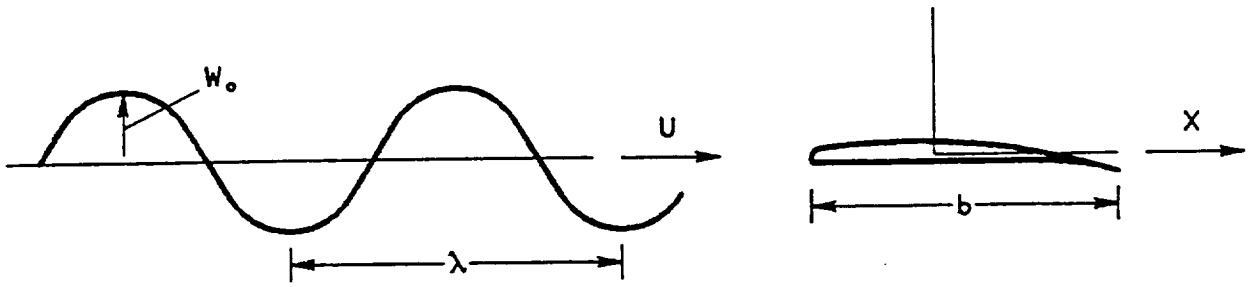

GUST: $W = W_o \, e^{i\omega(t-x/U)}$

REDUCED FREQUENCY: $k_o = \frac{\omega b/2}{U} = \pi \frac{b}{\lambda}$

ANGLE OF ATTACK: α = ARCTAN W_o/U

UNSTEADY LIFT COEFFICIENT: $C_L = 2\pi\alpha S(k_o)$

SEARS FUNCTION: $S(k_o)$

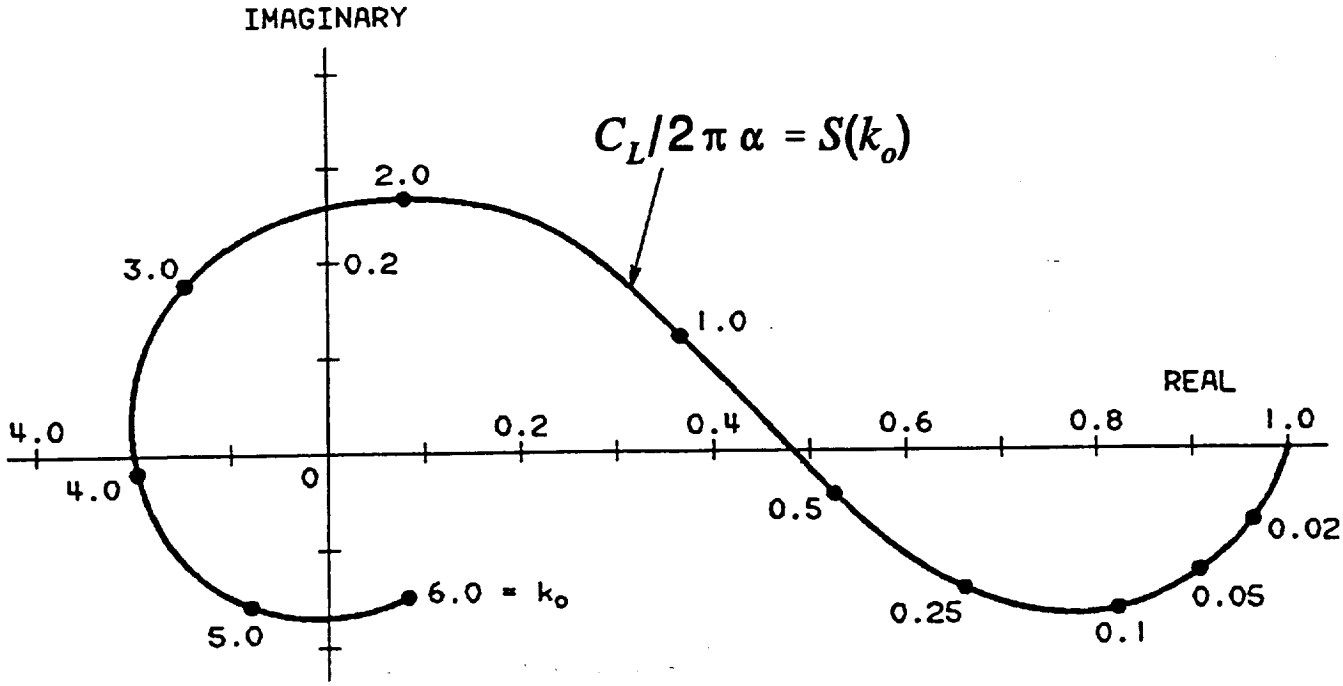

Figure 14 Airfoil/gust interaction problem for Sears theory. 2D, Incompressible.

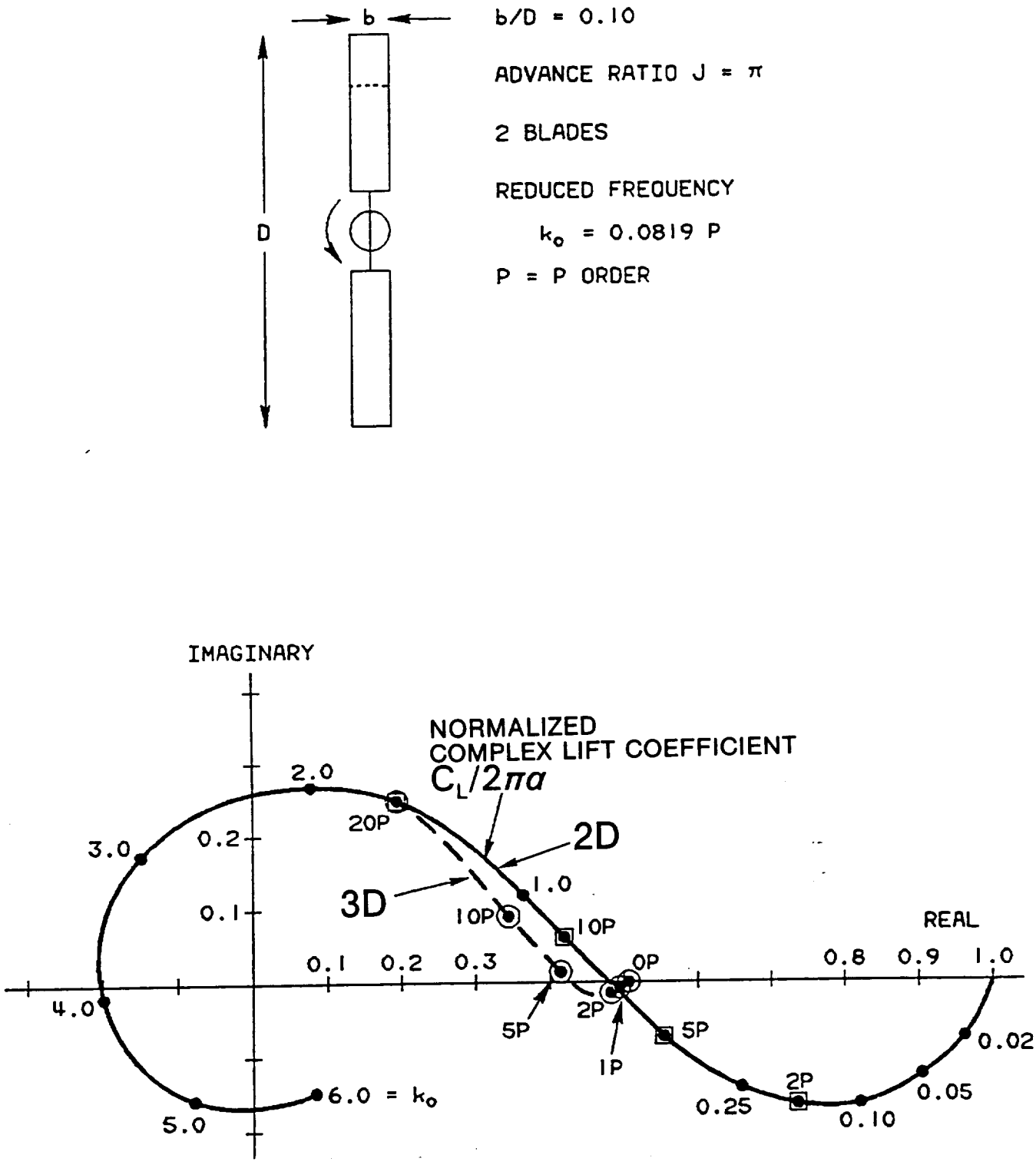

Figure 15. Propeller blade/gust interaction problem for 3D analysis. Incompressible.

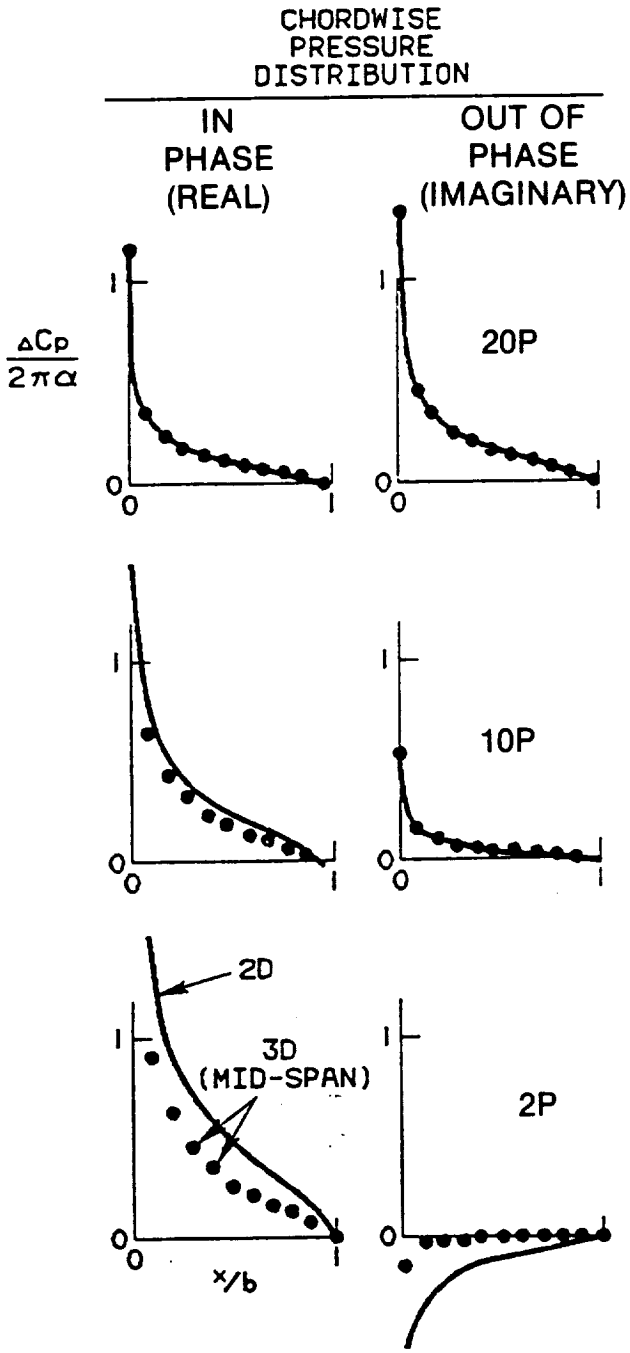

Figure 16. Unsteady pressure coefficients. 3D versus 2D.

ADVANCE TRIANGLE

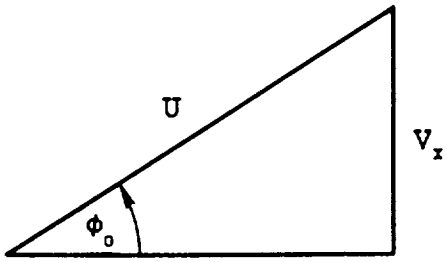

$\Omega r = \pi NDz$

$$\tan \phi_0 = \frac{V_x}{\pi NDz} = \frac{J}{\pi z} = \frac{1}{az}$$

INFLOW TRIANGLE

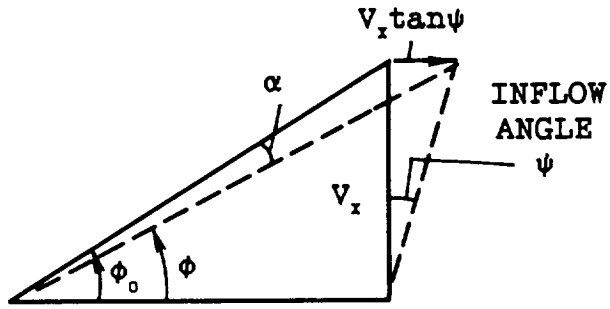

πNDz

$$\tan \phi = \frac{V_x}{\pi NDz + V_x \tan \psi} = \frac{1}{az + \tan \psi}$$

$$\alpha = \tan^{-1}\phi_0 - \tan^{-1}\phi$$

z	$\alpha = W_0$
0.30	2.70°
0.60	2.12
0.80	1.75
0.90	1.58
0.97	1.48
1.00	1.42

for
$J = 3.057$
$\psi = 3°$

where
z = radius ratio
$a = \pi/J$

Figure 17 Input preparation for SR-3 design point with 3 degree angular inflow.

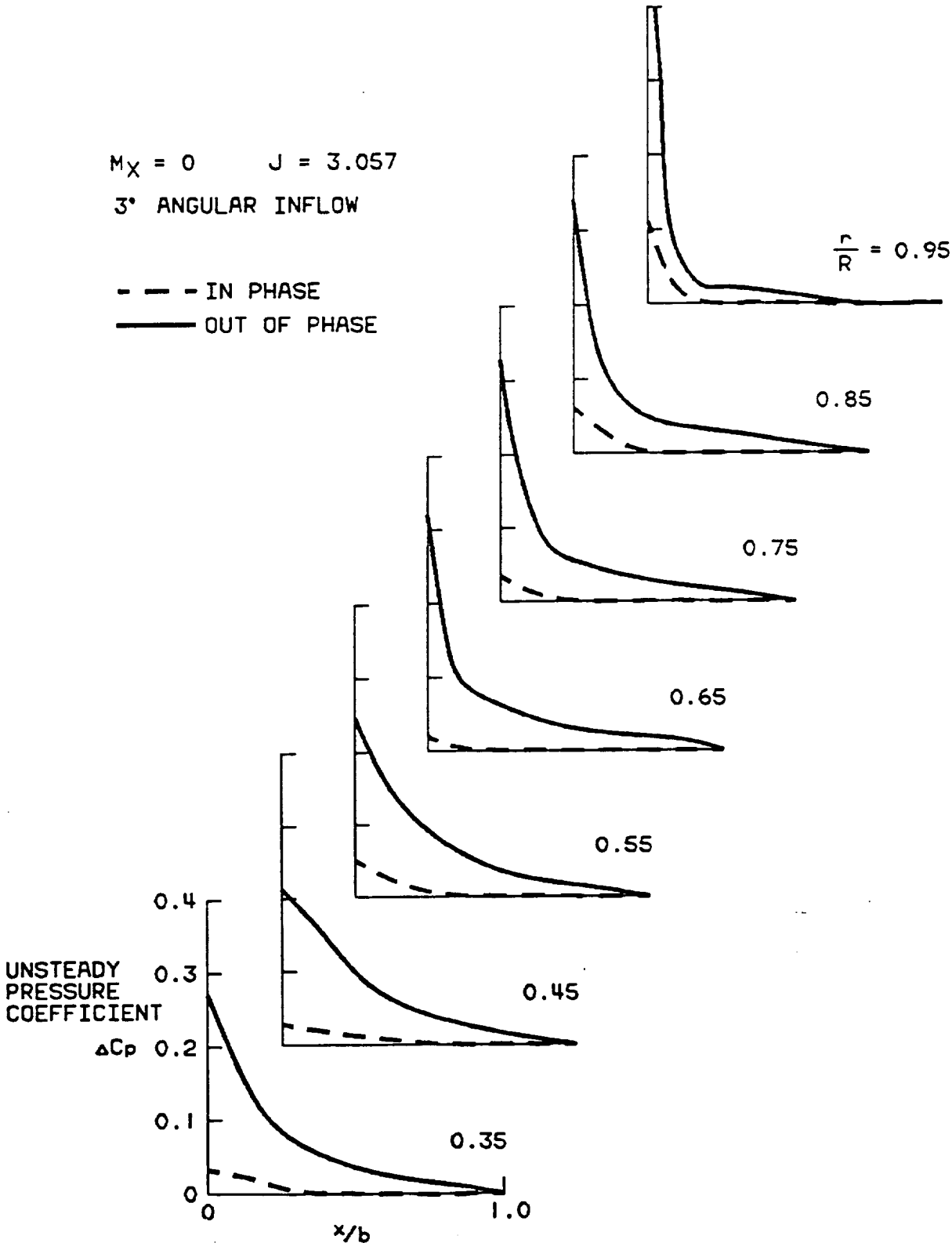

Figure 18. Unsteady loading due to angular inflow on SR-3 Prop-Fan. Incompressible.

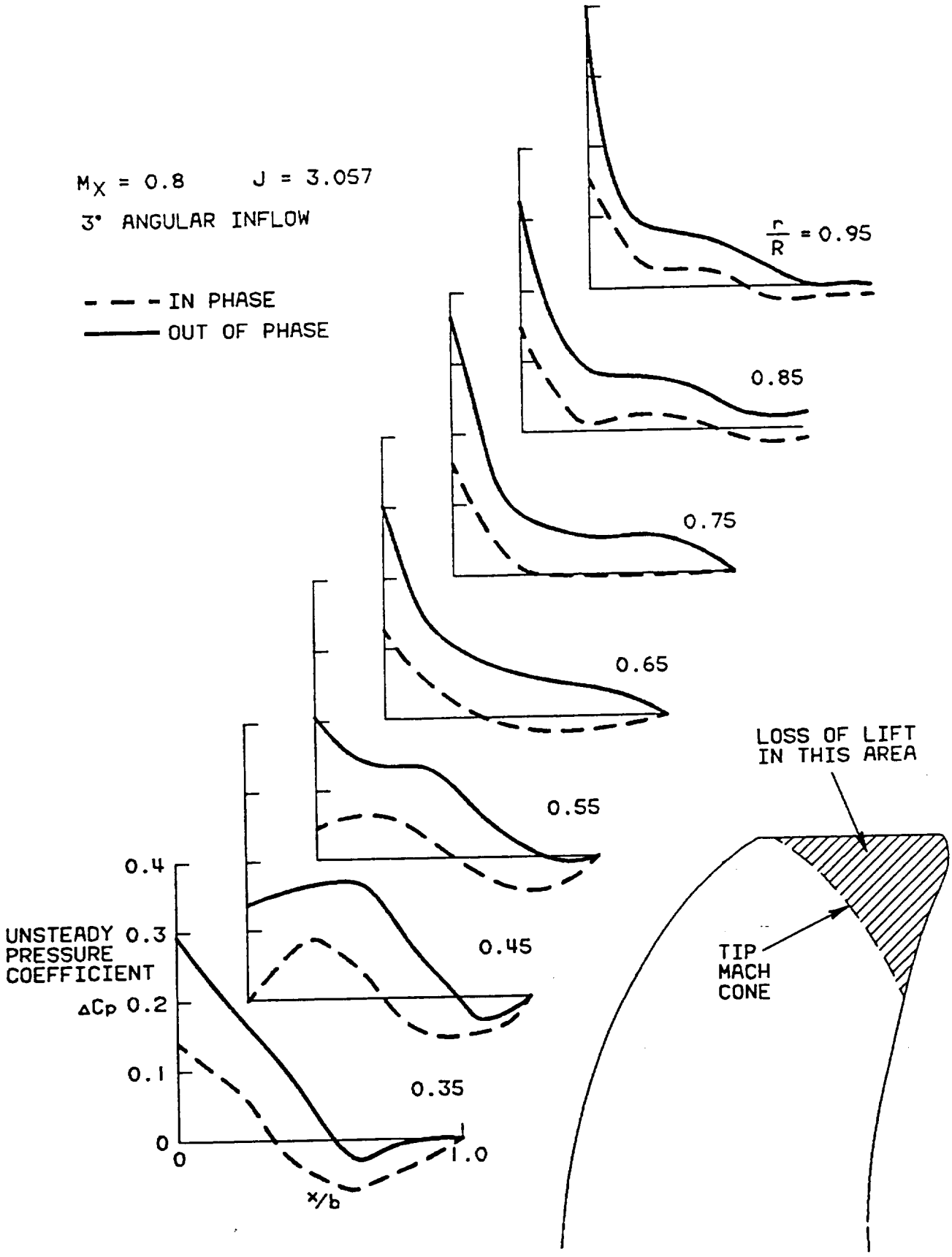

Figure 19. Unsteady loading due to angular inflow on SR-3 Prop-Fan. Compressible.

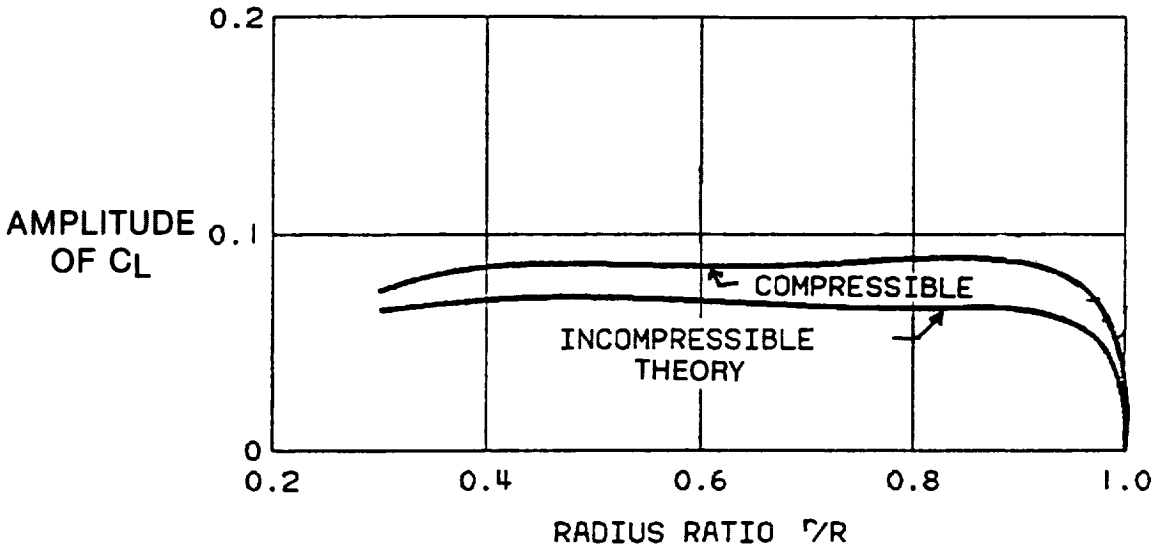

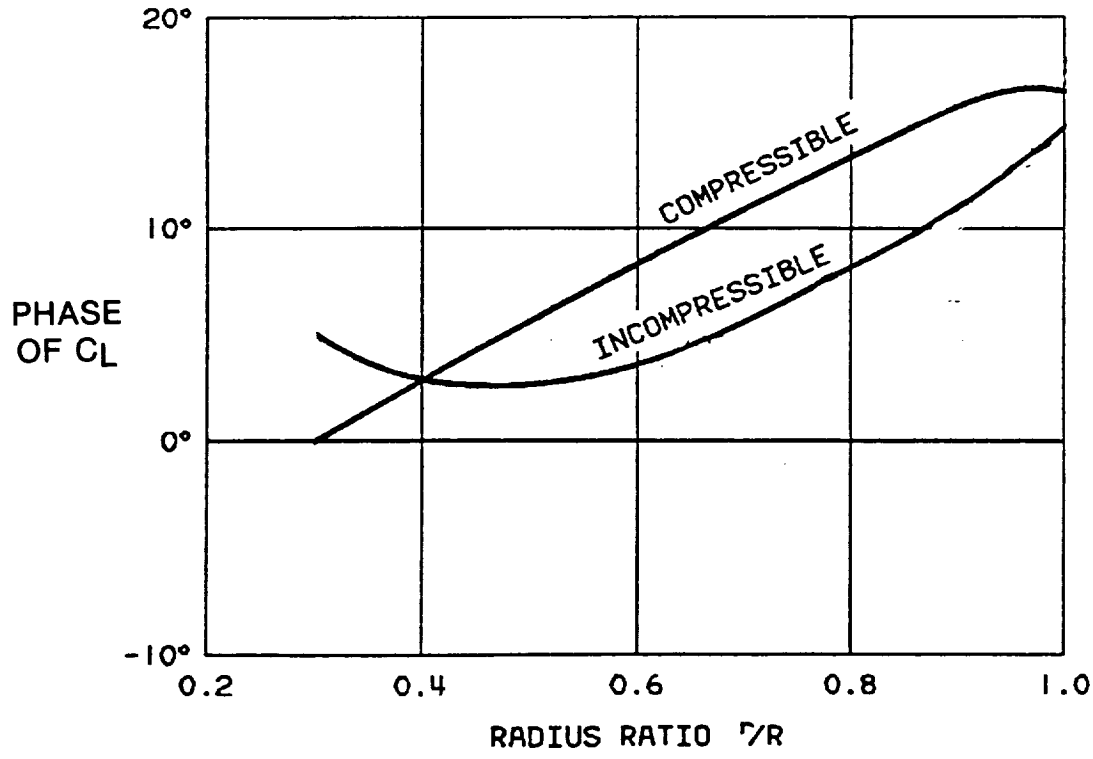

Figure 20. Lift coefficient harmonic at shaft rotation frequency- SR-3 design point.

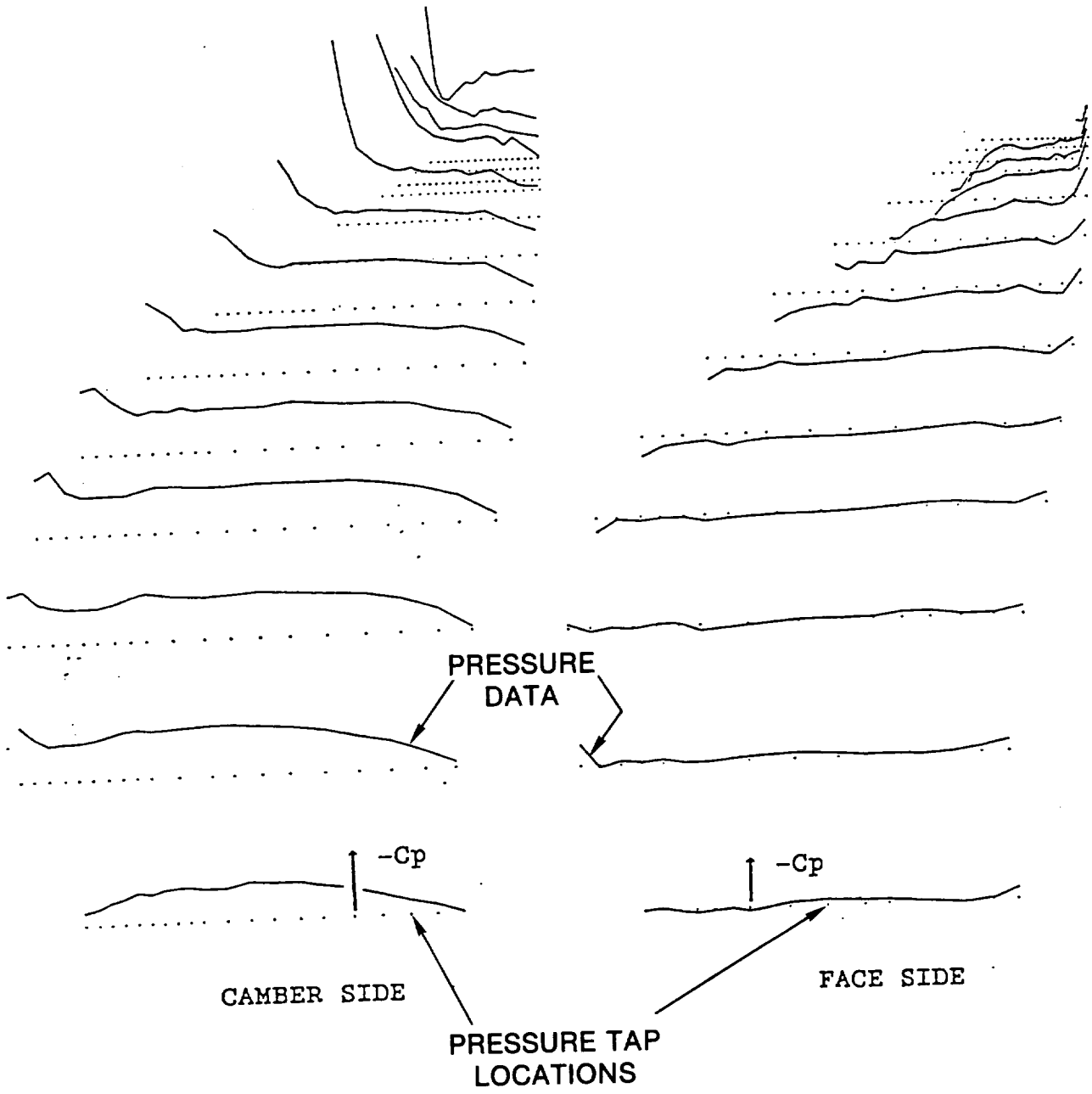

Figure 21. Measured blade pressure distribution on 2 blade SR-7 Prop-Fan in Modane S1 wind tunnel. Mach number = 0.50, Advance ratio = 3.067, Power coefficient = 0.361.

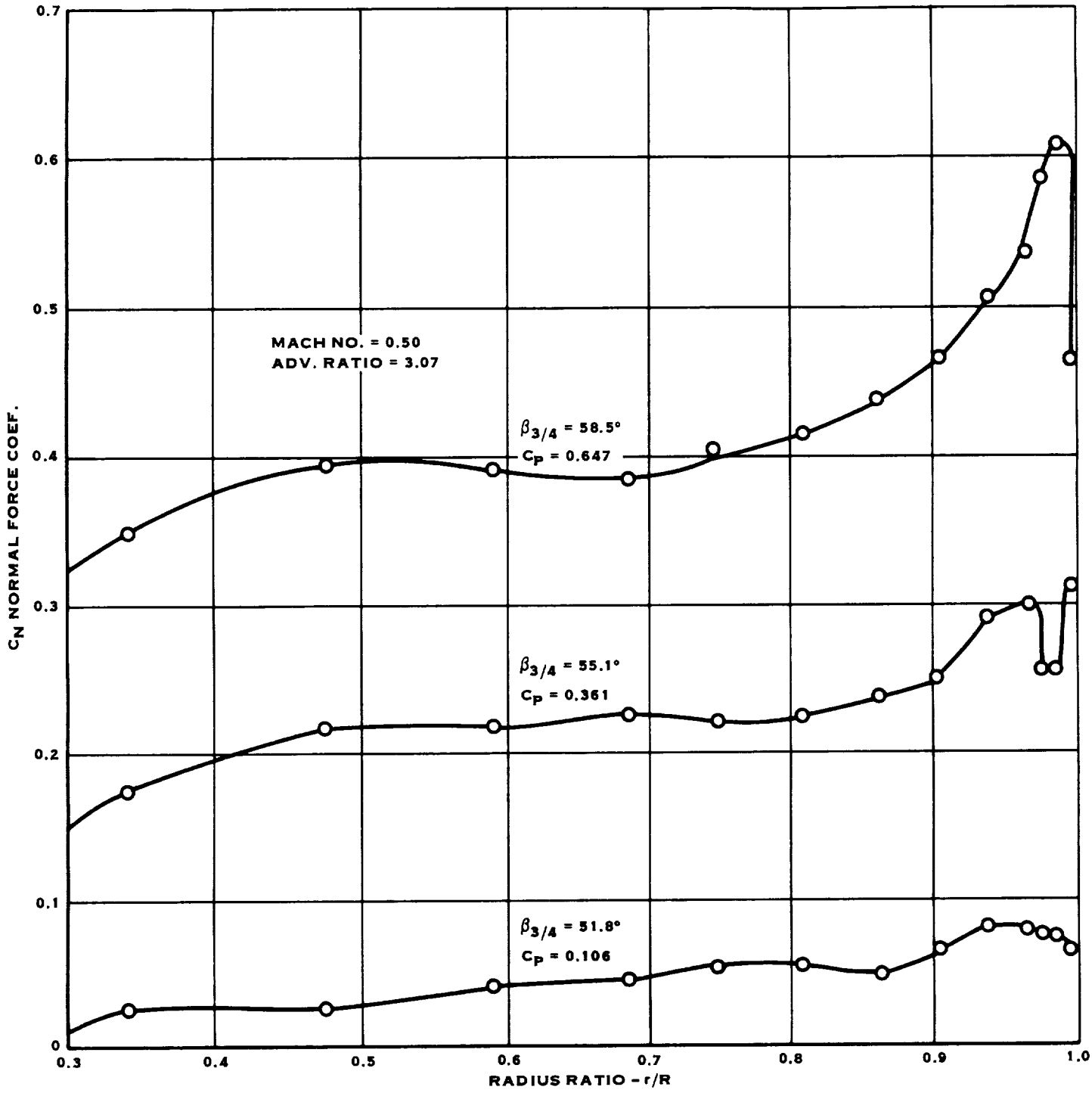

Figure 22. Section normal force coefficient for 2 blade SR-7 Prop-Fan in Modane test. Design loading per blade is matched by middle curve.

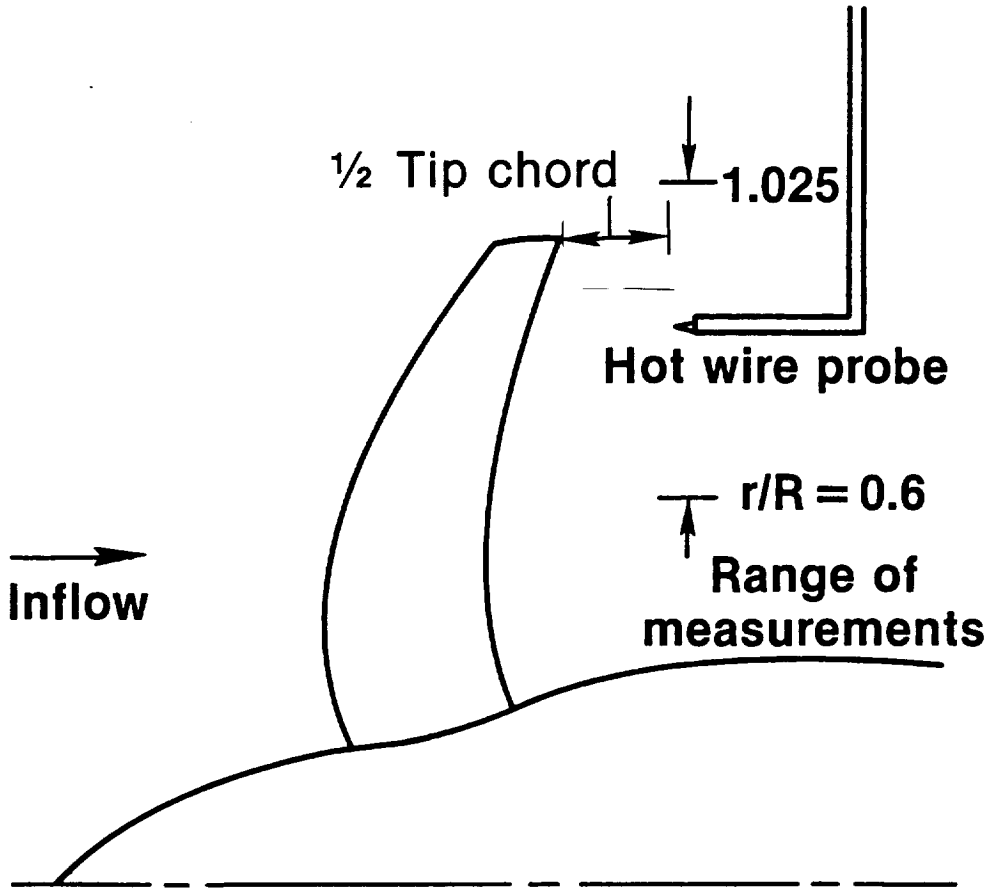

Figure 23 Range of probe traverse for 2 blade SR-3 test in UTRC wind tunnel. Traverse was in one plane passing ½ chord downstream of blade tip.

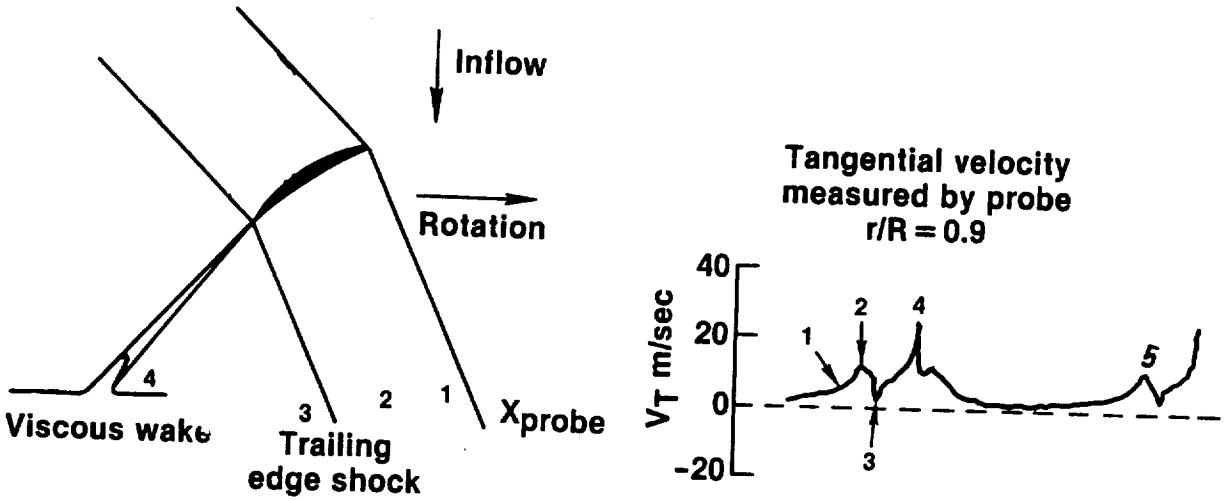

Figure 24 Relation between blade flow features and hot wire trace

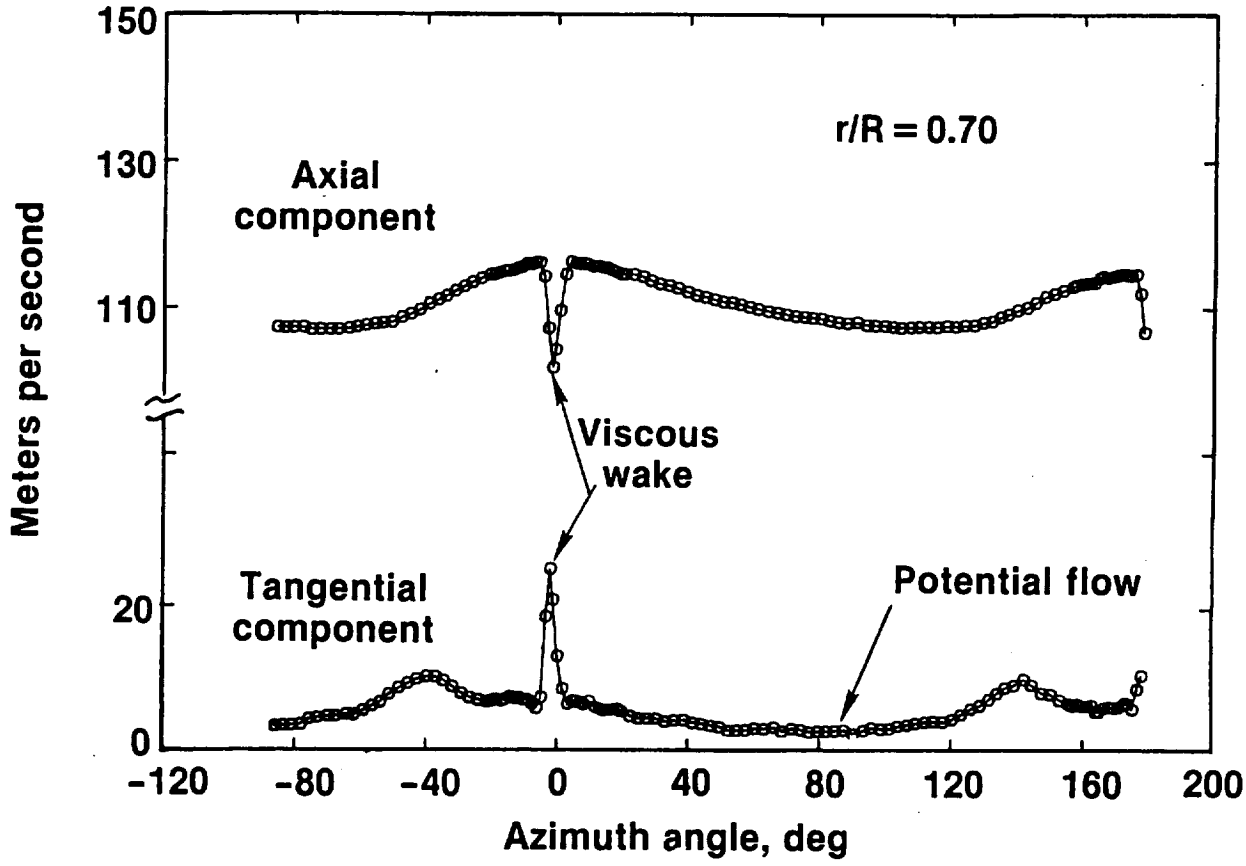

Figure 25 Axial and tangential velocity traces at r/R = 0.70

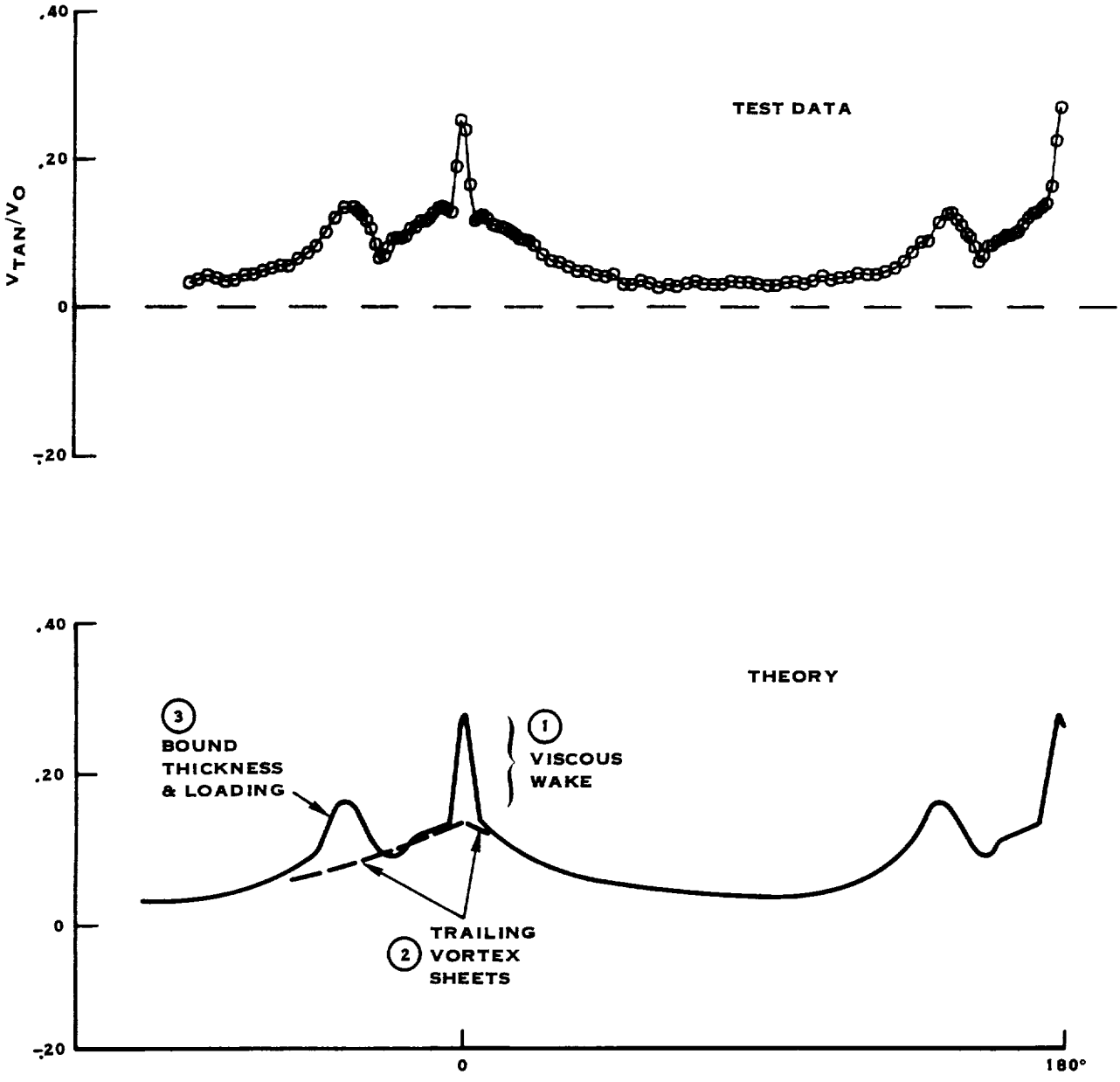

Figure 26 The three components of the wake theory (at r/R 0.85)
1. viscous
2. trailing vortex sheets (far potential wake)
3. bound thickness and loading (near potential field)

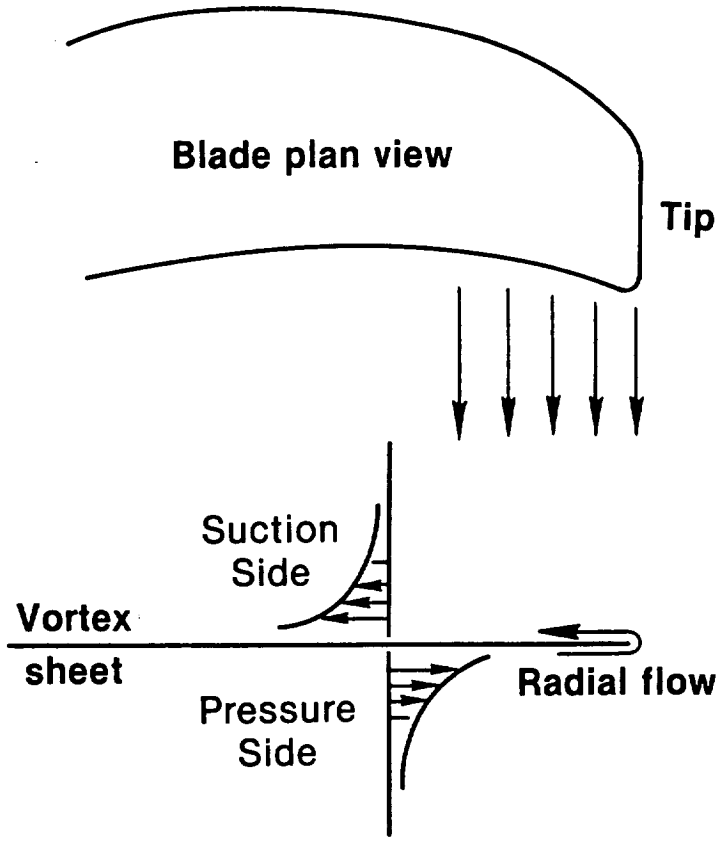

Figure 27 Vortex sheet and radial flow

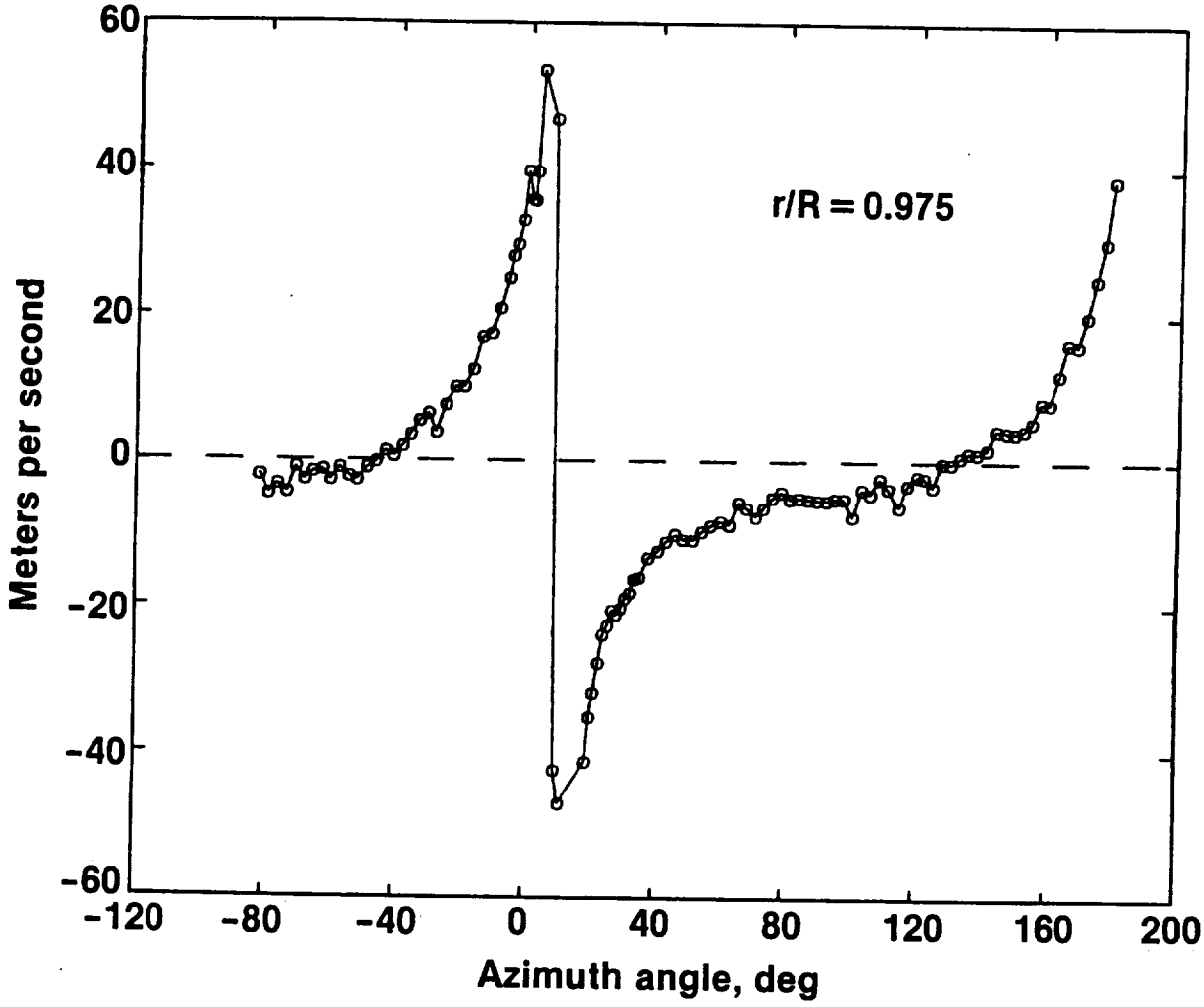

Figure 28 Measured radial velocity component at r/R = 0.975

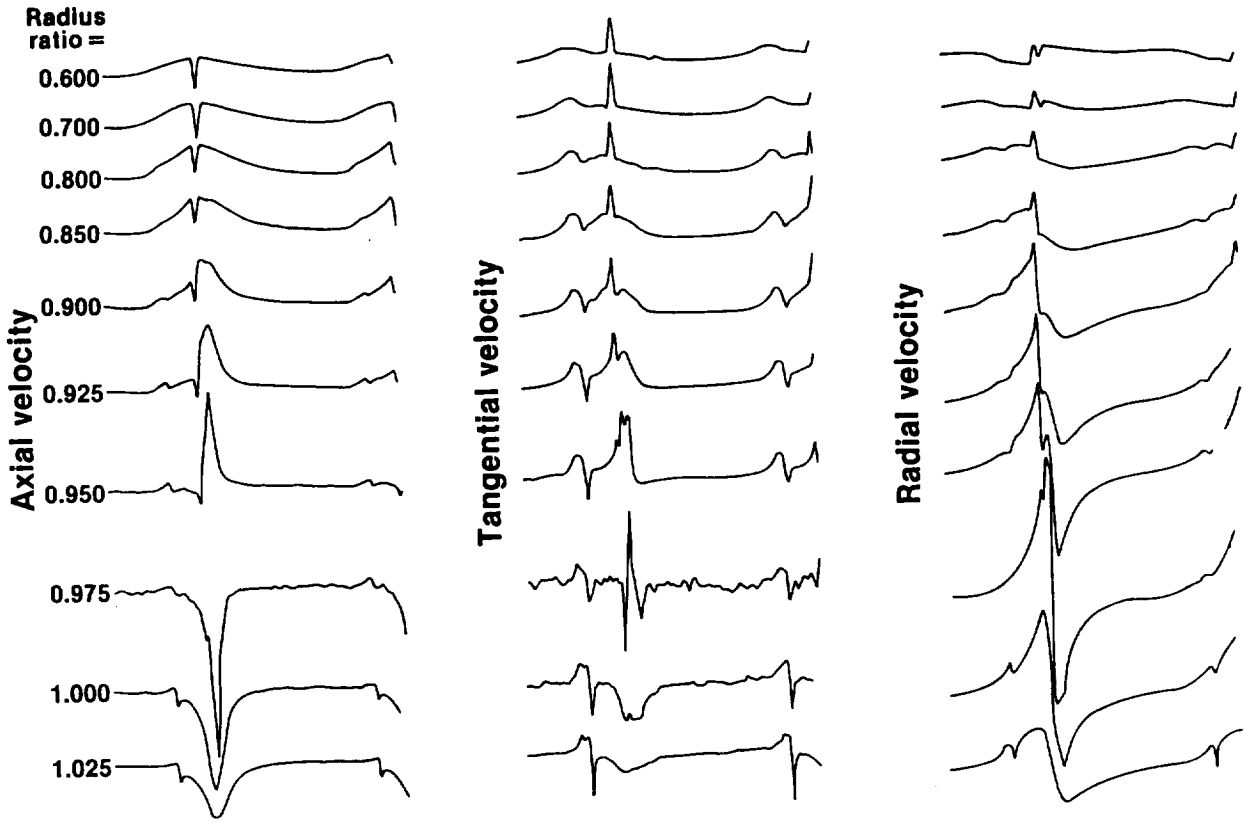

Figure 29 Composite of all data for 2 blade SR-3 in UTRC tunnel

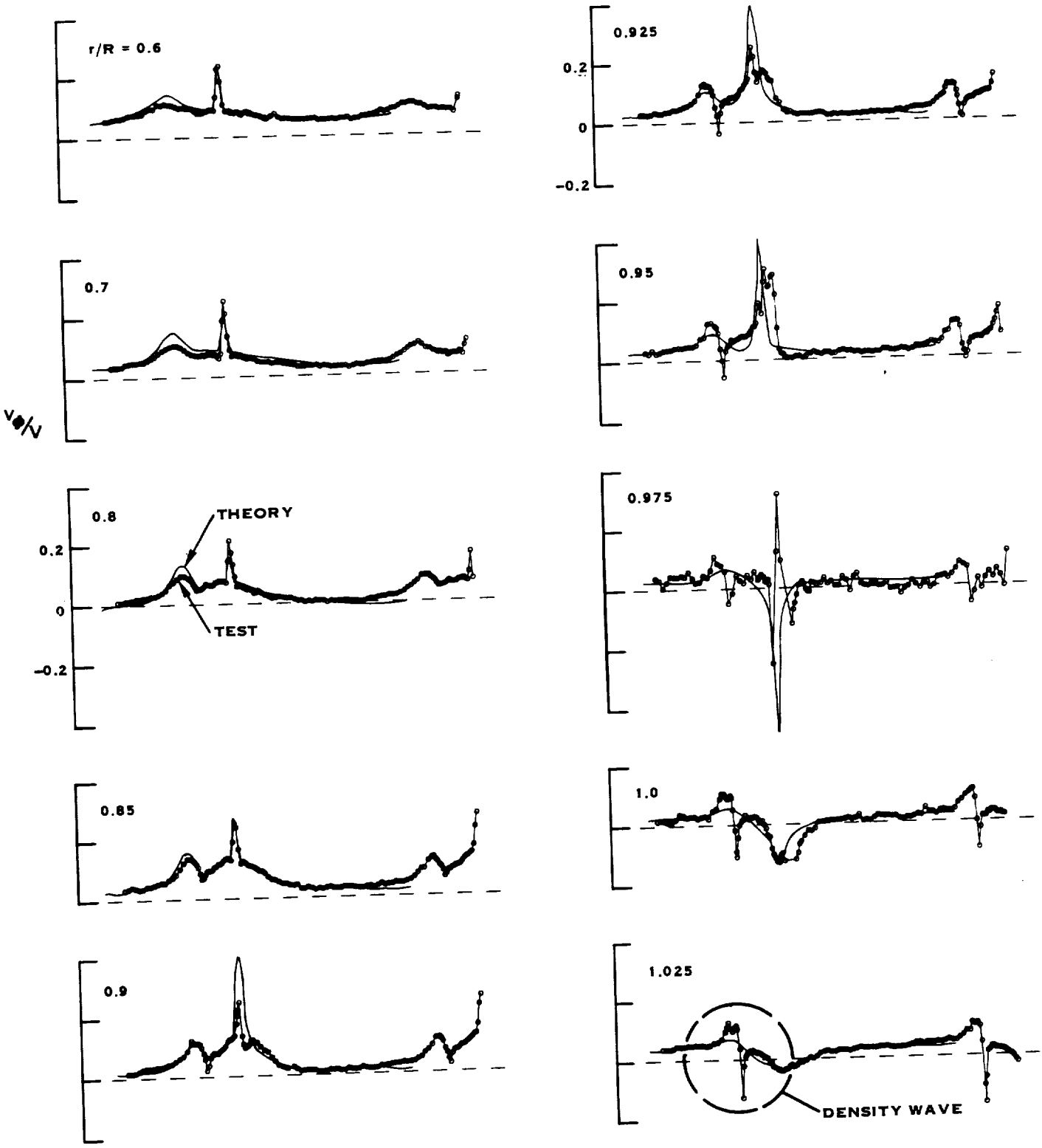

Figure 30 Tangential velocity component in wake of 2 blade SR-3 -test and theory

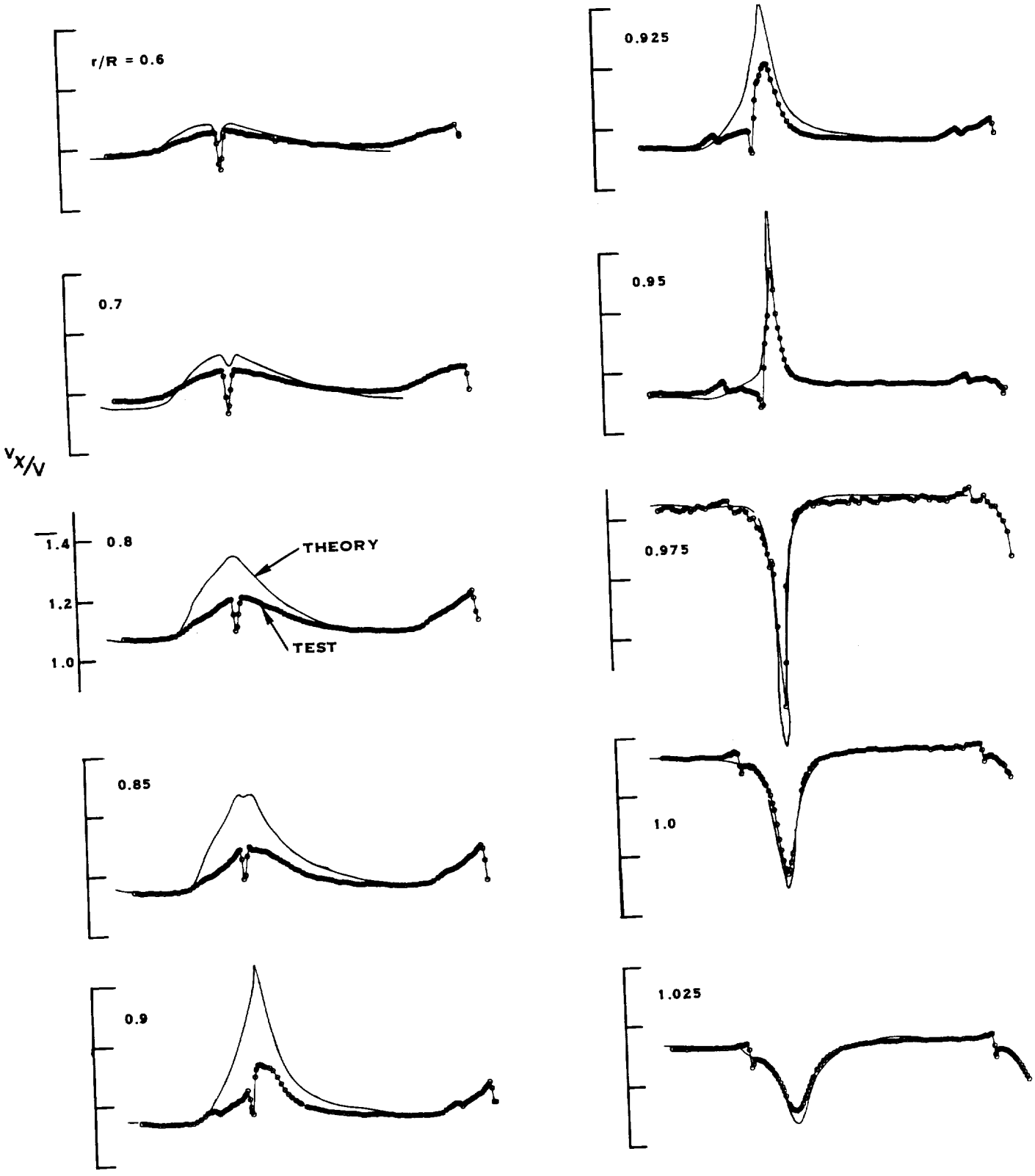

Figure 31 Axial velocity component in wake of 2 blade SR-3 -test and theory

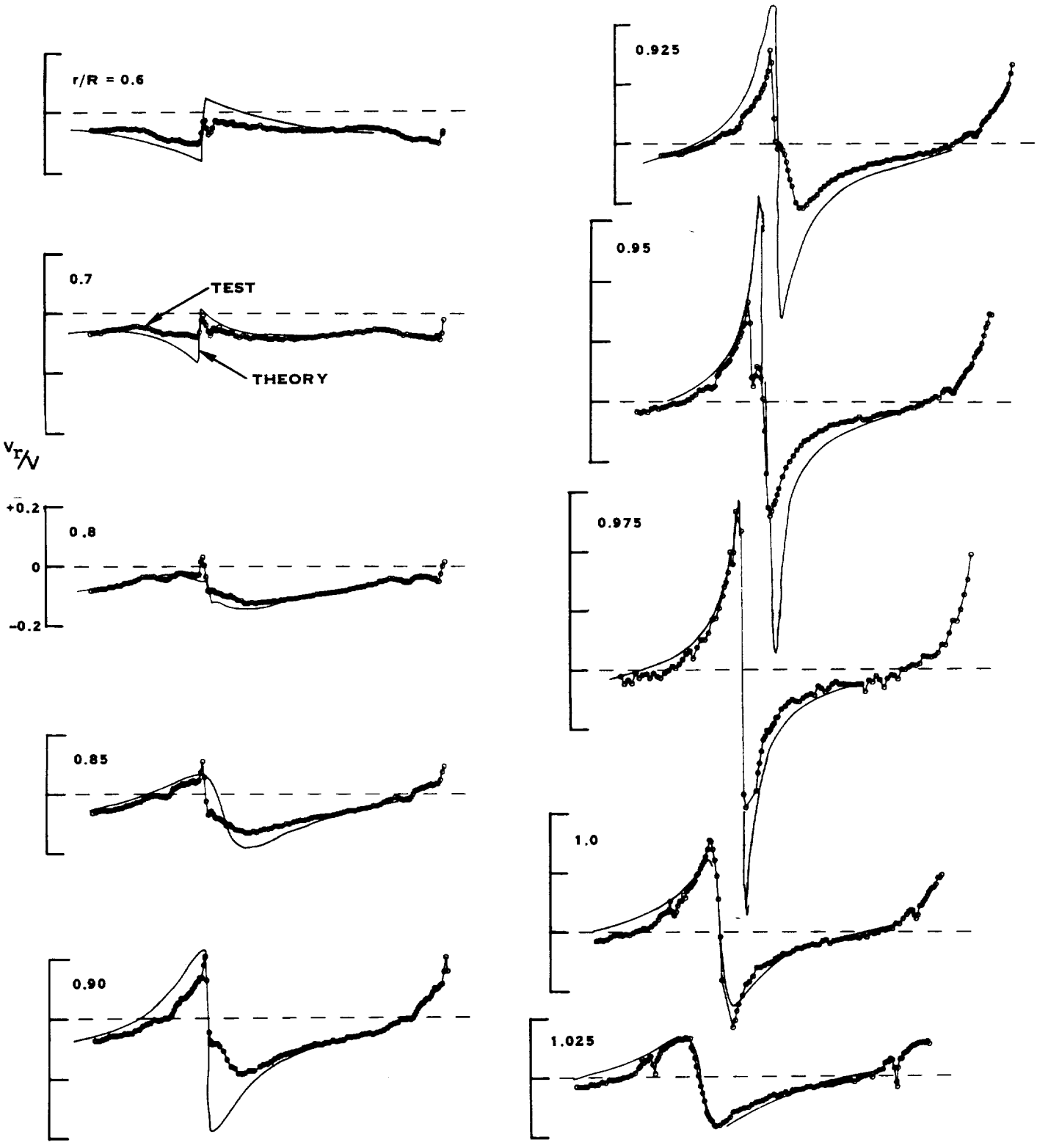

Figure 32 Radial velocity component in wake of 2 blade SR-3 - test and theory

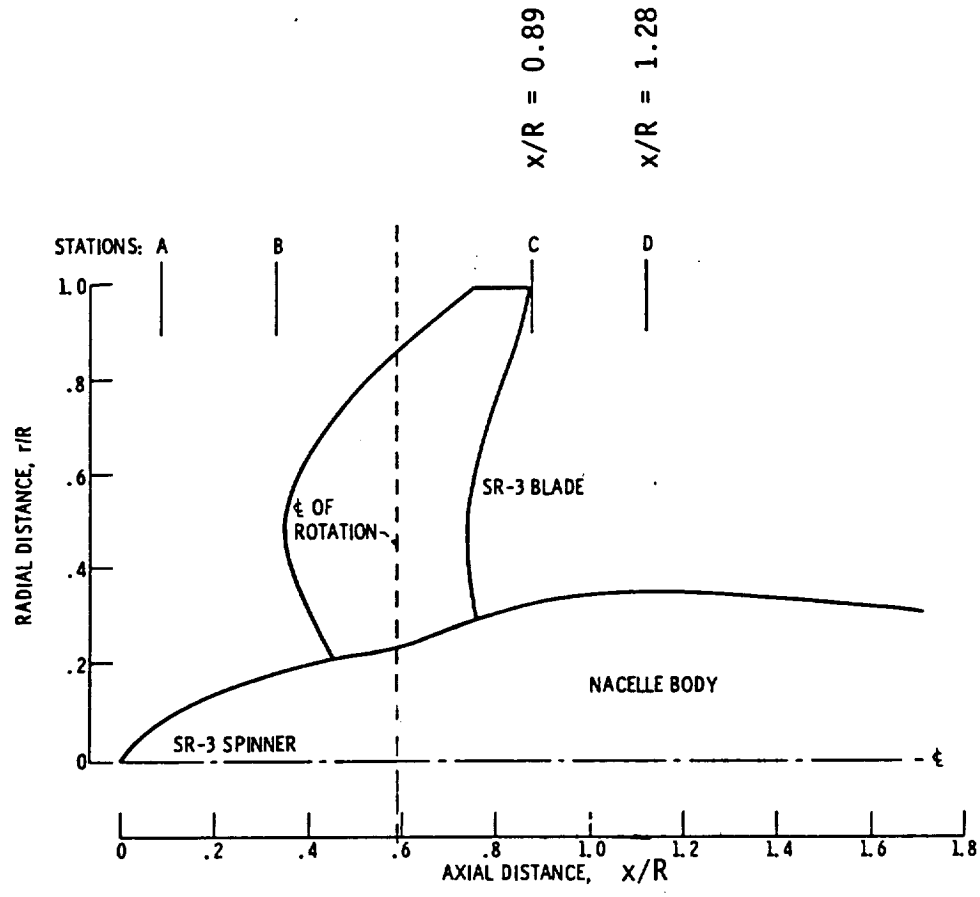

Figure 33 Traversing planes for laser velocimeter measurements of SR-3 wakes in NASA 6'x8' wind tunnel

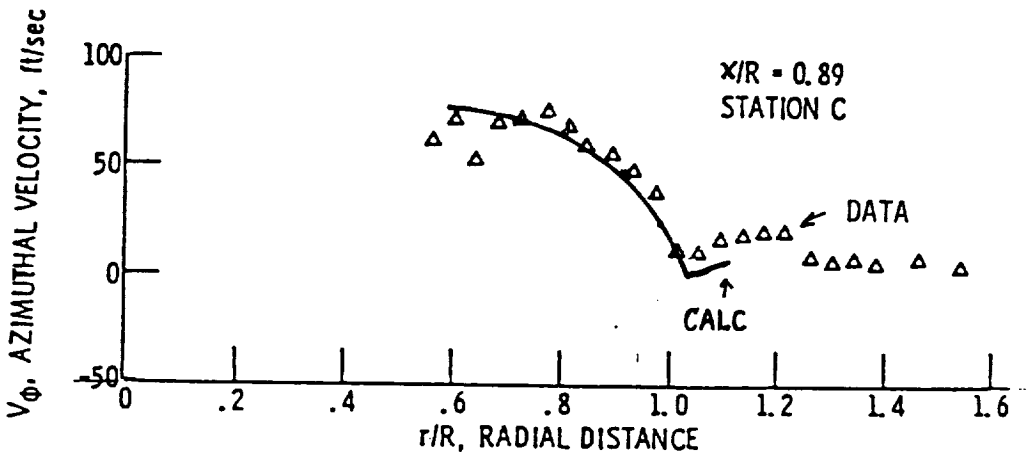

Figure 34 Circumferentially averaged tangential velocity for SR-3 as a function of r/R

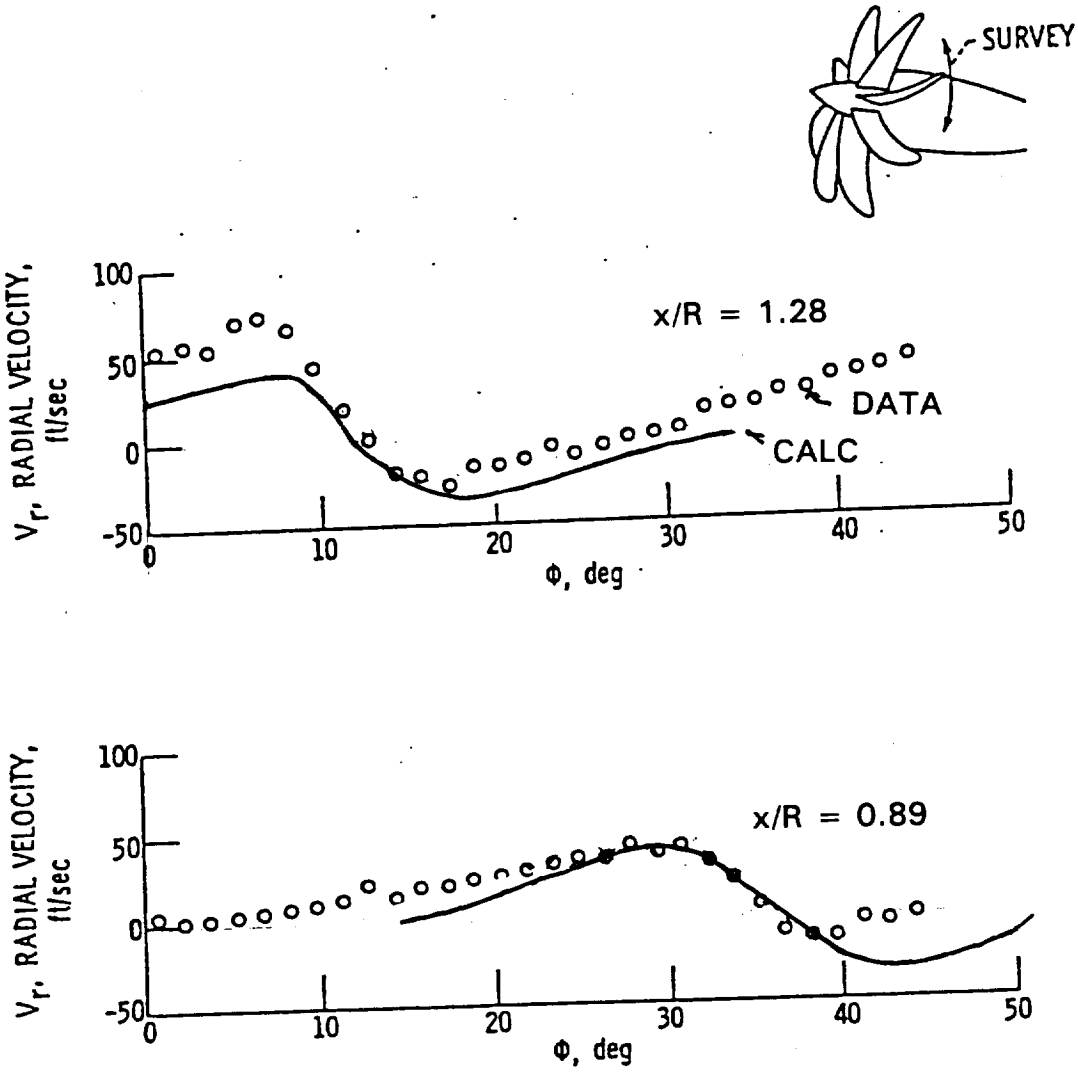

Figure 35 Intrablade variation of radial velocity for SR-3 measured outside the blade tips. r/R = 1.08.

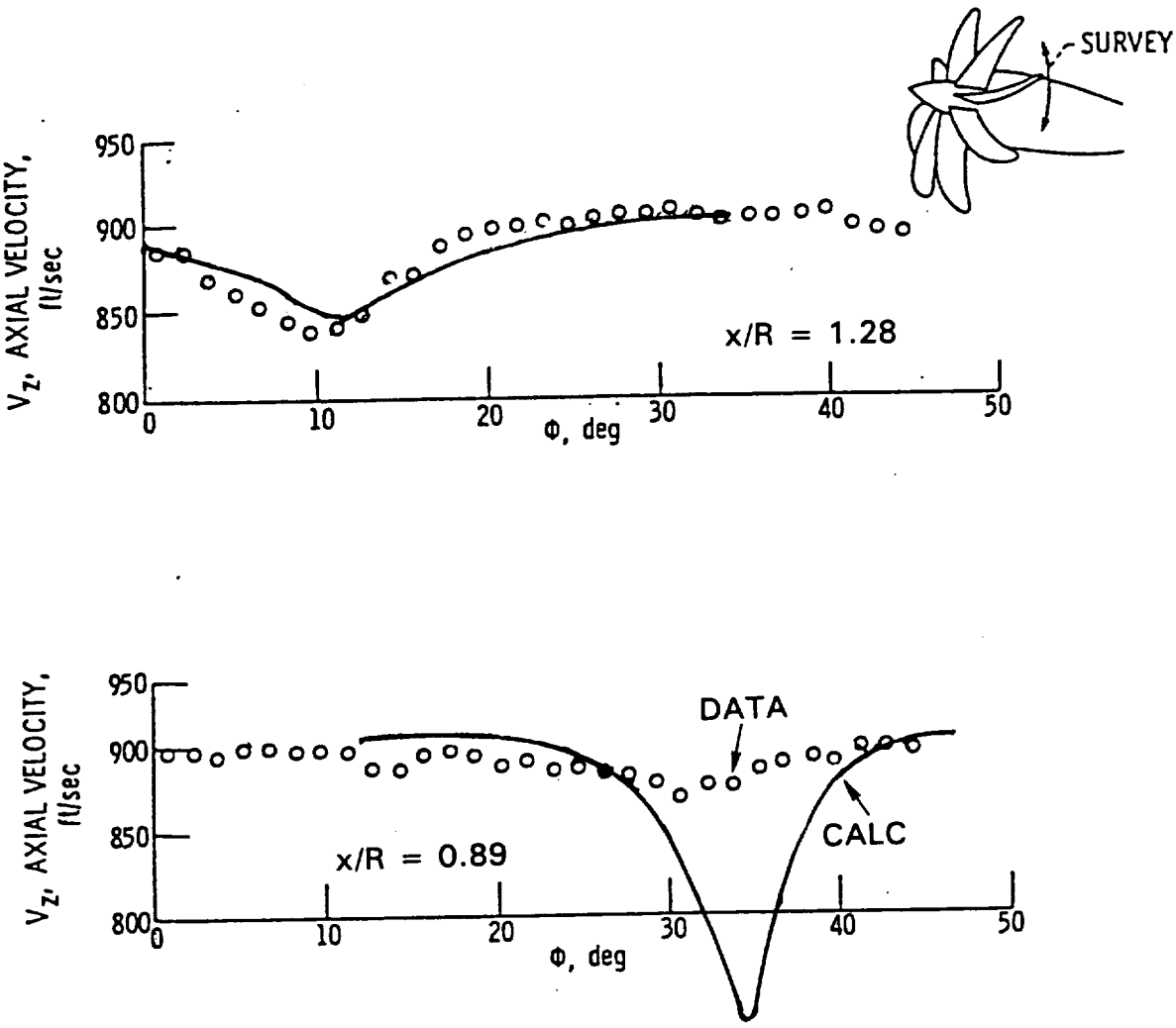

Figure 36 Intrablade variation of axial velocity for SR-3 outside the blade tips. 2 axial stations at r/R=1.08.

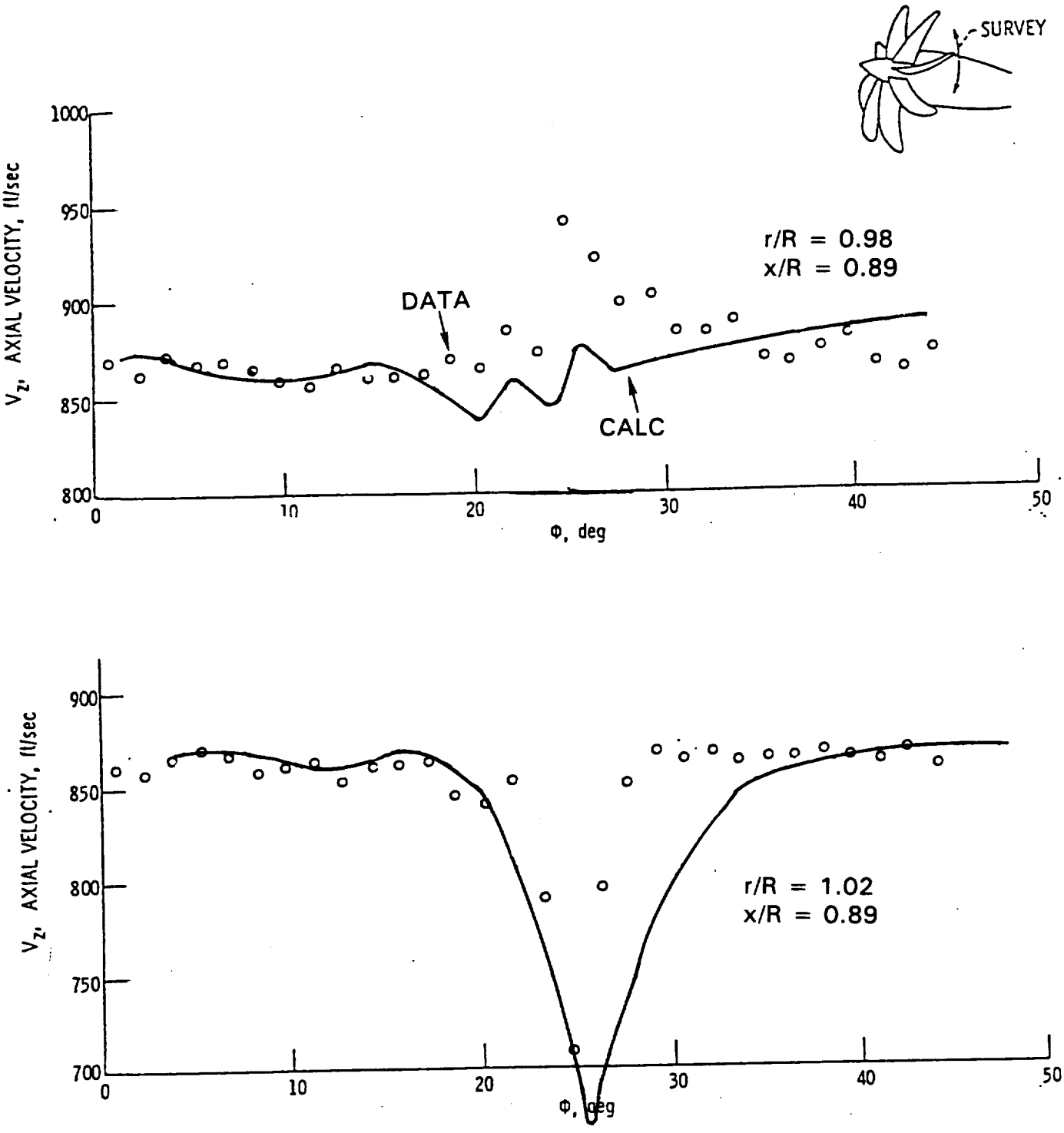

Figure 37 Intrablade variation of axial velocity for SR-3 near tip trailing edge. Inside and outside the tip vortex.

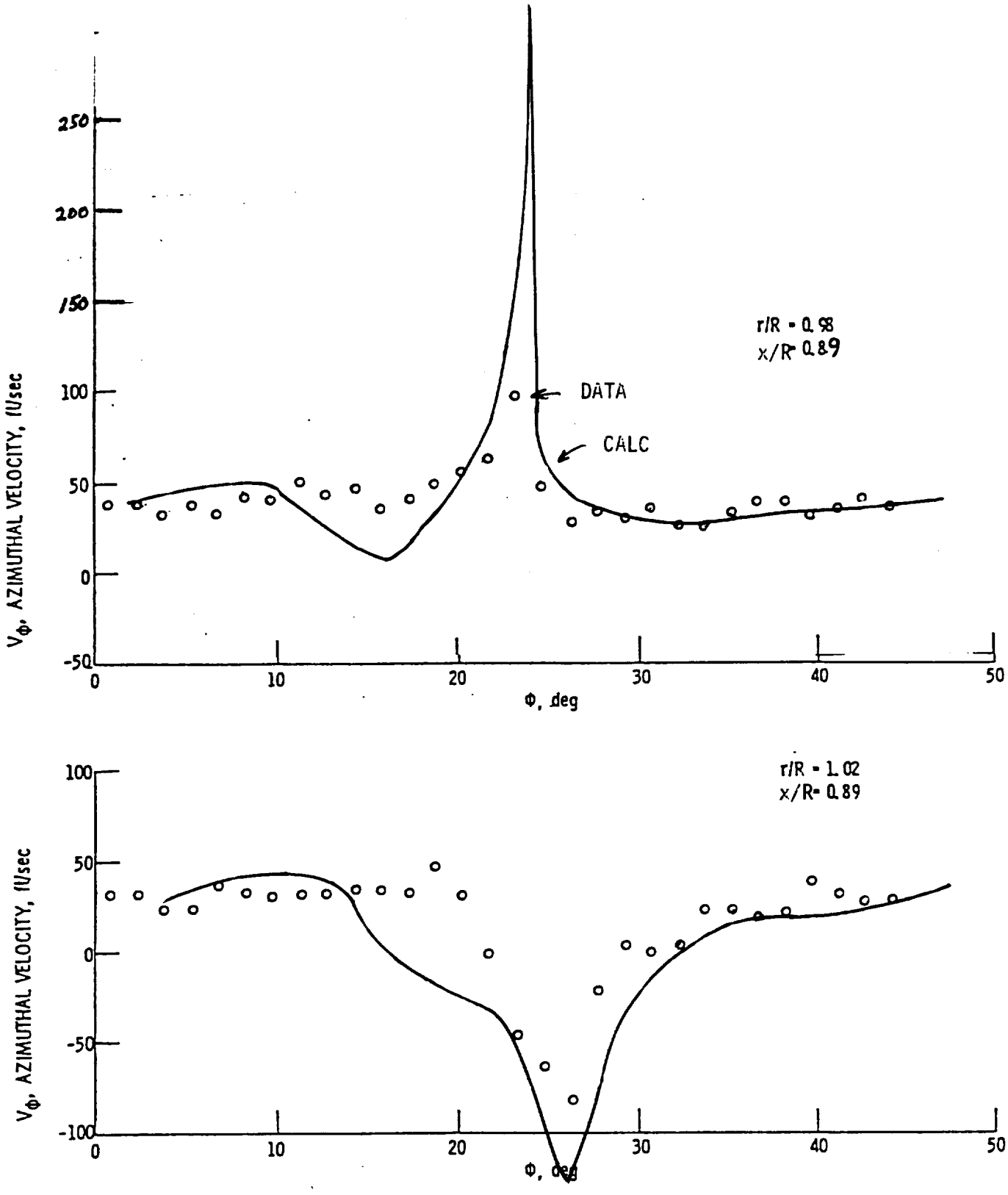

Figure 38 Intrablade variation of tangential velocity for SR-3 near tip trailing edge. Inside and outside the tip vortex.

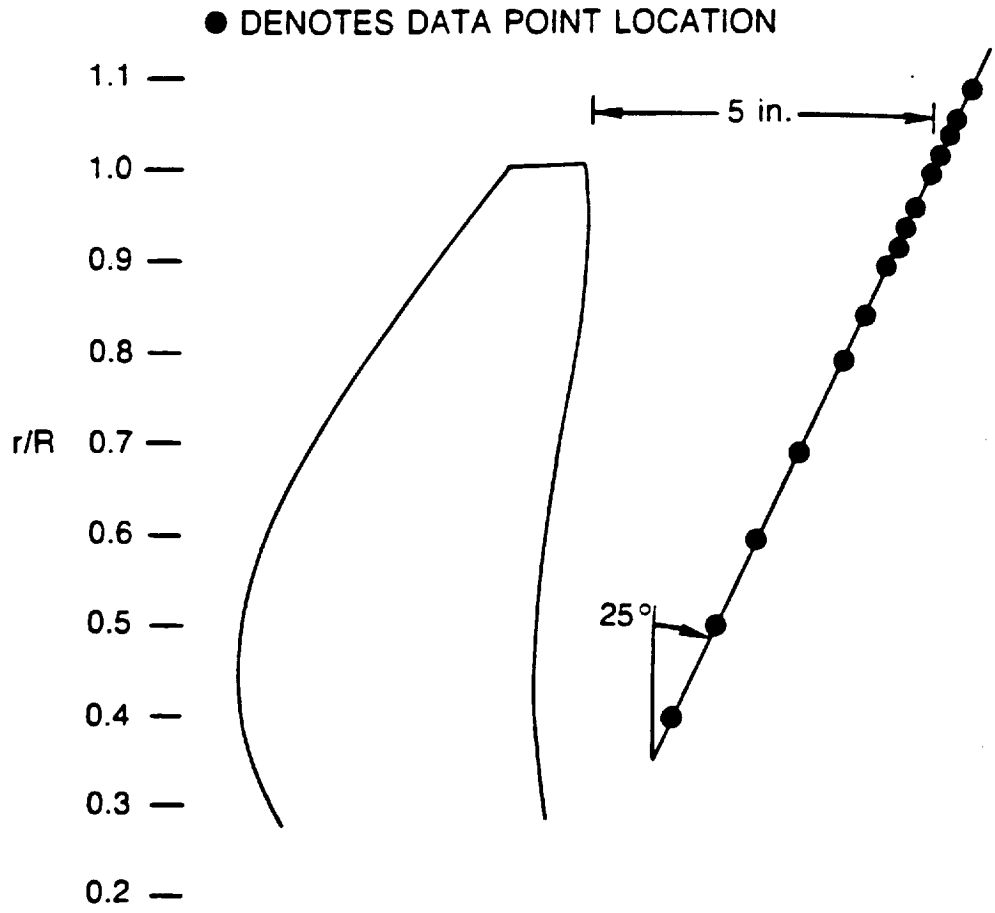

Figure 39 Probe positions for wake survey of CRP-X1.

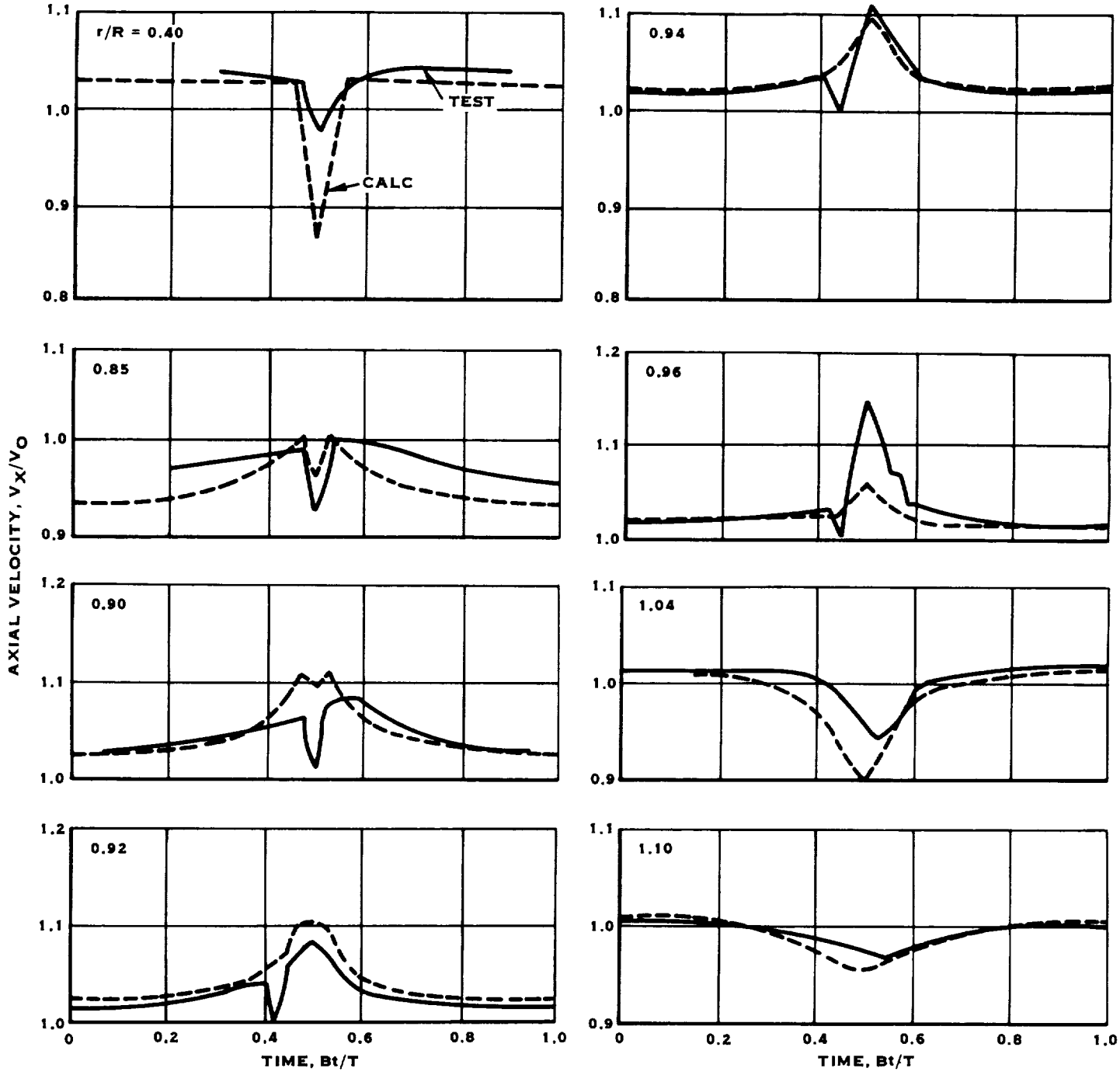

Figure 40 Axial velocity component in wake of single rotor from CRP-X1 Prop-Fan.

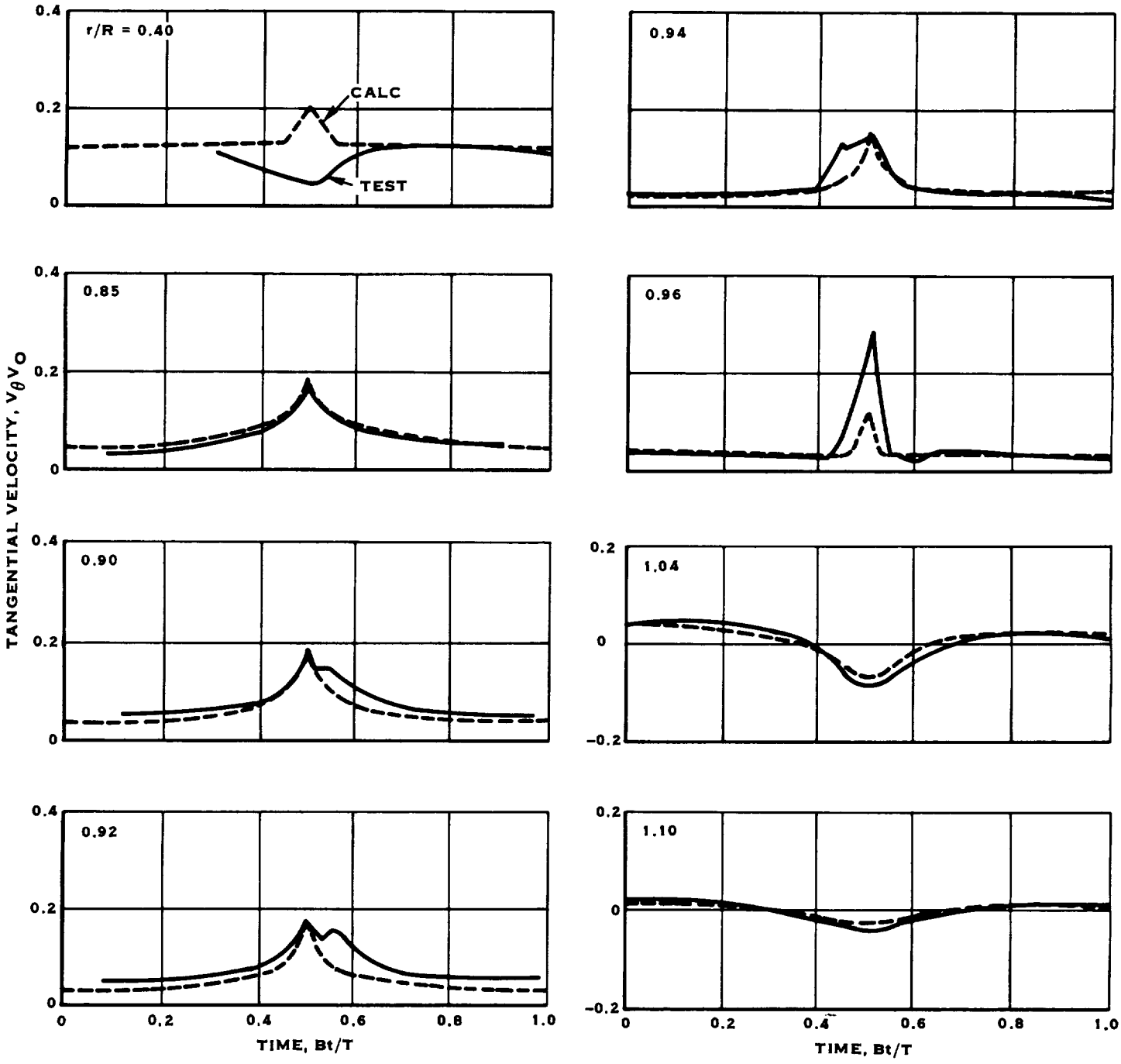

Figure 41 Tangential velocity component in wake of single rotor from CRP-X1 Prop-Fan.

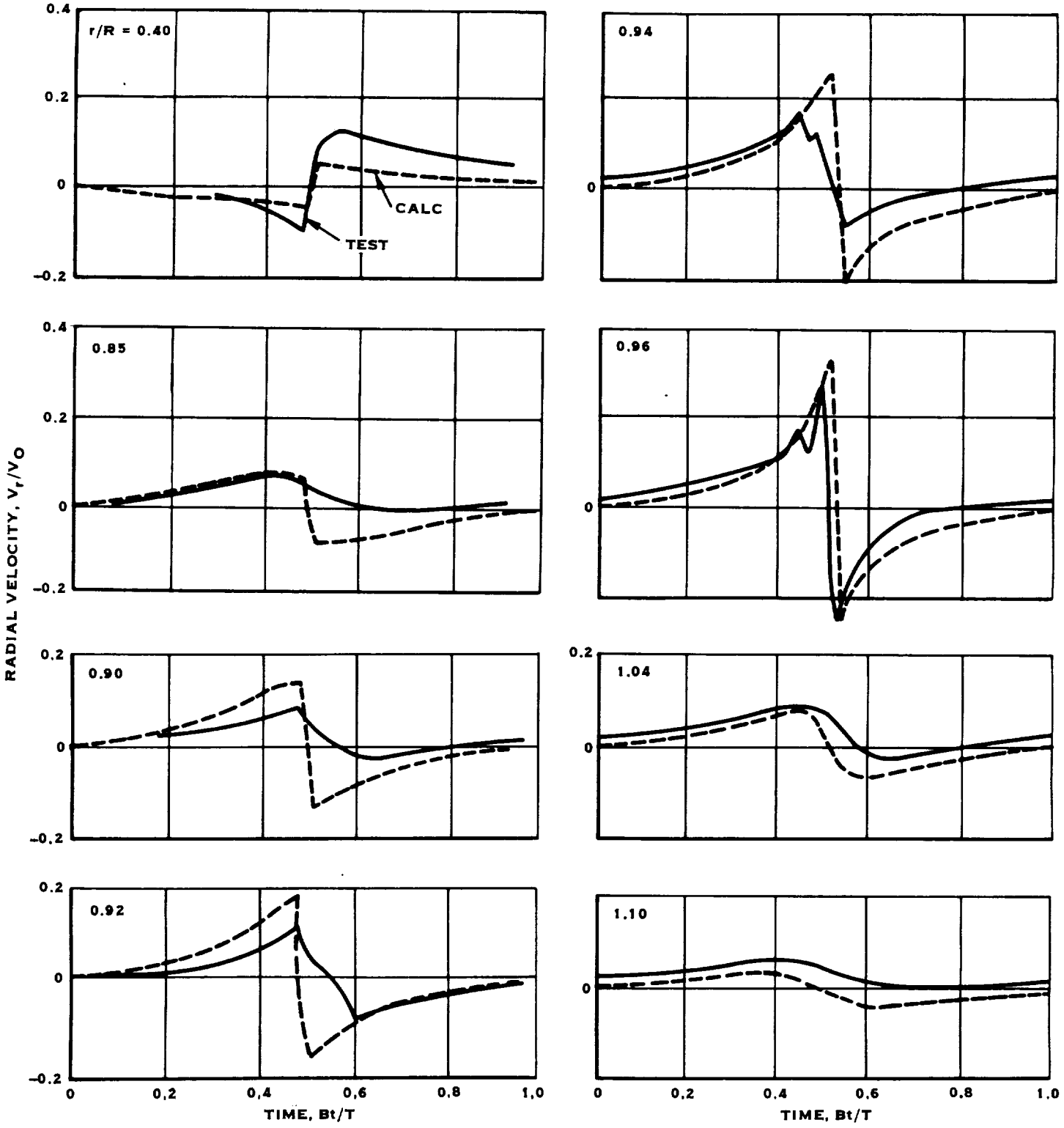

Figure 42 Radial velocity component in wake of single rotor from CRP-X1 Prop-Fan.

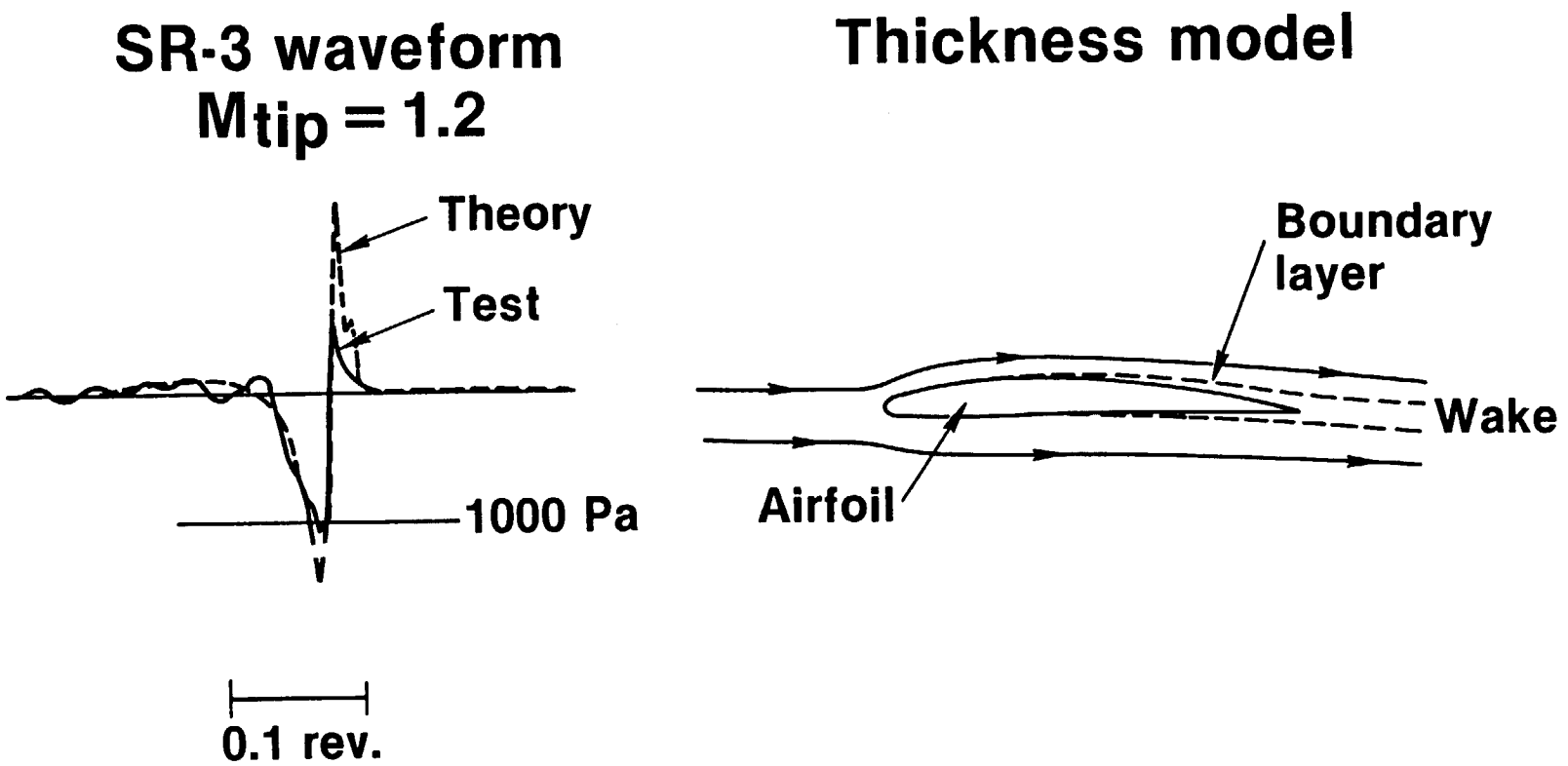

Figure 43 Comparison of measured and predicted acoustic waveforms showing the effect of boundary layer and wake displacement thickness.

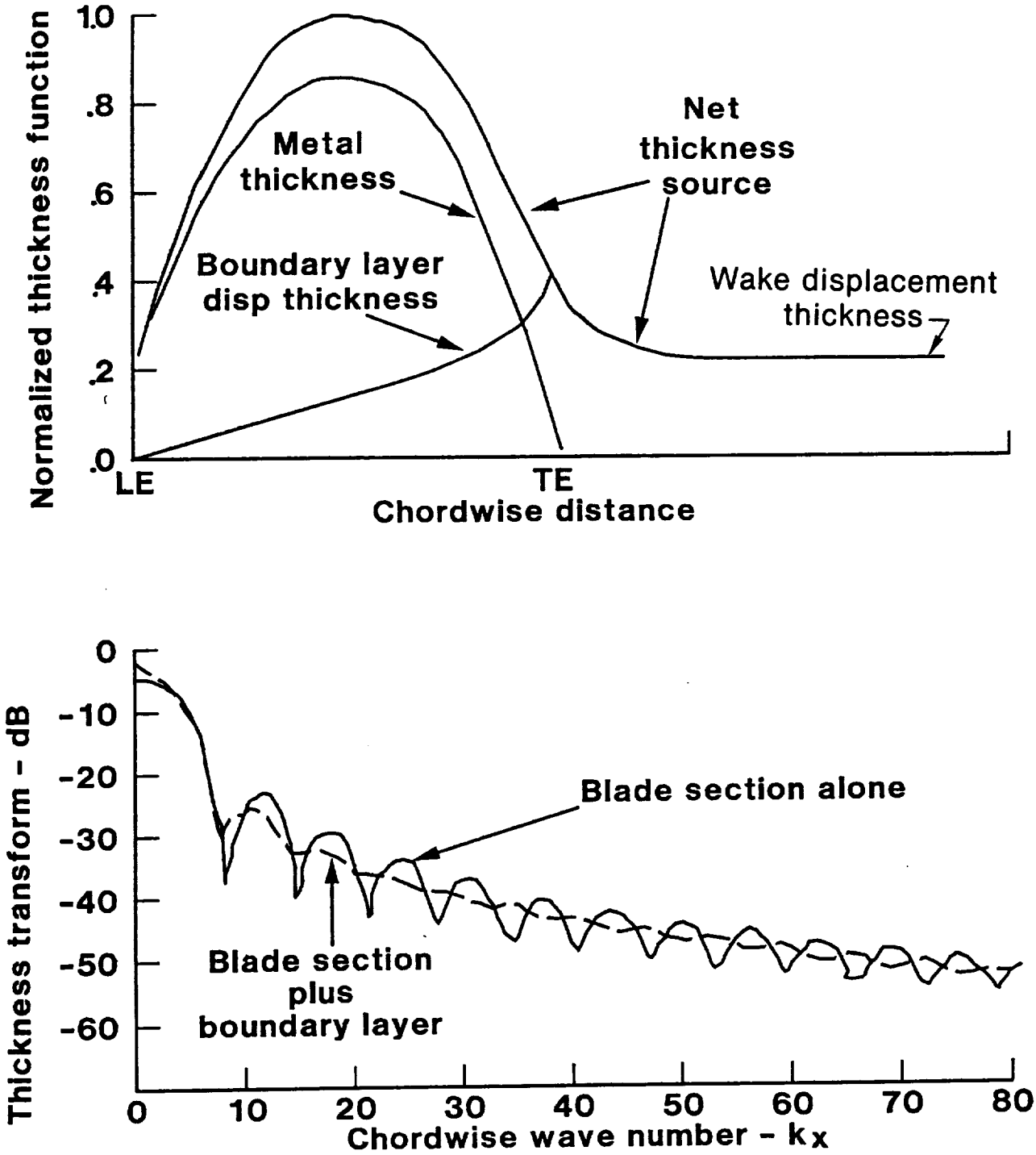

Figure 44 (Top) Comparison of thickness profile for Series 16 airfoil with and without displacement thickness. Maximum thickness normalized to 1.0. Airfoil thickness ratio is 0.02, assumed drag coefficient is 0.012, and total maximum thickness ratio is 0.0233.
(Bottom) Fourier transform of displacement profiles above.

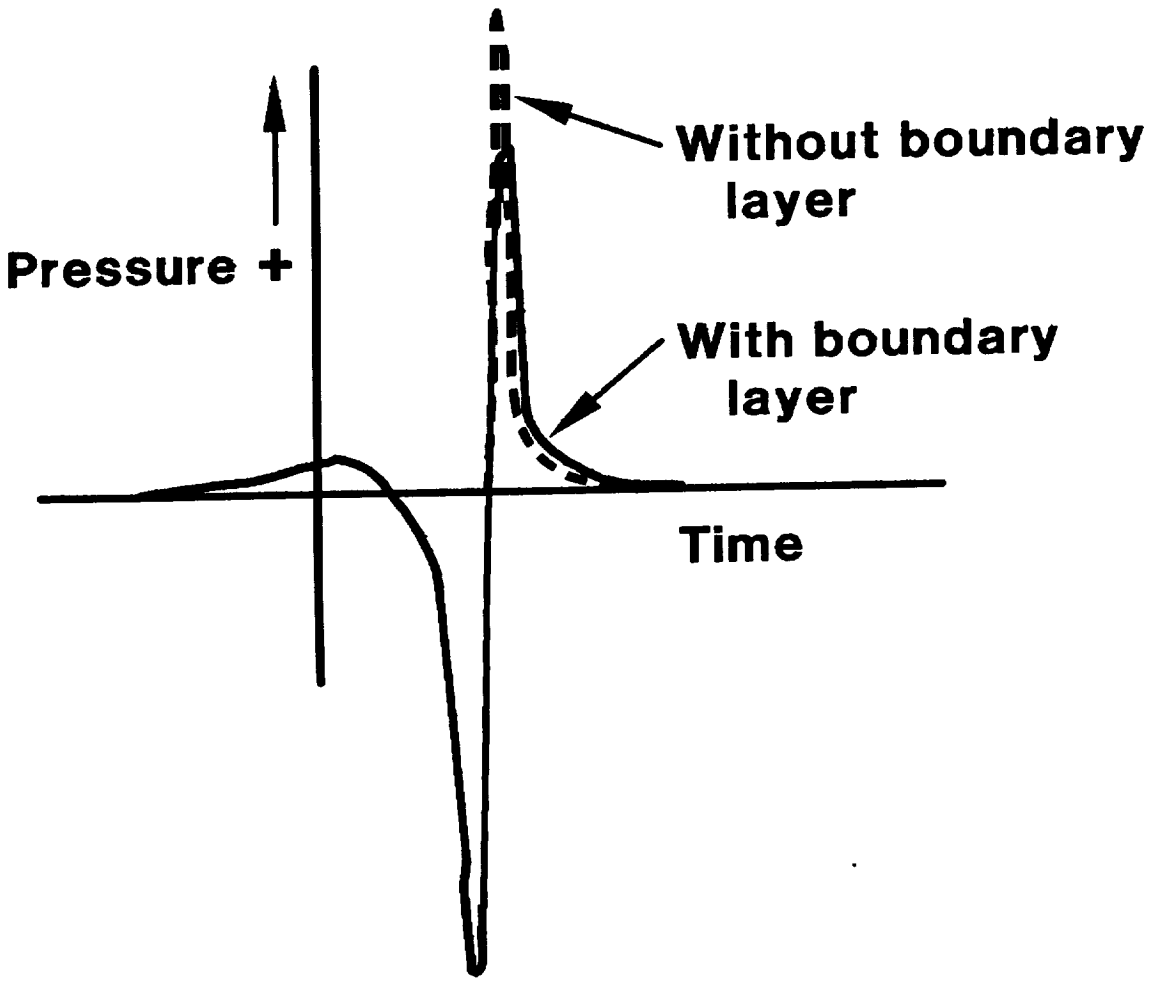

Figure 45 Effect of displacement thickness on predicted acoustic waveform. (Note: these predictions are for SR7 as opposed to SR3 in Figure 43.)

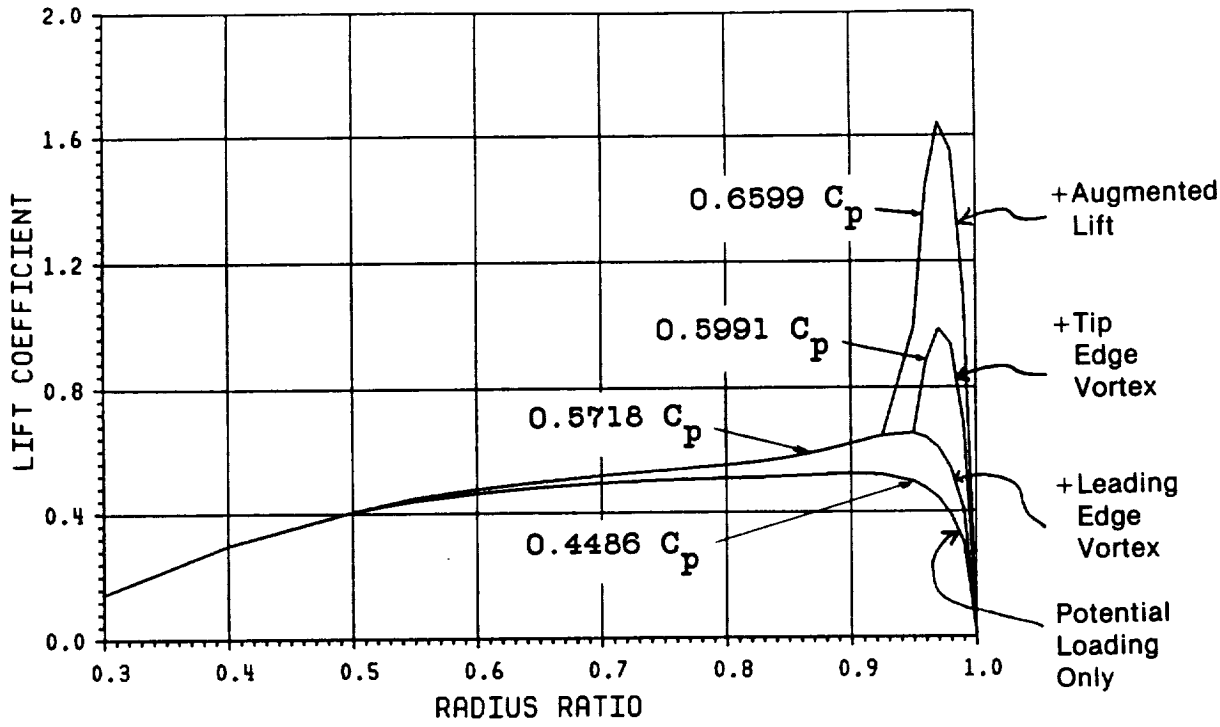

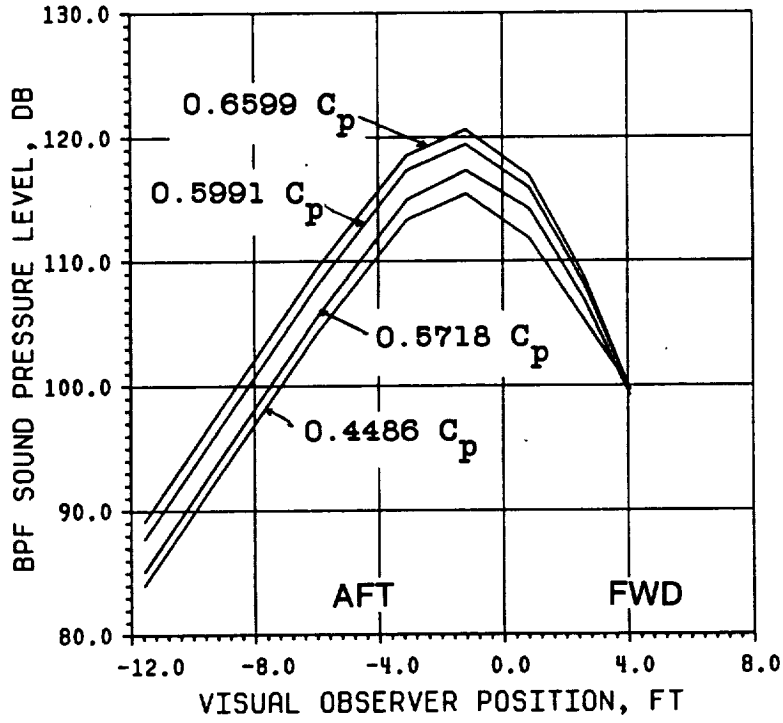

Figure 46 Contributions of individual vortex loading components to spanwise loading distribution and sideline noise. Observer sideline distance equal to 6.12 ft (3 diameters).

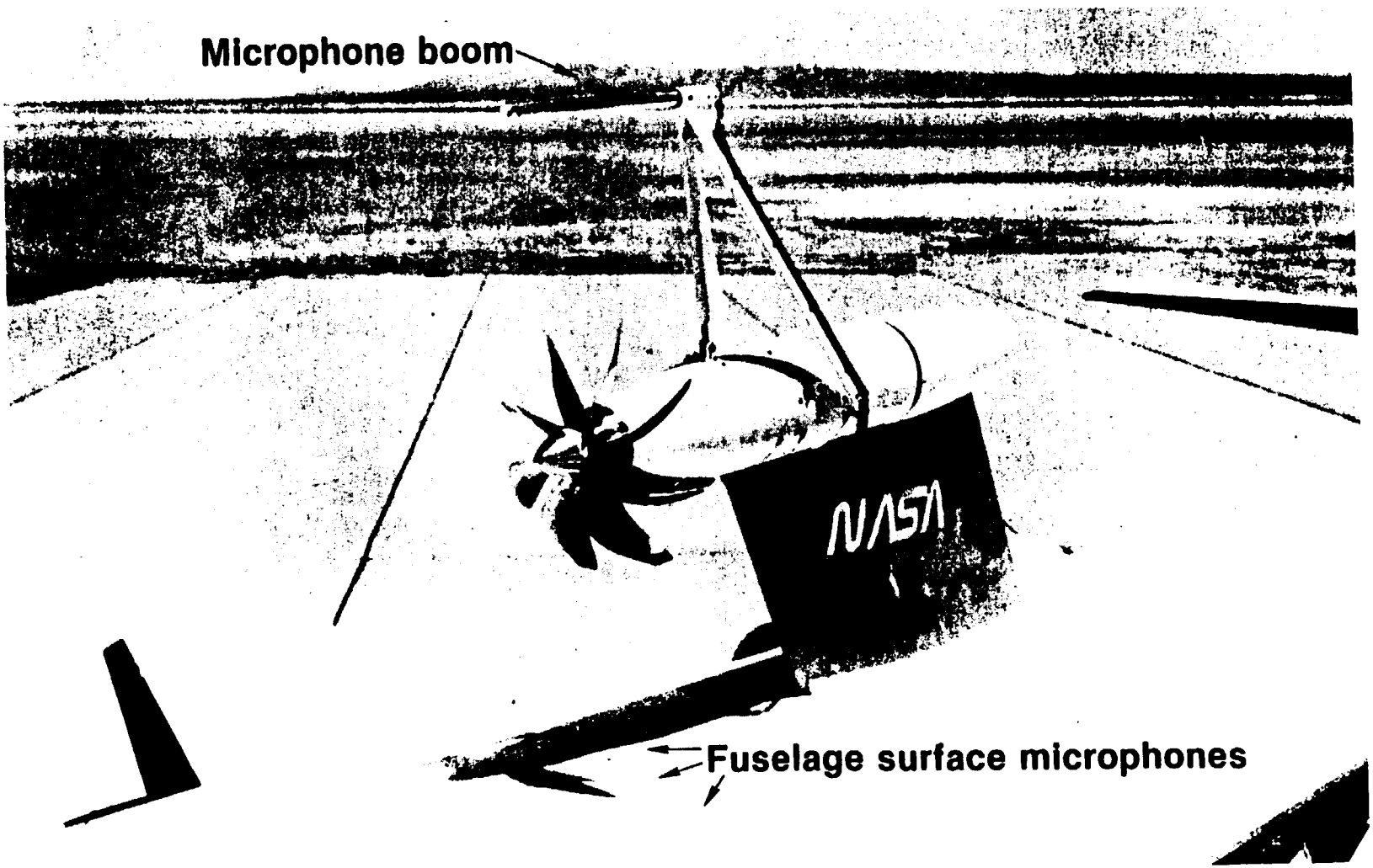

Figure 47 Photograph of the SR-3 Prop-Fan, microphone boom and fuselage surface microphones on JetStar test aircraft (taken from Ref. 21).

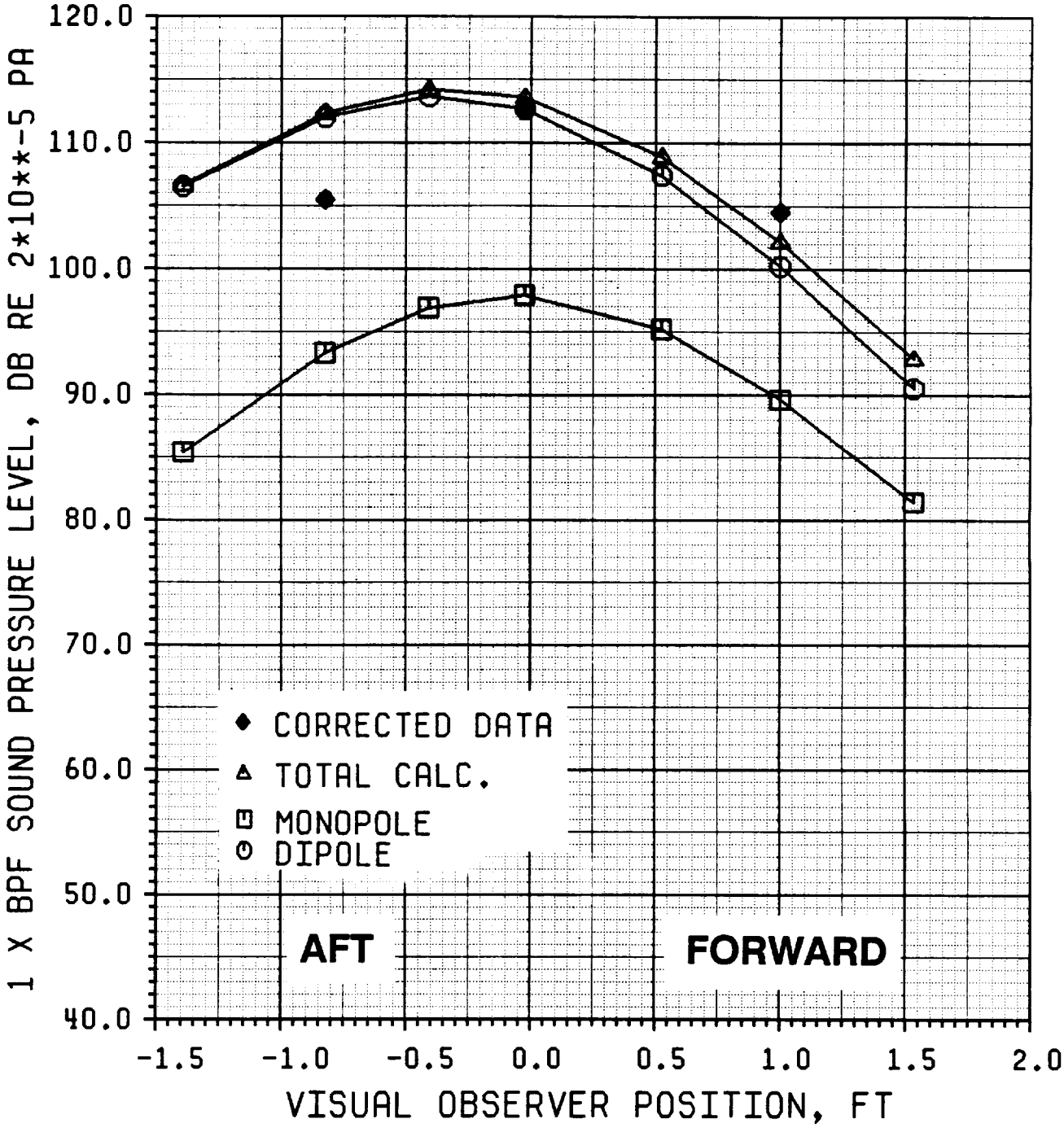

Figure 48 Comparison of measured and predicted directivity of BPF tone at 0.8 diameter sideline. SR-3 model at 20000 ft. altitude, 0.51 flight Mach number, 2.92 advance ratio, and 1.89 CP. Noise predicted with tip vortex loading normal to blade surface (default procedure).

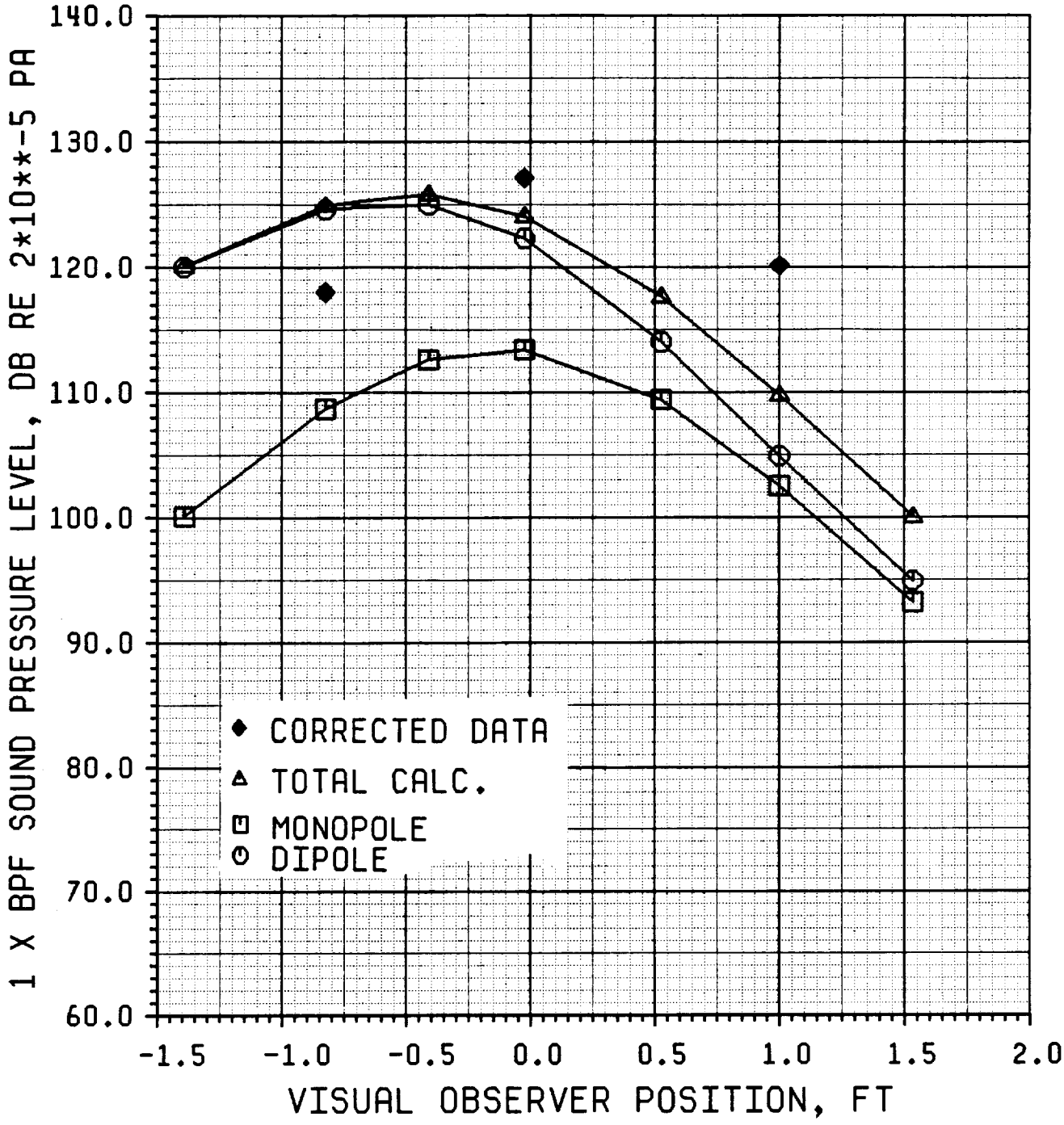

Figure 49 Comparison of measured and predicted directivity of BPF tone at 0.8 diameter sideline. SR-3 model at 30000 ft. altitude, 0.62 flight Mach number, 2.96 advance ratio, and 1.95 CP. Noise predicted with tip vortex loading normal to blade surface (default procedure).

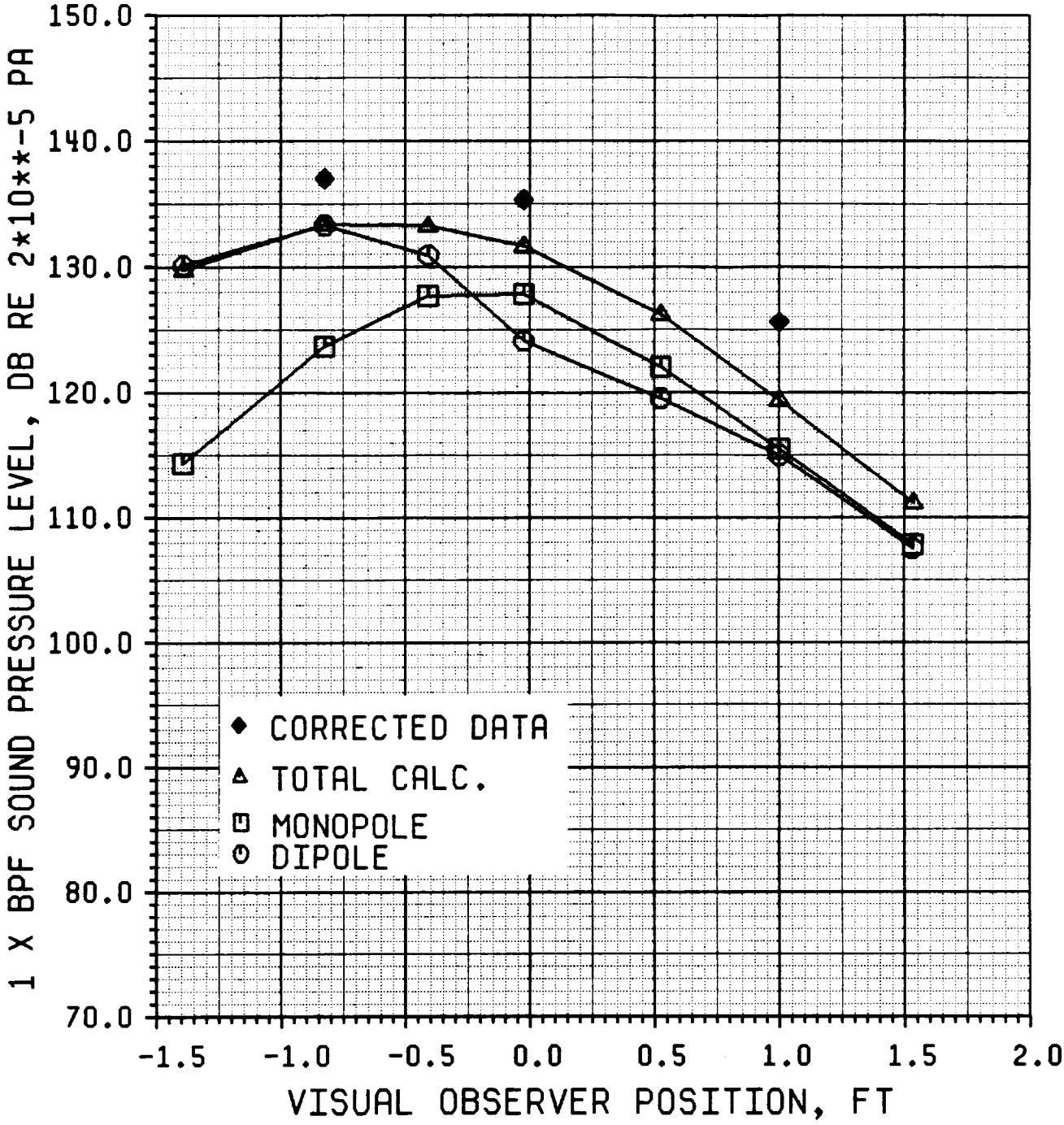

Figure 50 Comparison of measured and predicted directivity of BPF tone at 0.8 diameter sideline. SR-3 model at 30000 ft. altitude, 0.71 flight Mach number, 3.06 advance ratio, and 1.84 CP. Noise predicted with tip vortex loading normal to blade surface (default procedure).

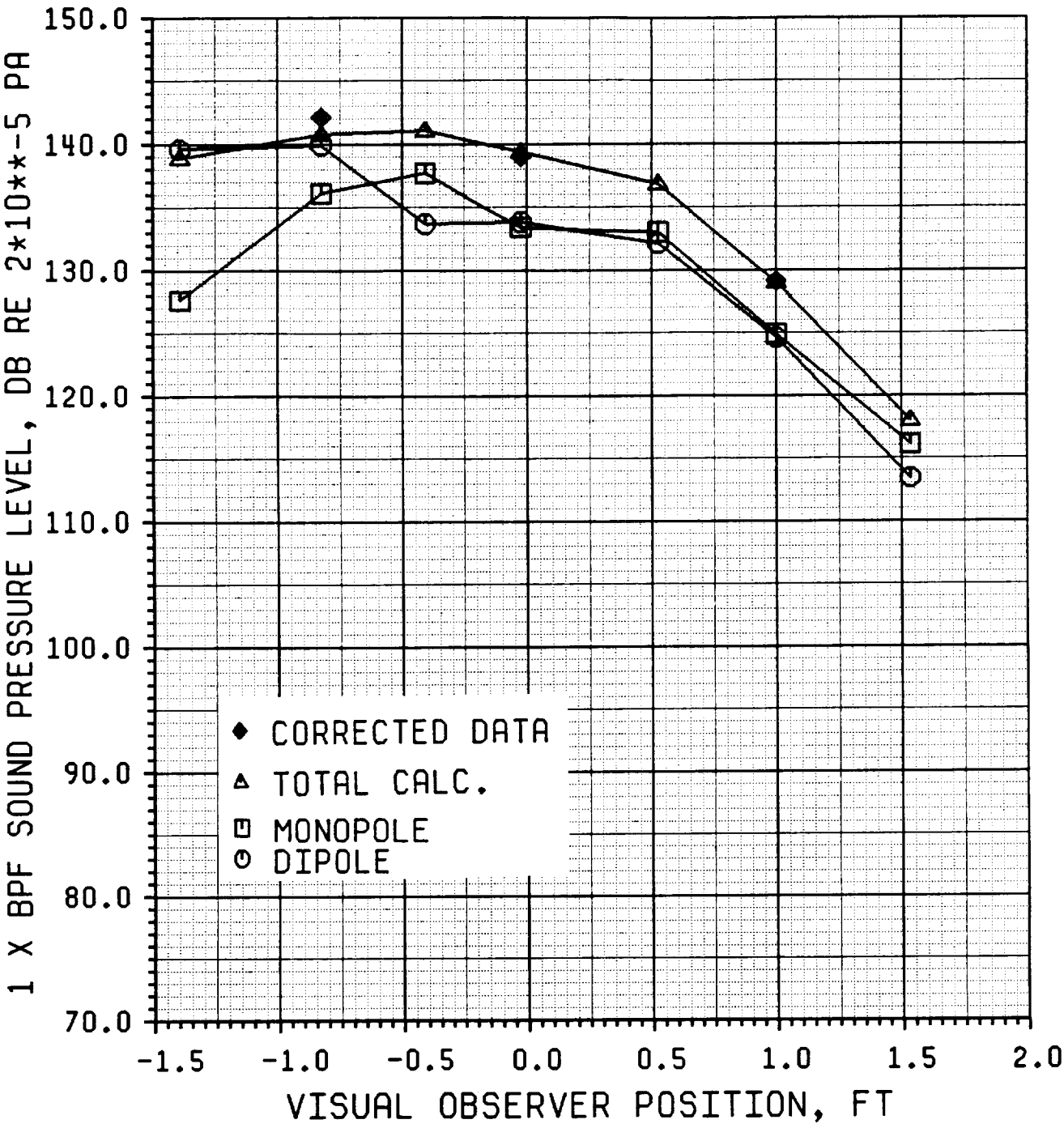

Figure 51 Comparison of measured and predicted directivity of BPF tone at 0.8 diameter sideline. SR-3 model at 30000 ft. altitude, 0.79 flight Mach number, 3.03 advance ratio, and 1.83 CP. Noise predicted with tip vortex loading normal to blade surface (default procedure).

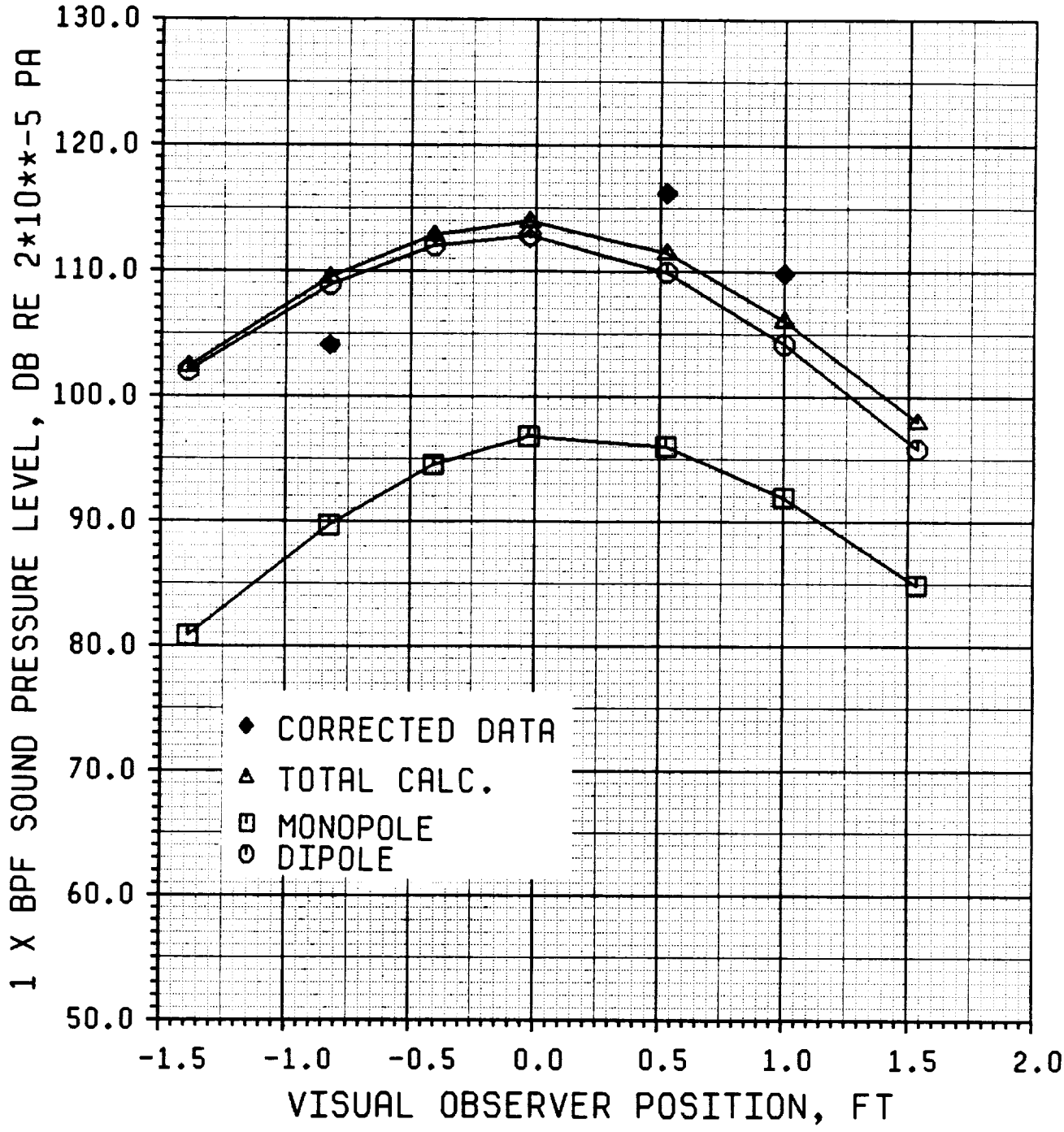

Figure 52 Comparison of measured and predicted directivity of BPF tone at 0.8 diameter sideline. SR-2 model at 20000 ft. altitude, 0.52 flight Mach number, 3.18 advance ratio, and 2.37 CP. Noise predicted with tip vortex loading normal to blade surface (default procedure).

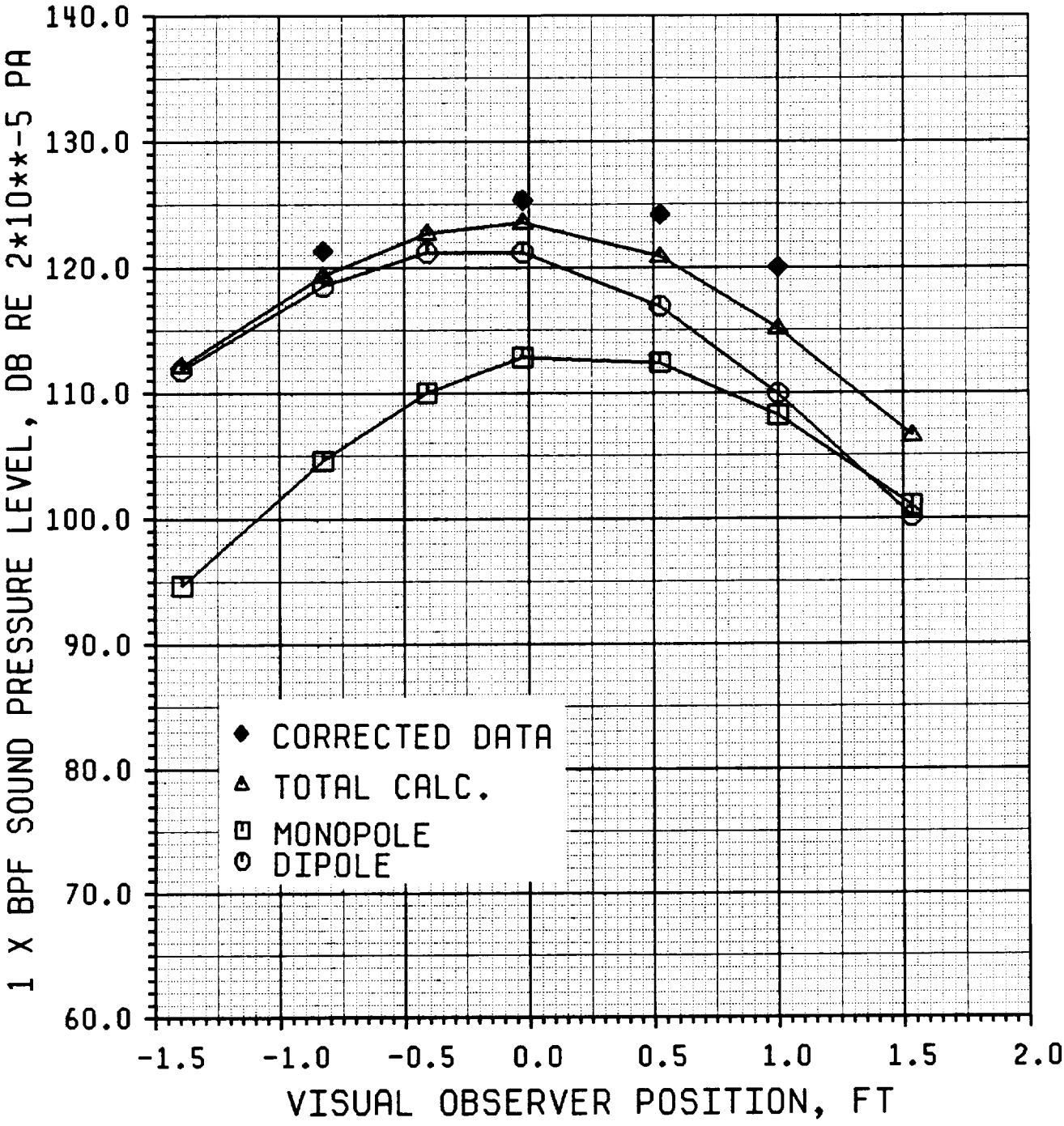

Figure 53 Comparison of measured and predicted directivity of BPF tone at 0.8 diameter sideline. SR-2 model at 30000 ft. altitude, 0.62 flight Mach number, 3.17 advance ratio, and 1.82 CP. Noise predicted with tip vortex loading normal to blade surface (default procedure).

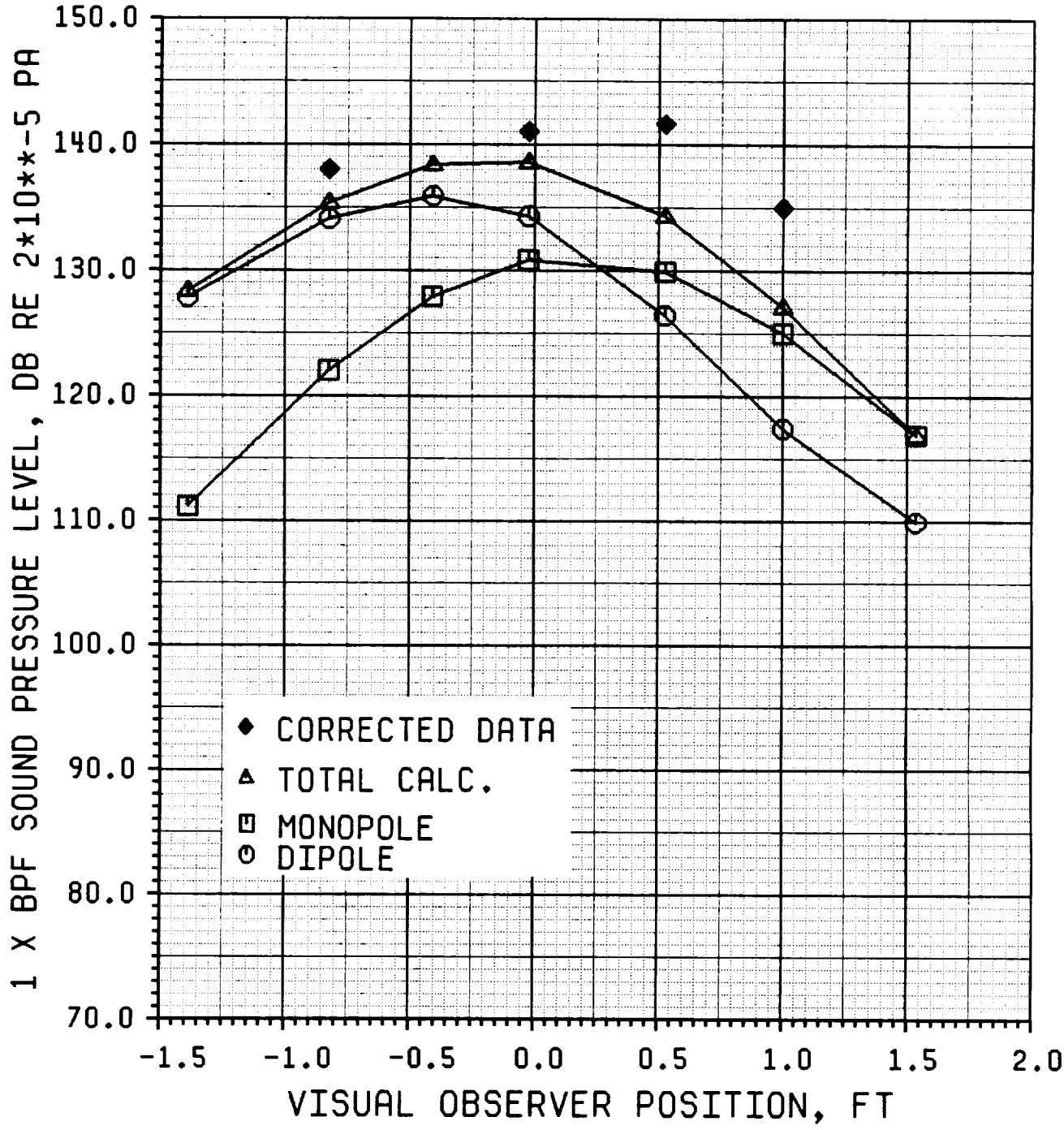

Figure 54 Comparison of measured and predicted directivity of BPF tone at 0.8 diameter sideline. SR-2 model at 30000 ft. altitude, 0.71 flight Mach number, 3.15 advance ratio, and 1.99 CP. Noise predicted with tip vortex loading normal to blade surface (default procedure).

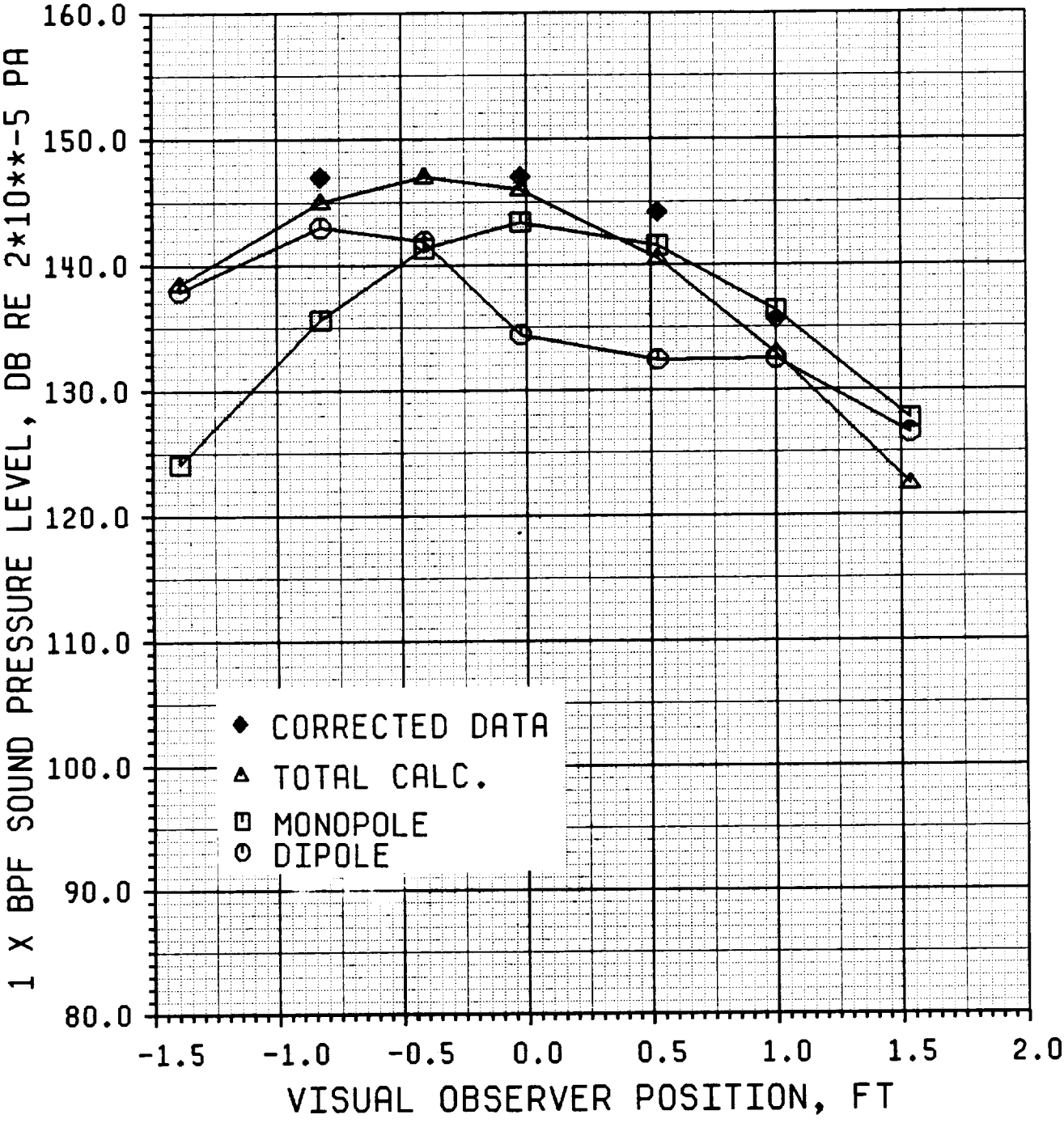

Figure 55 Comparison of measured and predicted directivity of BPF tone at 0.8 diameter sideline. SR-2 model at 30000 ft. altitude, 0.79 flight Mach number, 3.19 advance ratio, and 2.09 CP. Noise predicted with tip vortex loading normal to blade surface (default procedure).

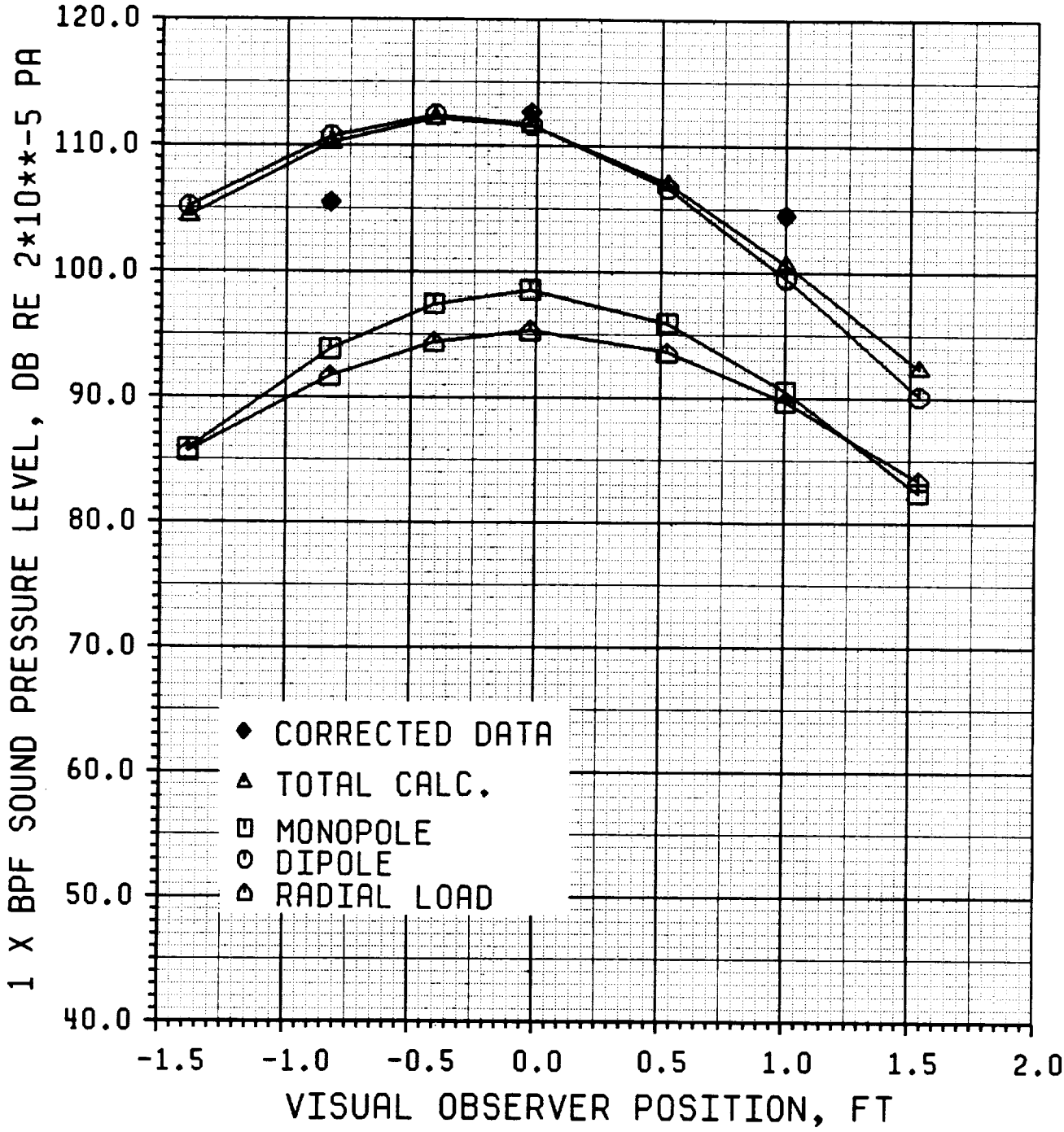

Figure 56 Comparison of measured and predicted directivity of BPF tone at 0.8 diameter sideline. SR-3 model at 20000 ft. altitude, 0.51 flight Mach number, 2.92 advance ratio, and 1.89 CP. Noise predicted with tip force acting in the radial direction. Compare with Figure 48.

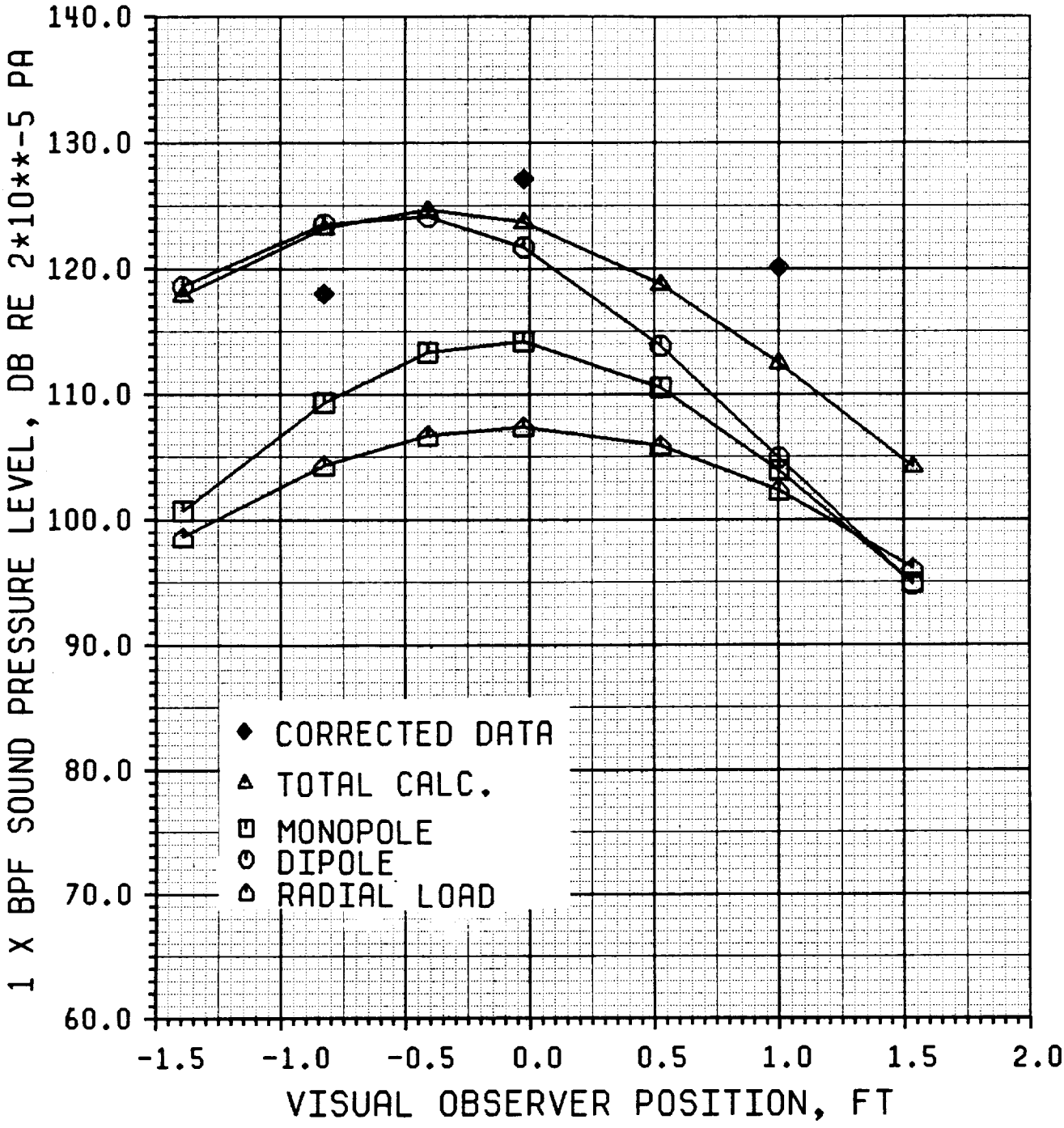

Figure 57 Comparison of measured and predicted directivity of BPF tone at 0.8 diameter sideline. SR-3 model at 30000 ft. altitude, 0.62 flight Mach number, 2.96 advance ratio, and 1.95 CP. Noise predicted with tip force acting in the radial direction. Compare with Figure 49.

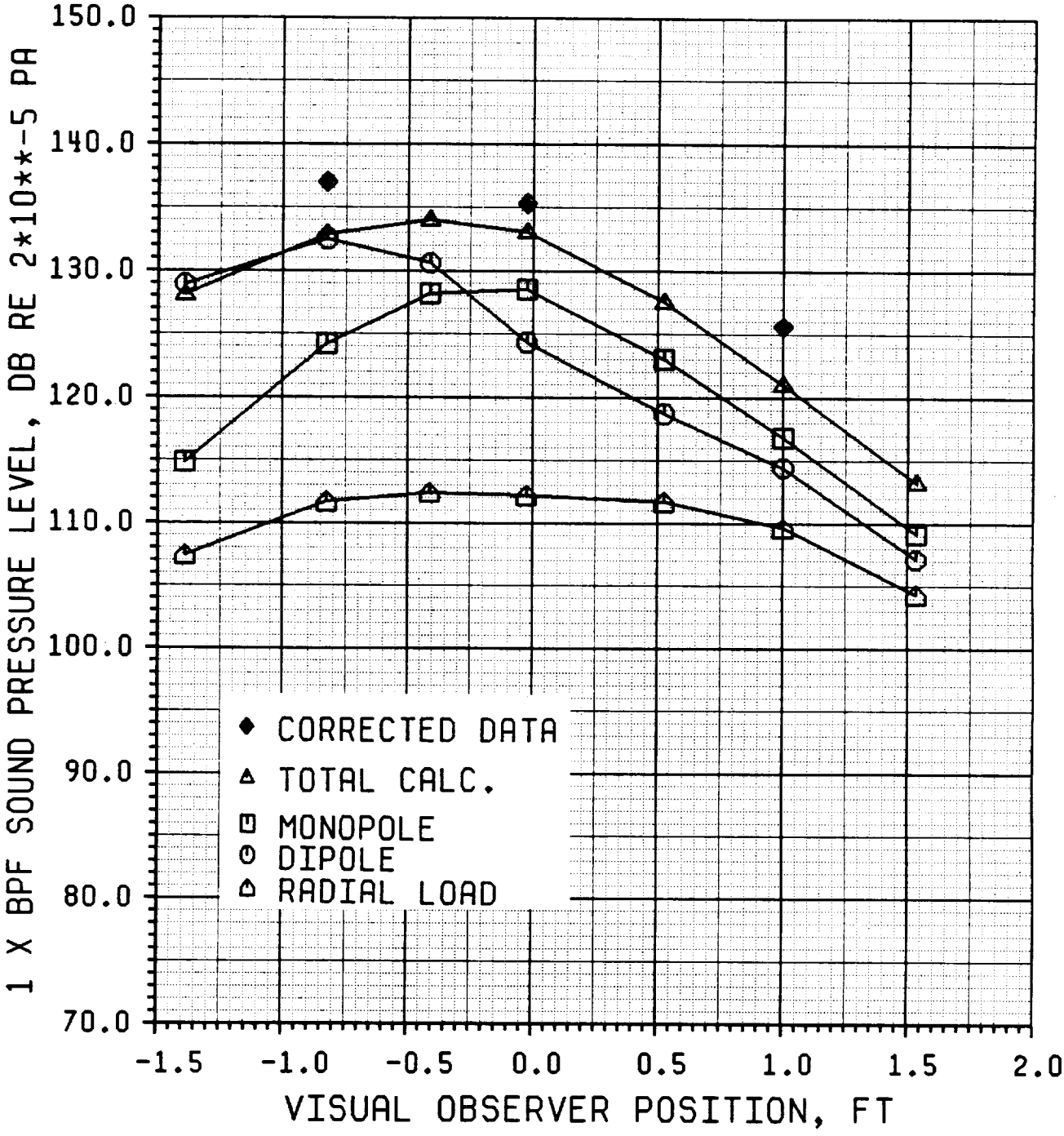

Figure 58 Comparison of measured and predicted directivity of BPF tone at 0.8 diameter sideline. SR-3 model at 30000 ft. altitude, 0.71 flight Mach number, 3.06 advance ratio, and 1.84 CP. Noise predicted with tip force acting in the radial direction. Compare with Figure 50.

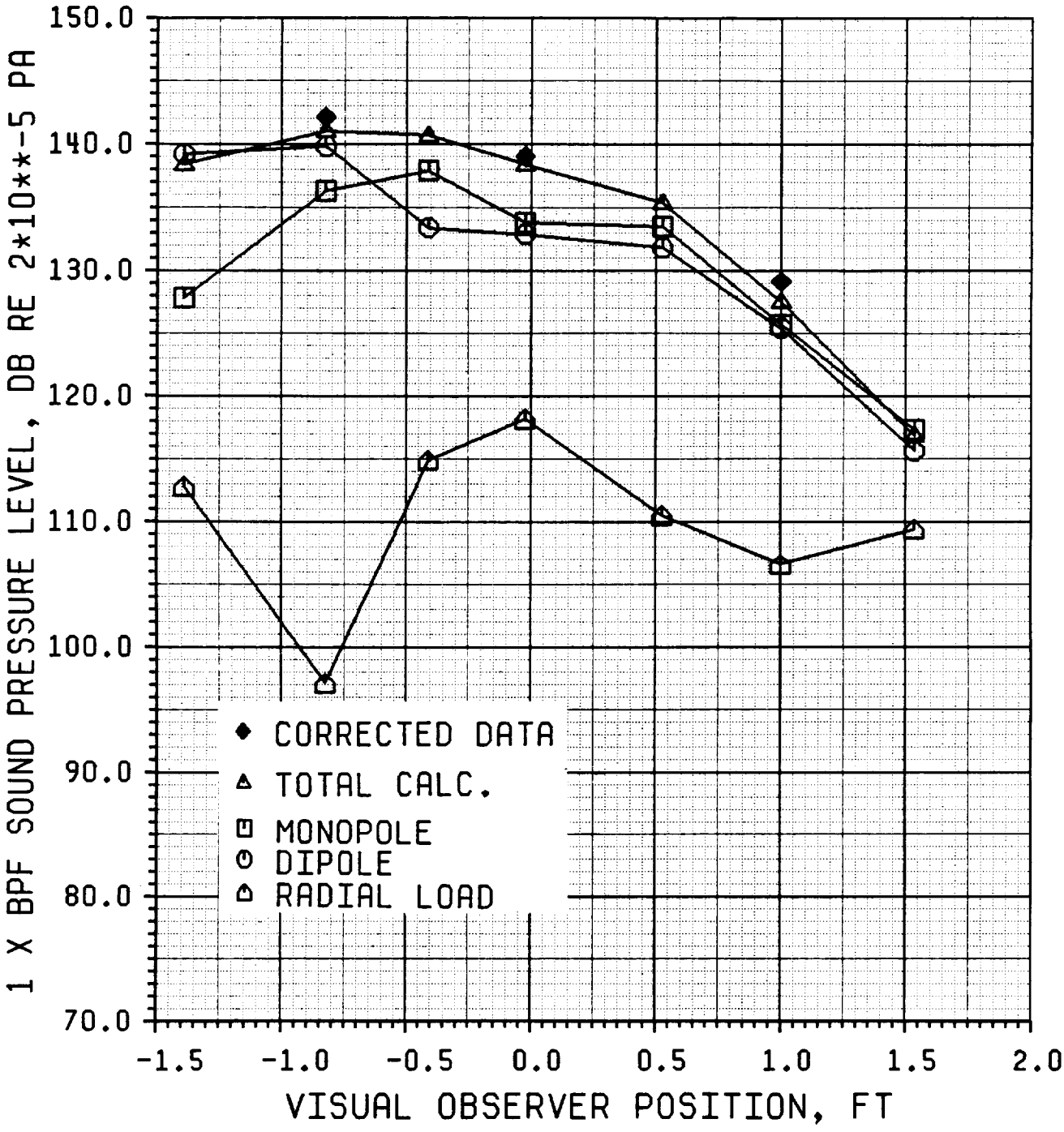

Figure 59 Comparison of measured and predicted directivity of BPF tone at 0.8 diameter sideline. SR-3 model at 30000 ft. altitude, 0.79 flight Mach number, 3.03 advance ratio, and 1.83 CP. Noise predicted with tip force acting in the radial direction. Compare with Figure 51.

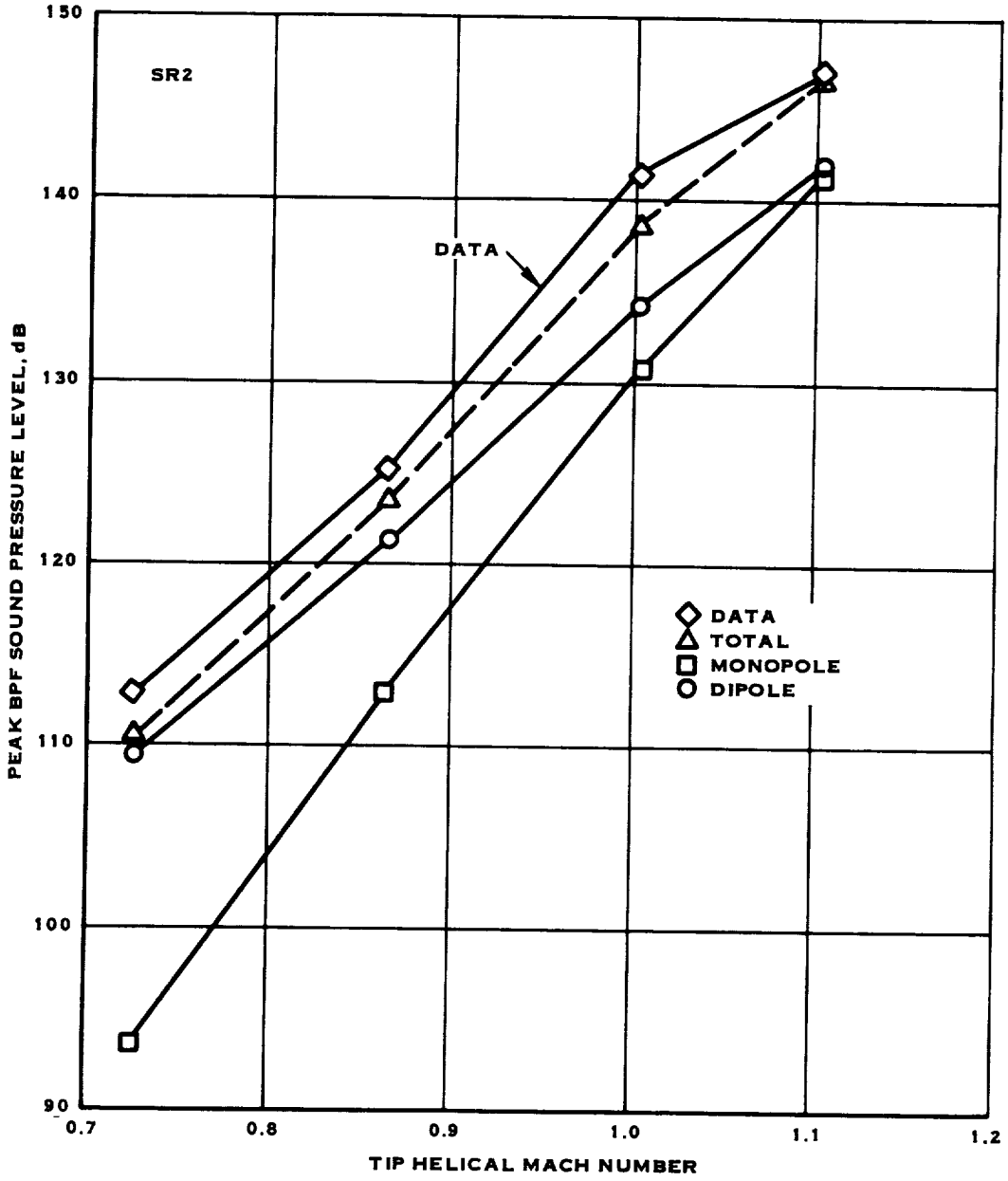

Figure 60 Maximum measured and predicted noise levels on a 0.8 diameter sideline plotted as a function of tip relative Mach number for the SR-2 model. 20000 ft. altitude data corrected to 30000 ft. pressure altitude.

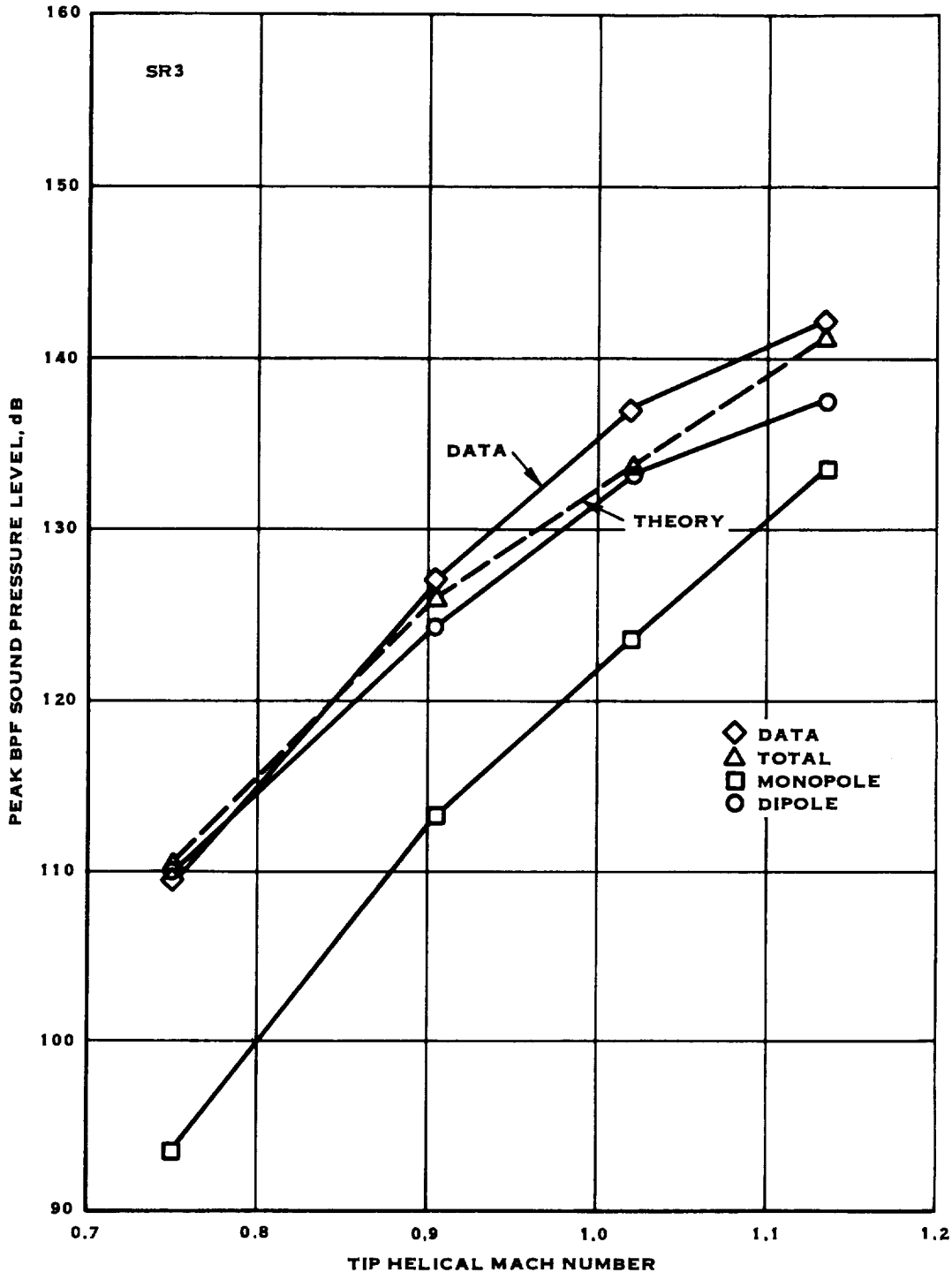

Figure 61 Maximum measured and predicted noise levels on a 0.8 diameter sideline plotted as a function of tip relative Mach number for the SR-3 model. 20000 ft. altitude data corrected to 30000 ft. pressure altitude.

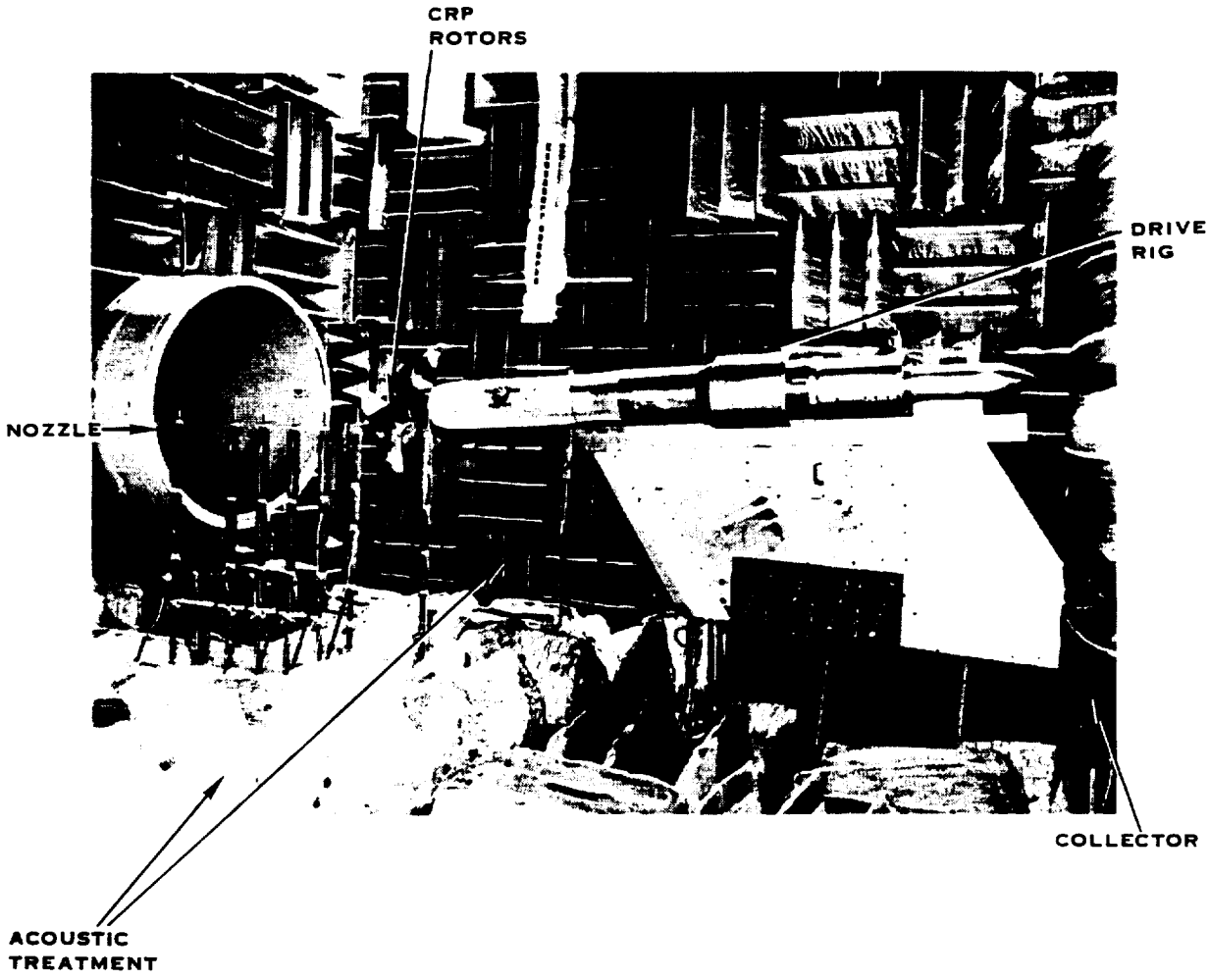

Figure 62 Photograph of CRP-X1 model in the UTRC Acoustic Wind Tunnel (taken from Ref. 23).

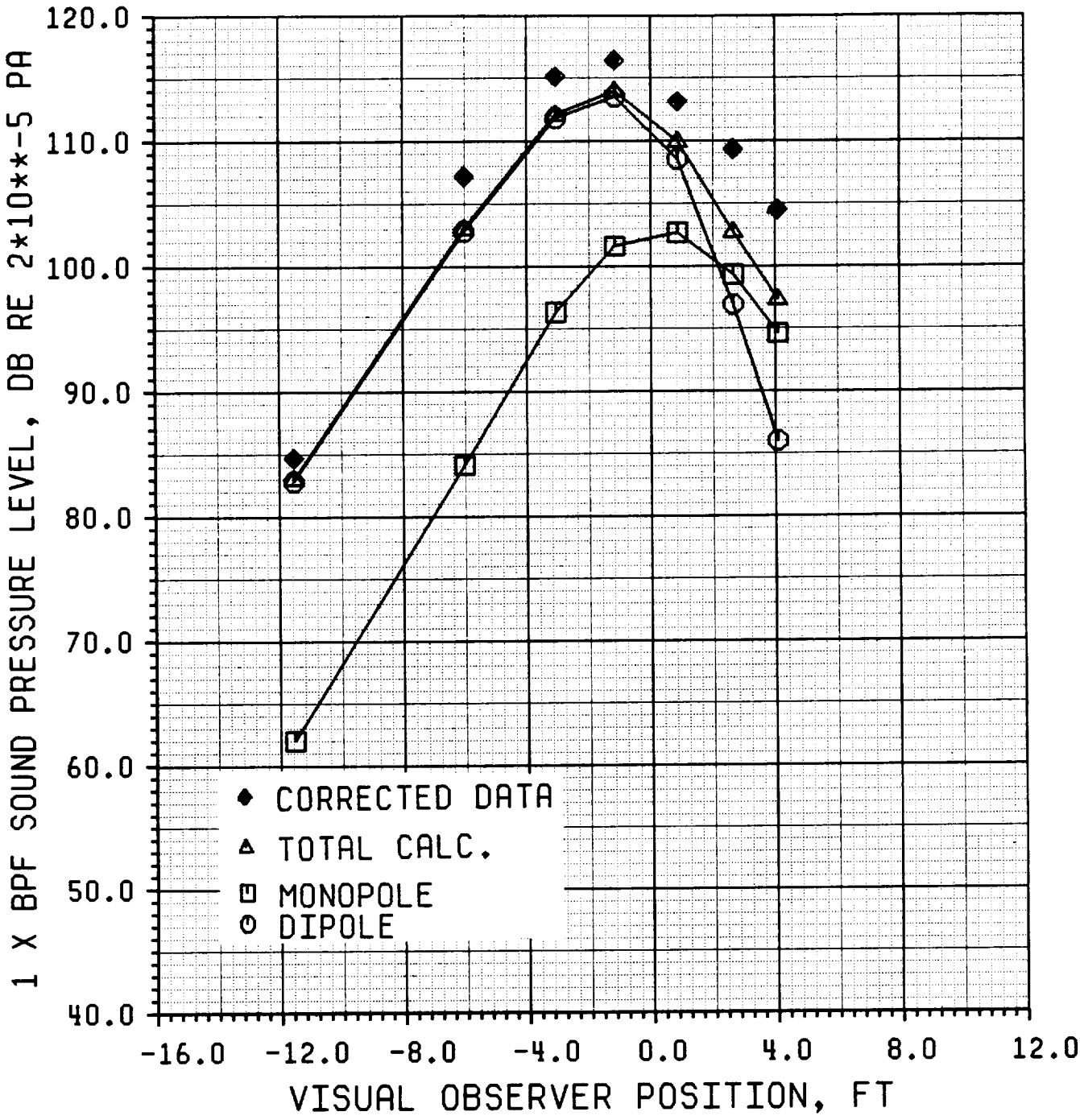

Figure 63 Comparison of measured and predicted directivity of BPF tone at 3.0 diameter sideline. CRP-X1 model at 0.26 flight Mach number, 1.18 advance ratio, and 0.349 CP. Noise predicted using standard (default) procedure (tip vortex loading acts normal to blade surface).

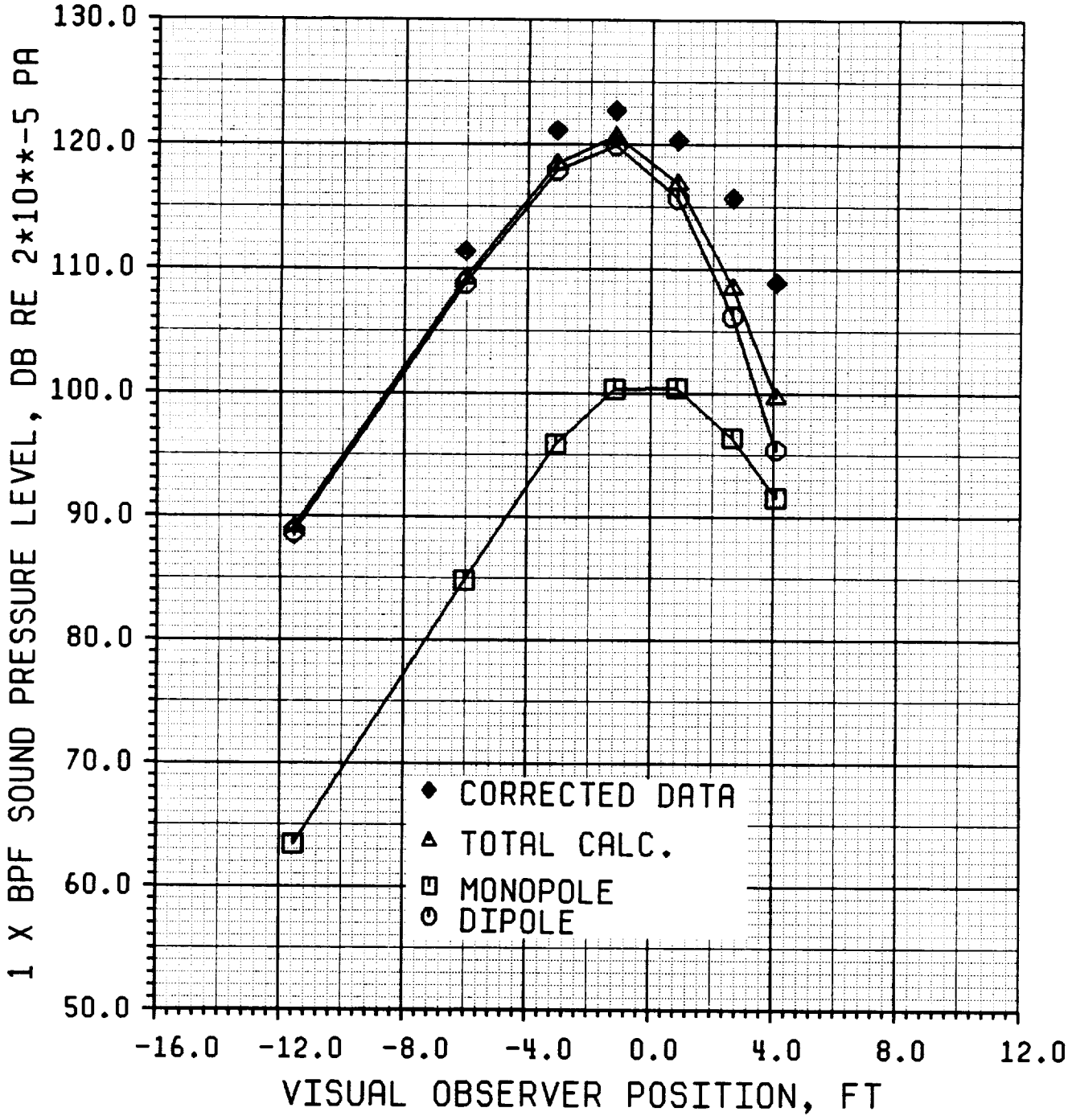

Figure 64 Comparison of measured and predicted directivity of BPF tone at 3.0 diameter sideline. CRP-X1 model at 0.26 flight Mach number, 1.18 advance ratio, and 0.699 CP. Noise predicted using standard (default) procedure (tip vortex loading acts normal to blade surface).

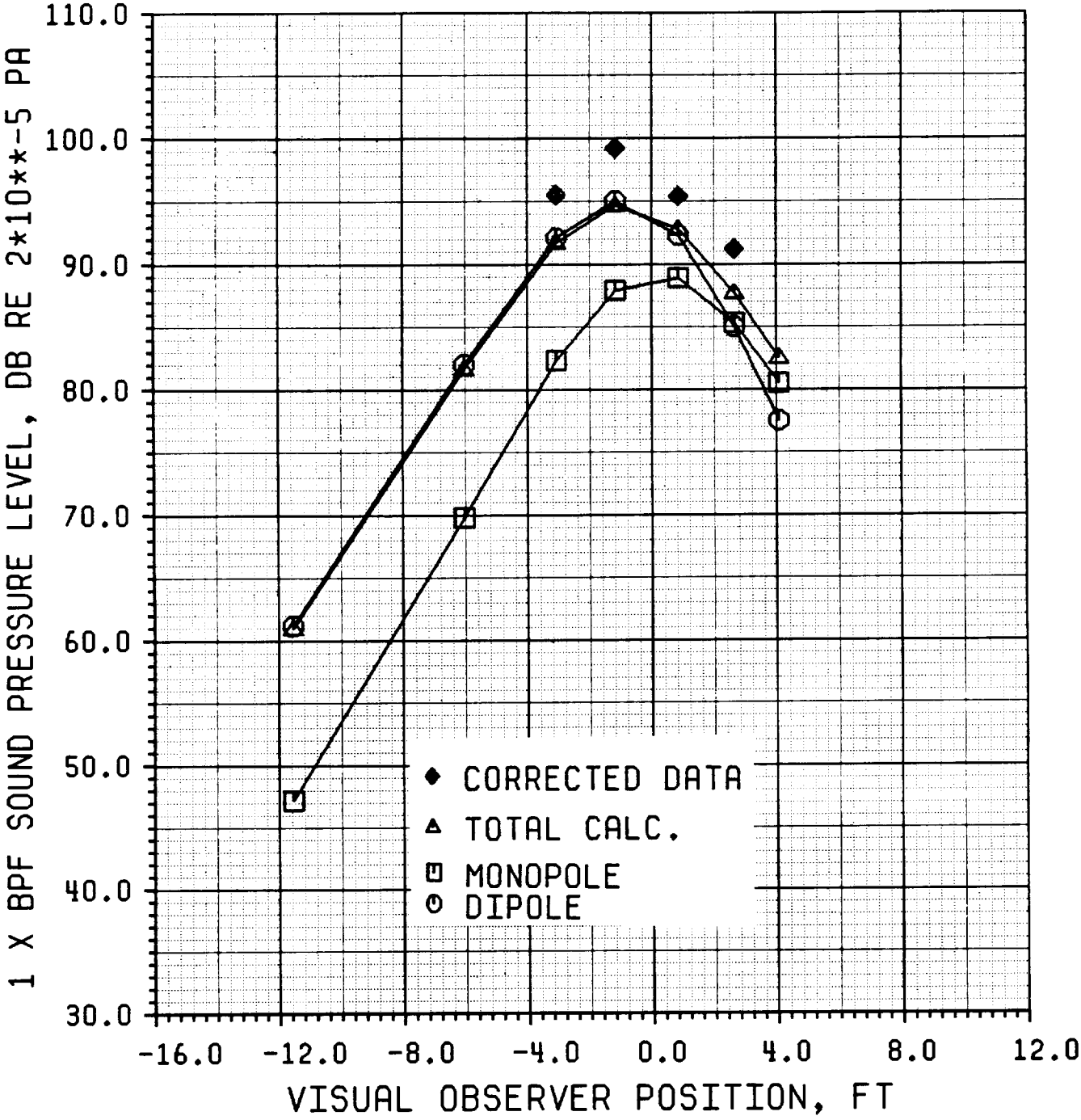

Figure 65 Comparison of measured and predicted directivity of BPF tone at 3.0 diameter sideline. CRP-X1 model at 0.26 flight Mach number, 1.51 advance ratio, and 0.145 CP. Noise predicted using standard (default) procedure (tip vortex loading acts normal to blade surface).

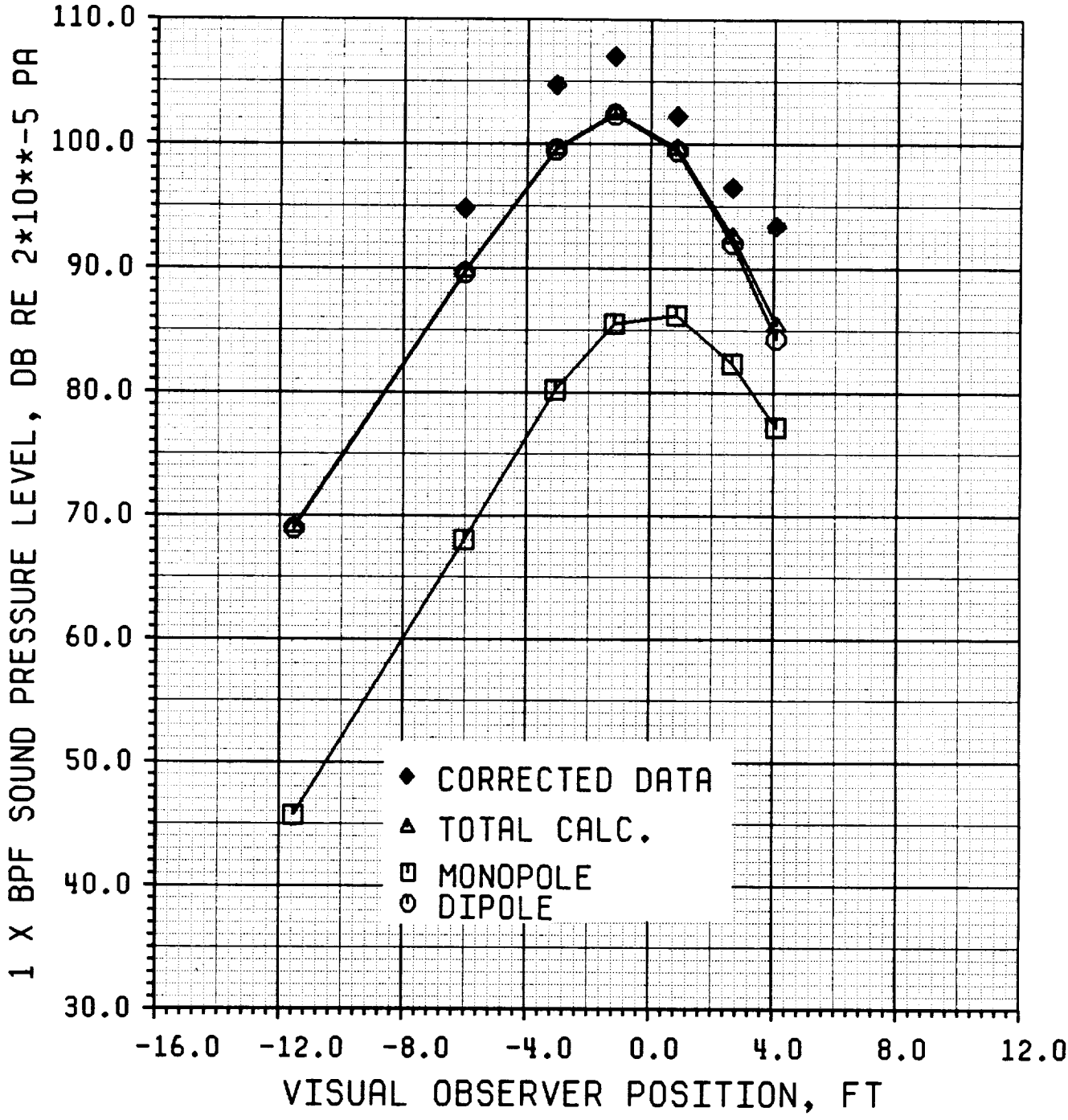

Figure 66 Comparison of measured and predicted directivity of BPF tone at 3.0 diameter sideline. CRP-X1 model at 0.26 flight Mach number, 1.51 advance ratio, and 0.477 CP. Noise predicted using standard (default) procedure (tip vortex loading acts normal to blade surface).

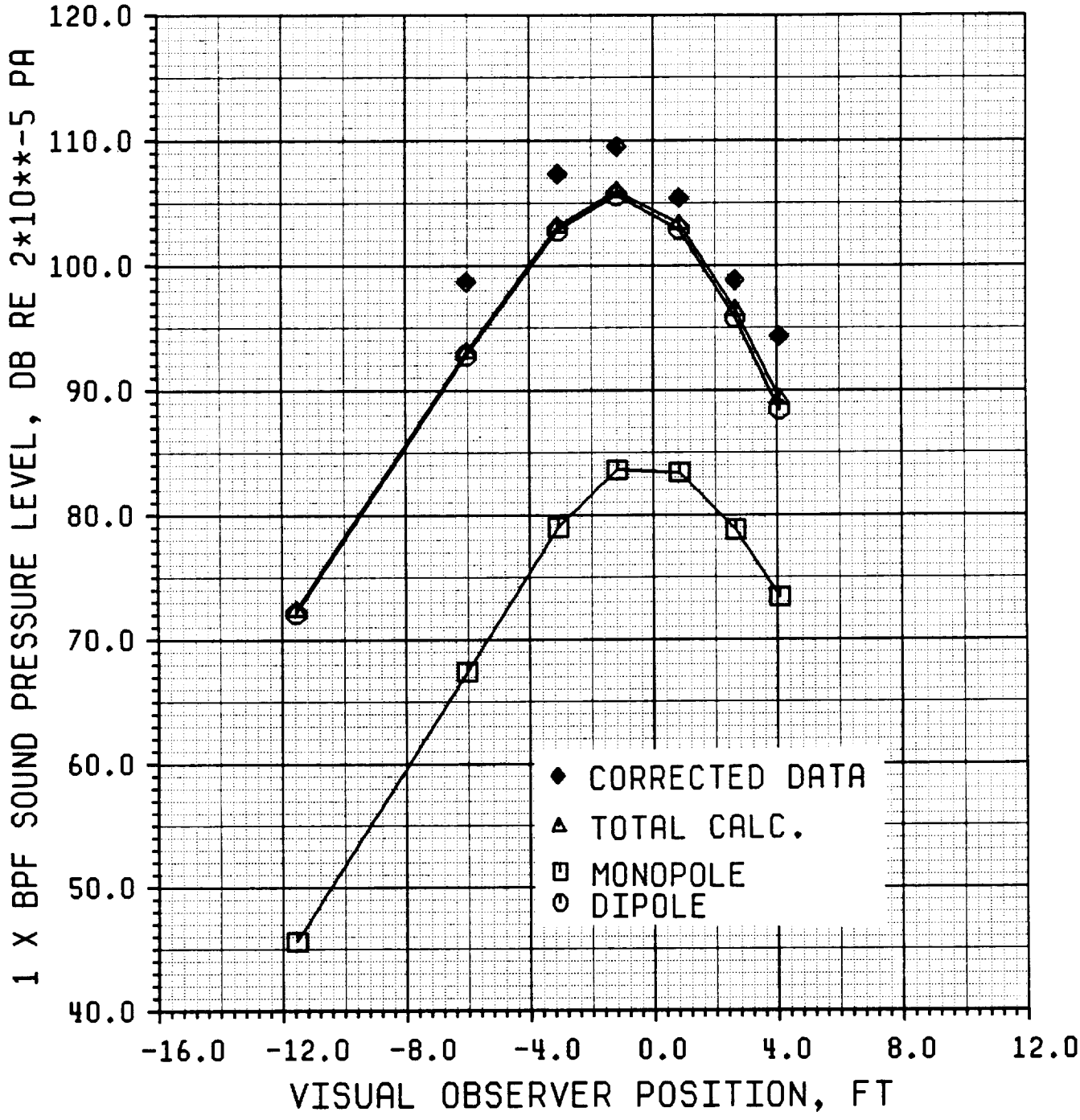

Figure 67 Comparison of measured and predicted directivity of BPF tone at 3.0 diameter sideline. CRP-X1 model at 0.26 flight Mach number, 1.51 advance ratio, and 0.678 CP. Noise predicted using standard (default) procedure (tip vortex loading acts normal to blade surface).

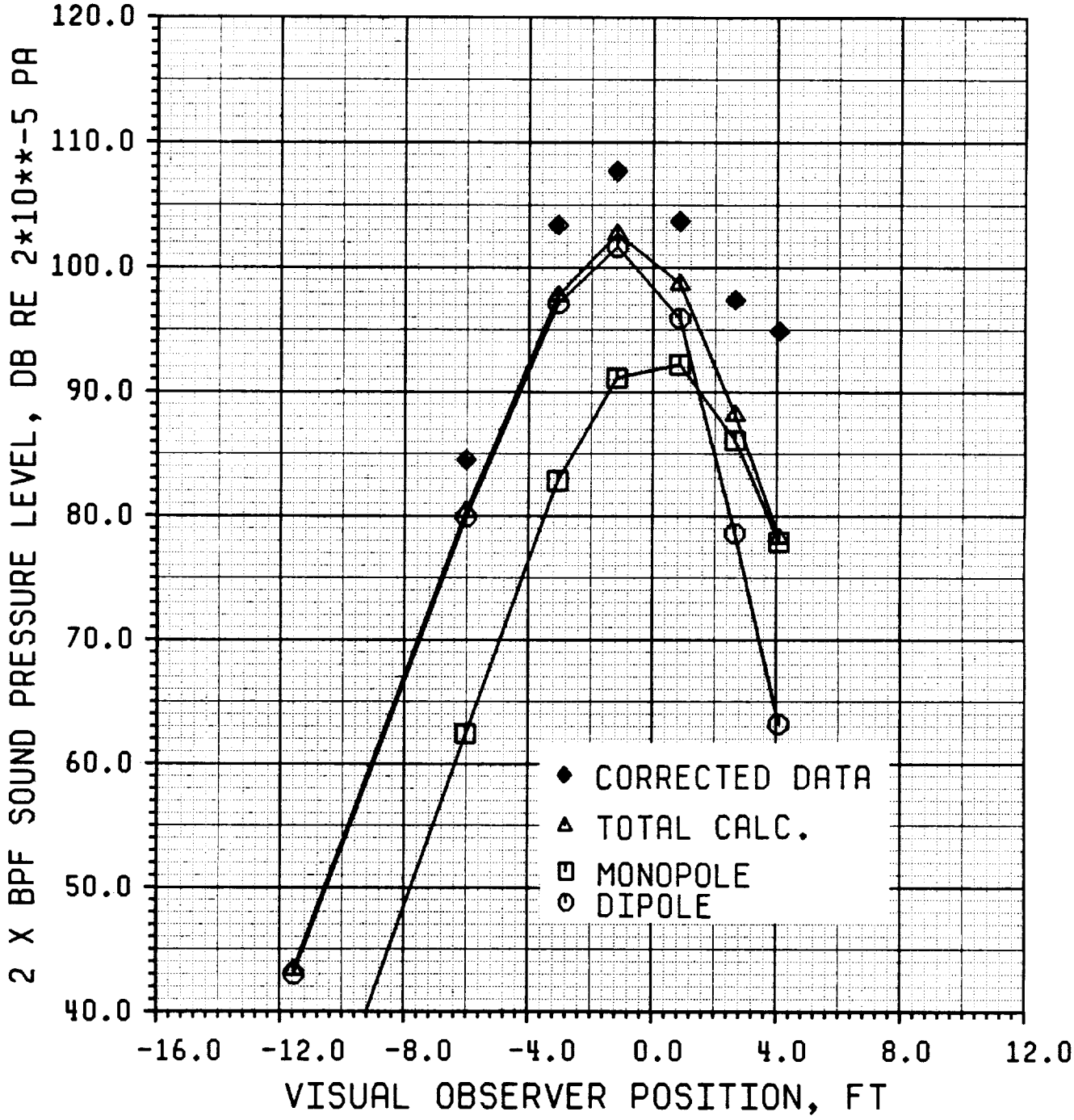

Figure 68 Comparison of measured and predicted directivity of 2xBPF tone at 3.0 diameter sideline. CRP-X1 model at 0.26 flight Mach number, 1.18 advance ratio, and 0.349 CP. Noise predicted using standard (default) procedure (tip vortex loading acts normal to blade surface).

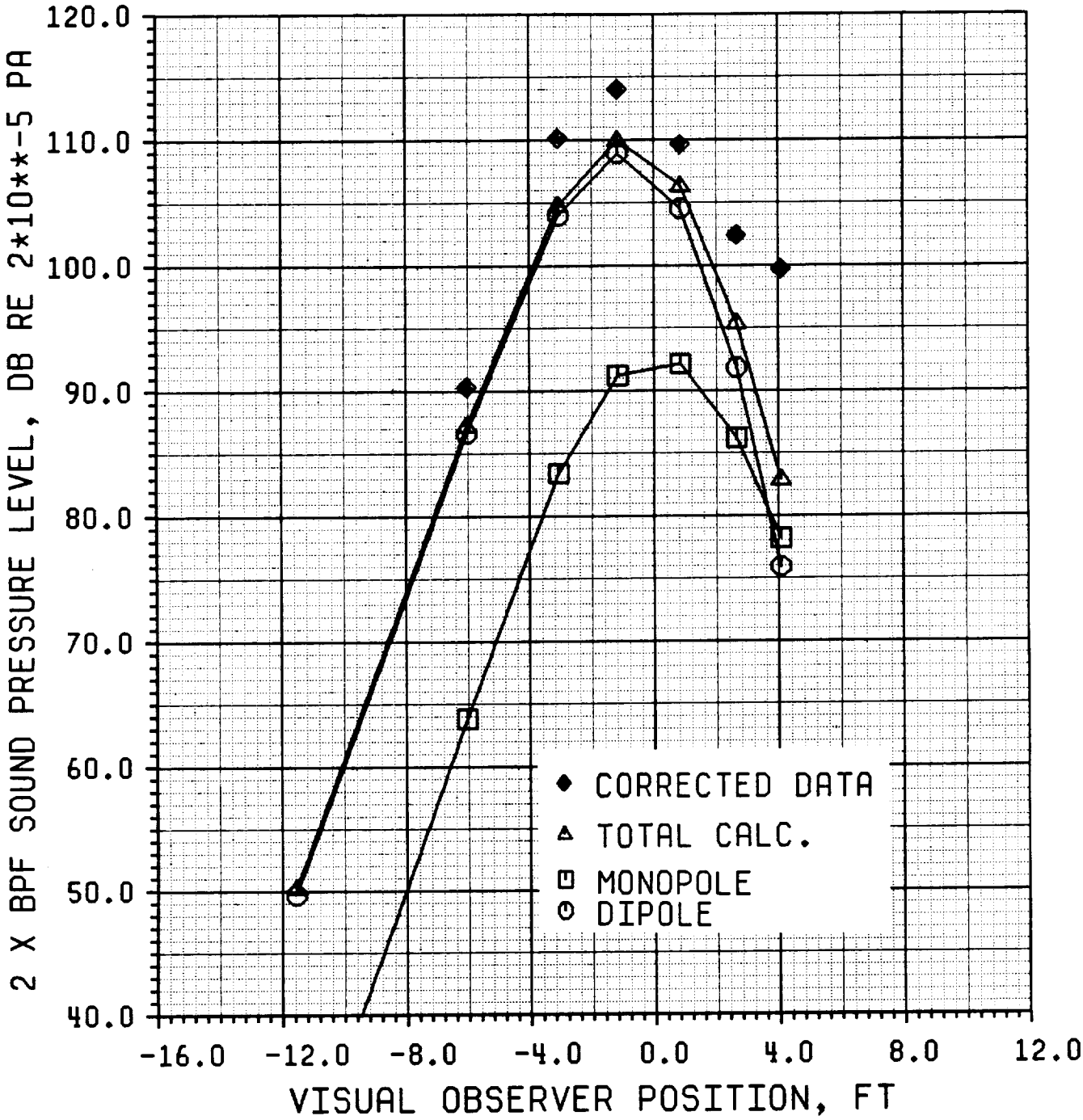

Figure 69 Comparison of measured and predicted directivity of 2xBPF tone at 3.0 diameter sideline. CRP-X1 model at 0.26 flight Mach number, 1.18 advance ratio, and 0.699 CP. Noise predicted using standard (default) procedure (tip vortex loading acts normal to blade surface).

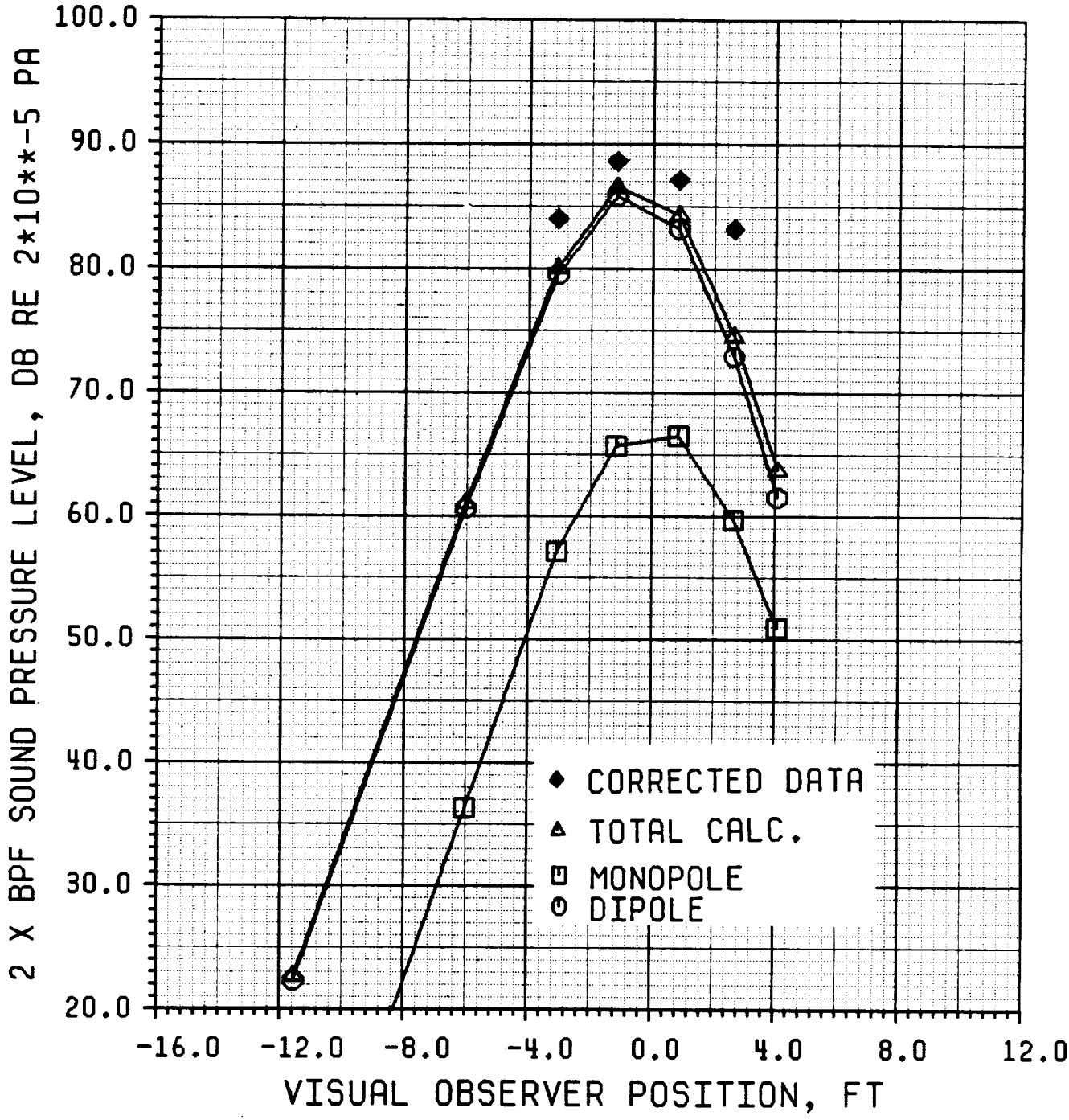

Figure 70 Comparison of measured and predicted directivity of 2xBPF tone at 3.0 diameter sideline. CRP-X1 model at 0.26 flight Mach number, 1.51 advance ratio, and 0.678 CP. Noise predicted using standard (default) procedure (tip vortex loading acts normal to blade surface).

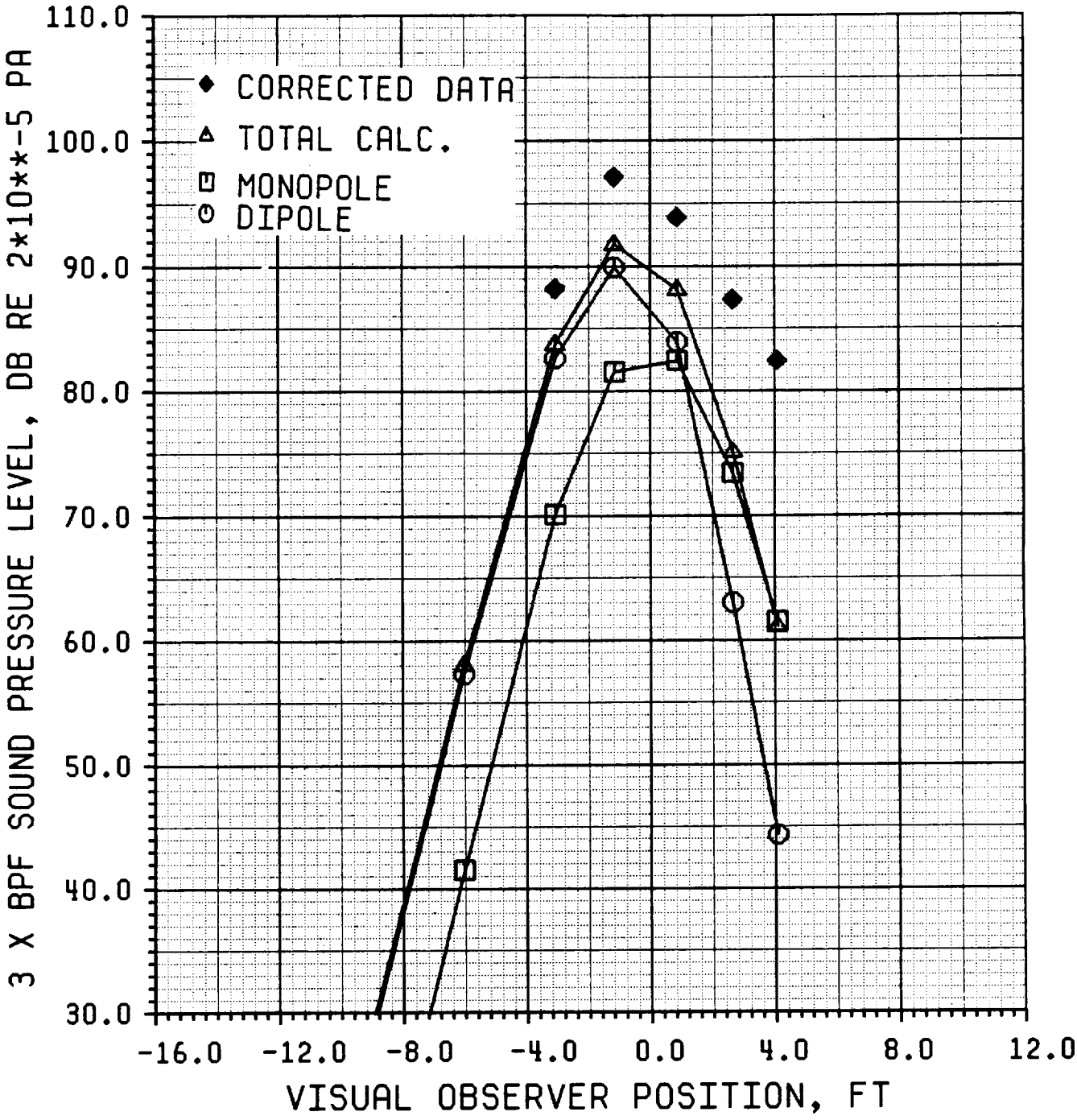

Figure 71 Comparison of measured and predicted directivity of 3xBPF tone at 3.0 diameter sideline. CRP-X1 model at 0.26 flight Mach number, 1.18 advance ratio, and 0.349 CP. Noise predicted using standard (default) procedure (tip vortex loading acts normal to blade surface).

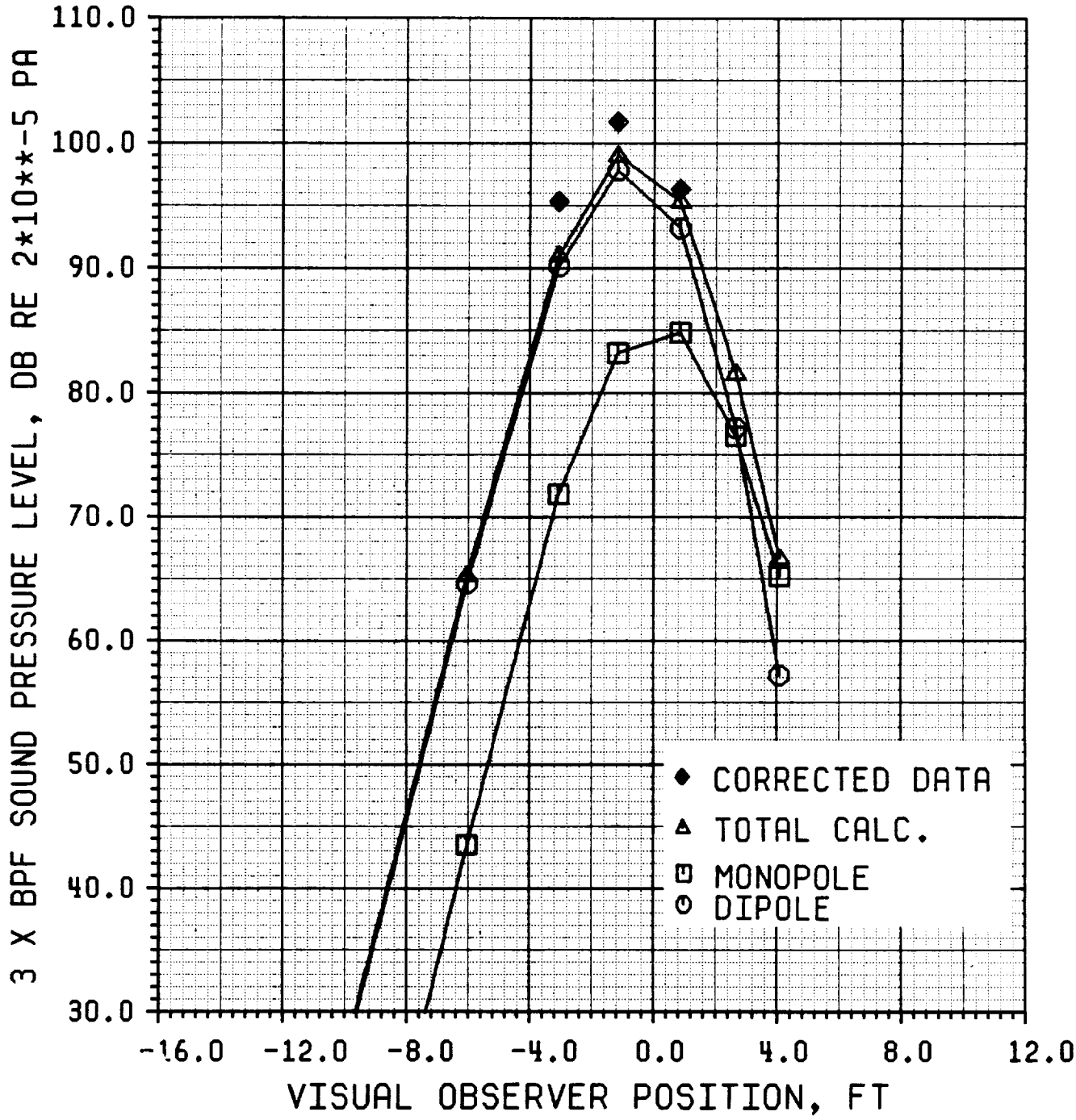

Figure 72 Comparison of measured and predicted directivity of 3xBPF tone at 3.0 diameter sideline. CRP-X1 model at 0.26 flight Mach number, 1.18 advance ratio, and 0.699 CP. Noise predicted using standard (default) procedure (tip vortex loading acts normal to blade surface).

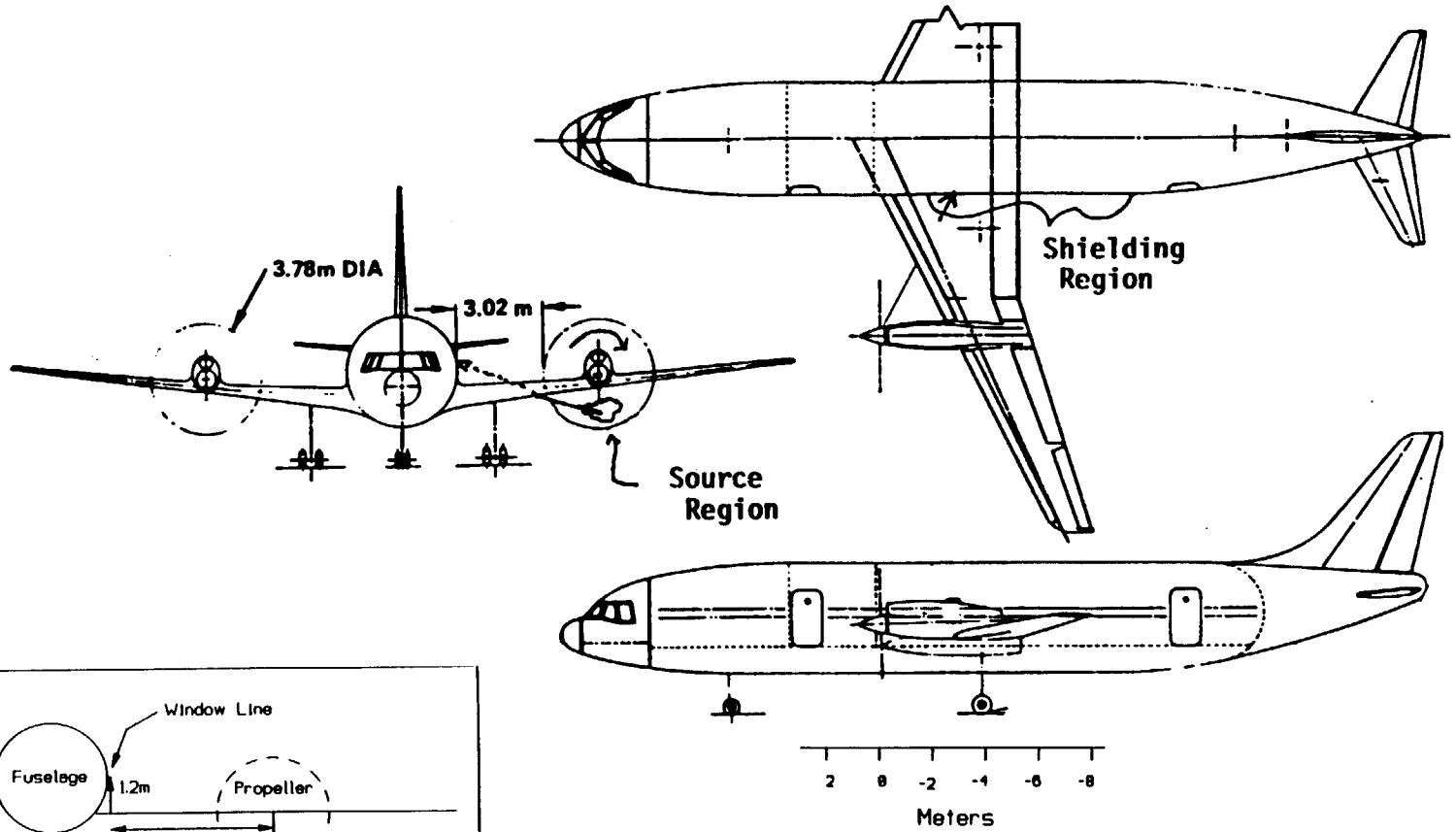

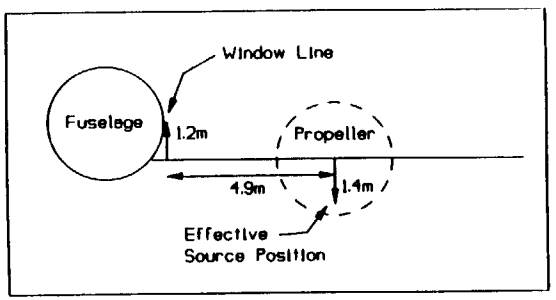

Dimensions for Calculations

Figure 73 Airplane configuration for sample calculations of wing shielding and boundary layer transmission effects.

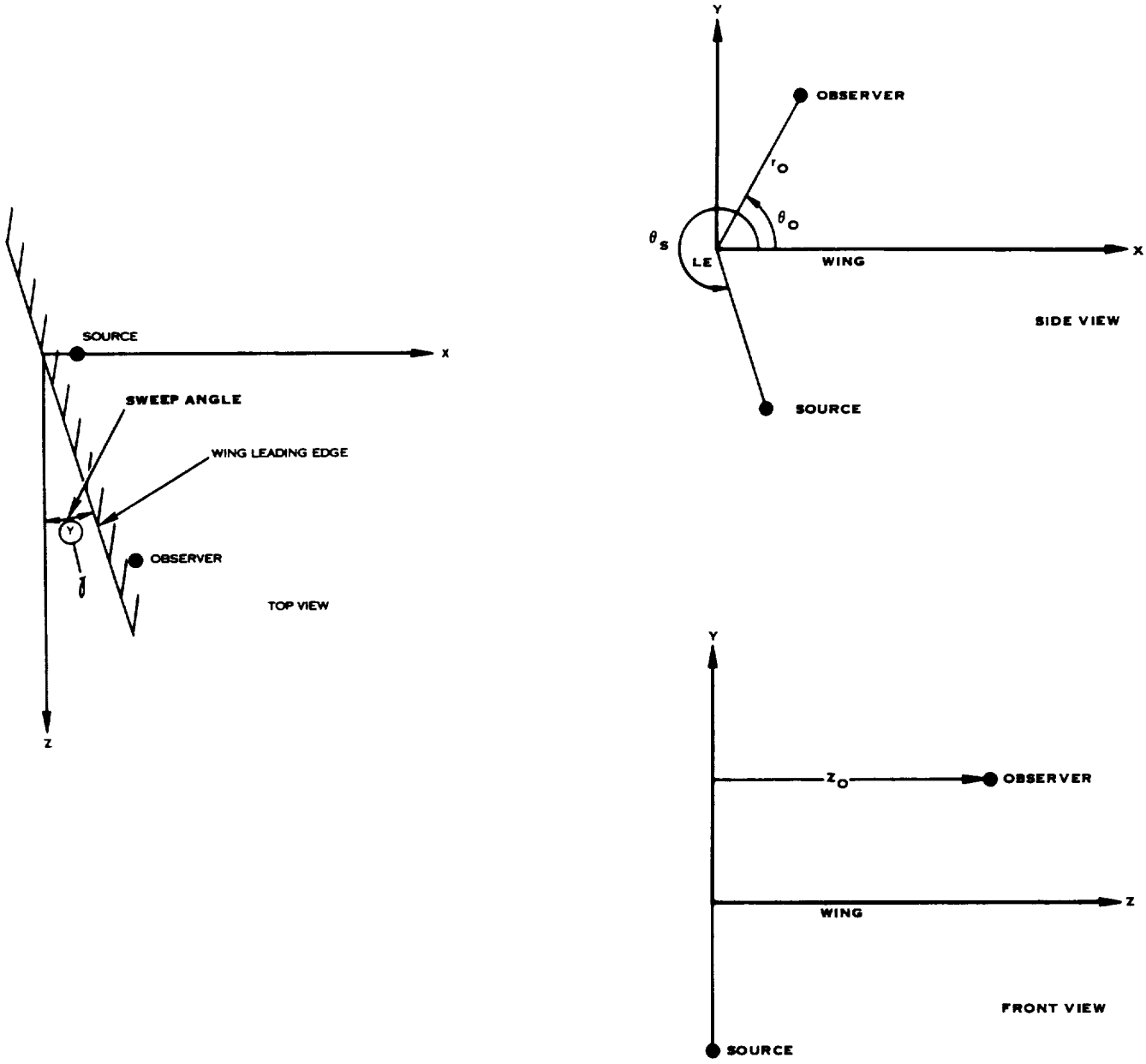

Figure 74 Illustration of the coordinate system used in wing shielding calculations. The geometry shown is for calculation of diffraction at the wing leading edge.

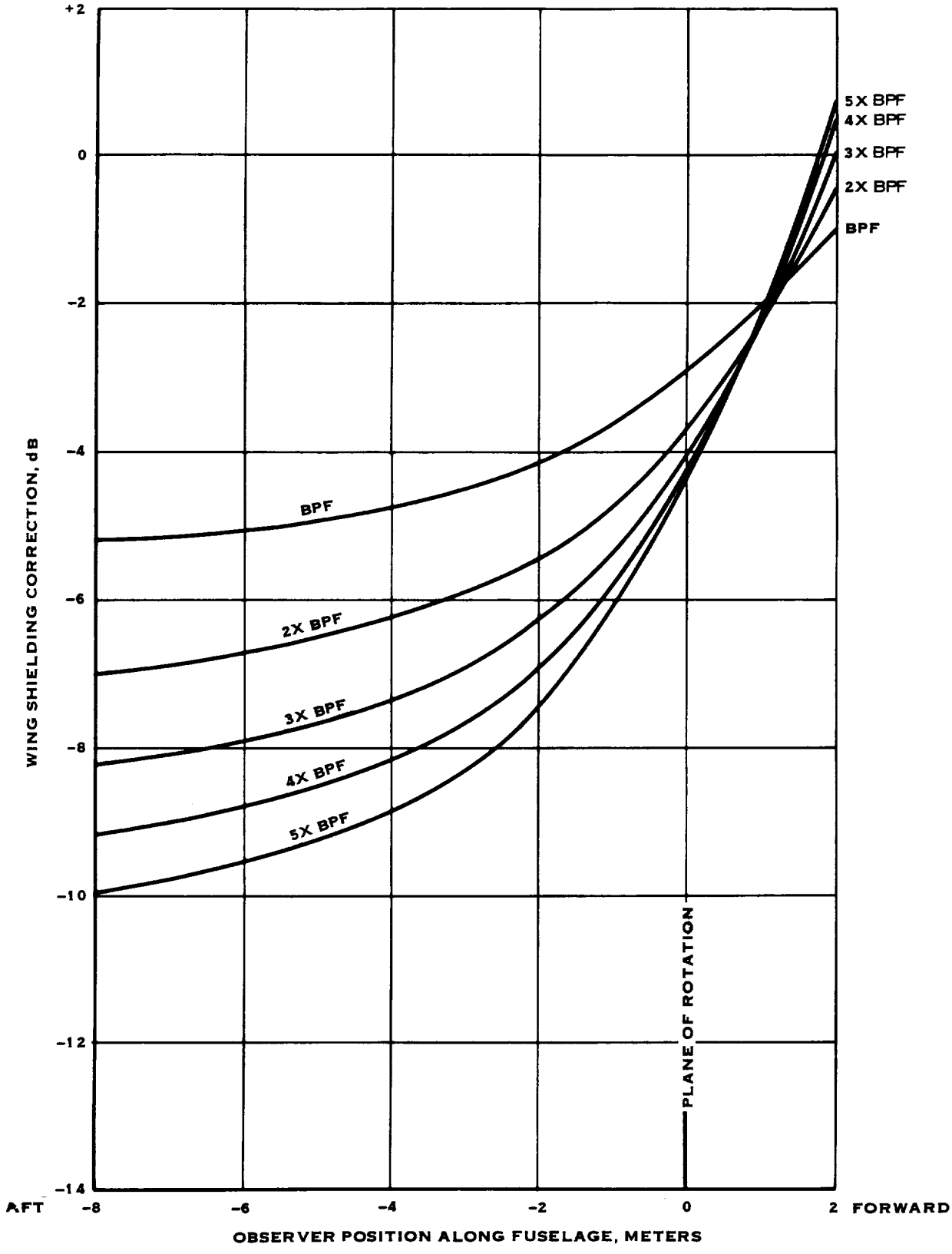

Figure 75 Noise reduction due to wing shielding at 0.15 Mach number. The corrections shown are to be added to calculated noise levels.

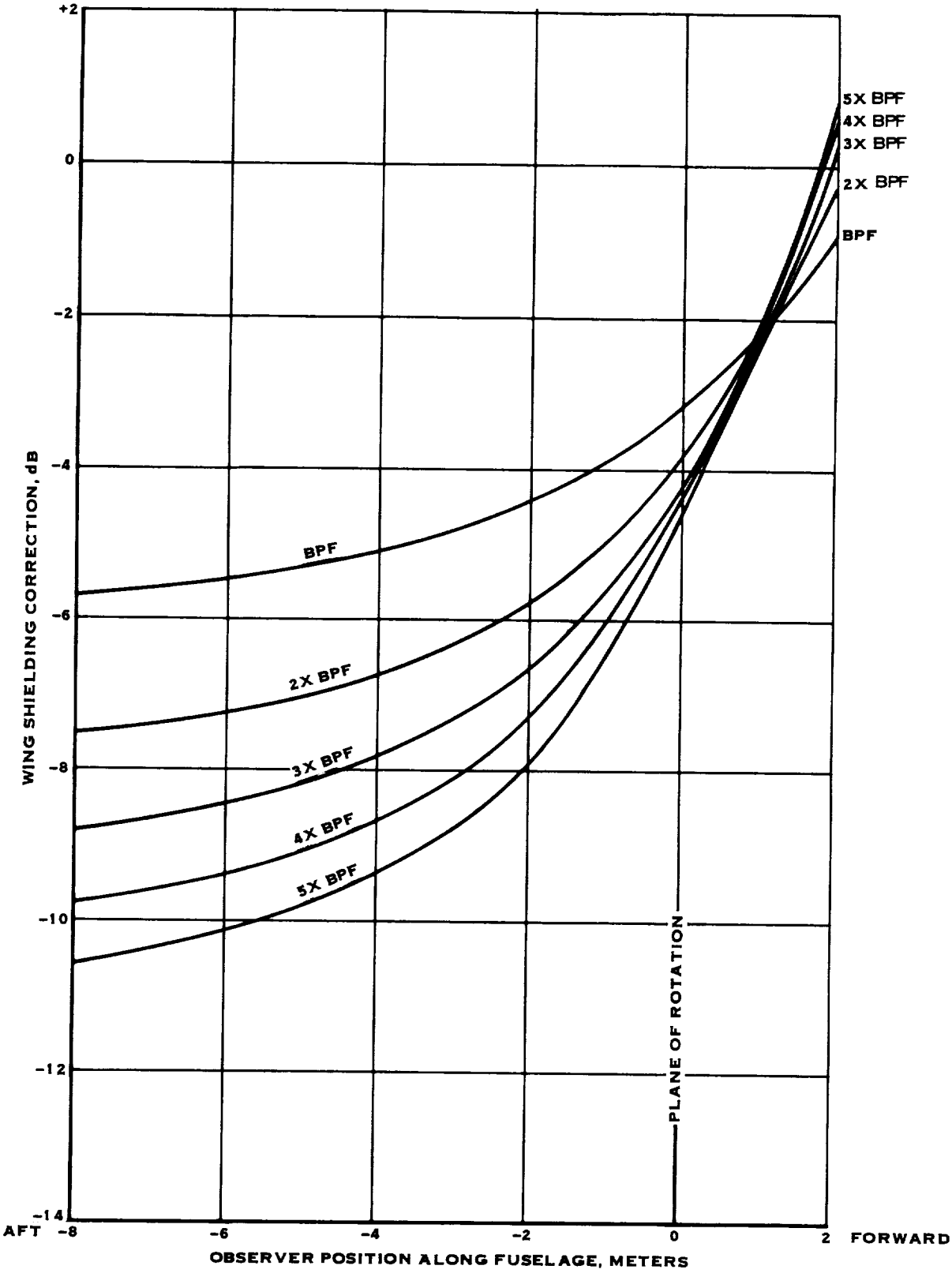

Figure 76 Noise reduction due to wing shielding at 0.25 Mach number. The corrections shown are to be added to calculated noise levels.

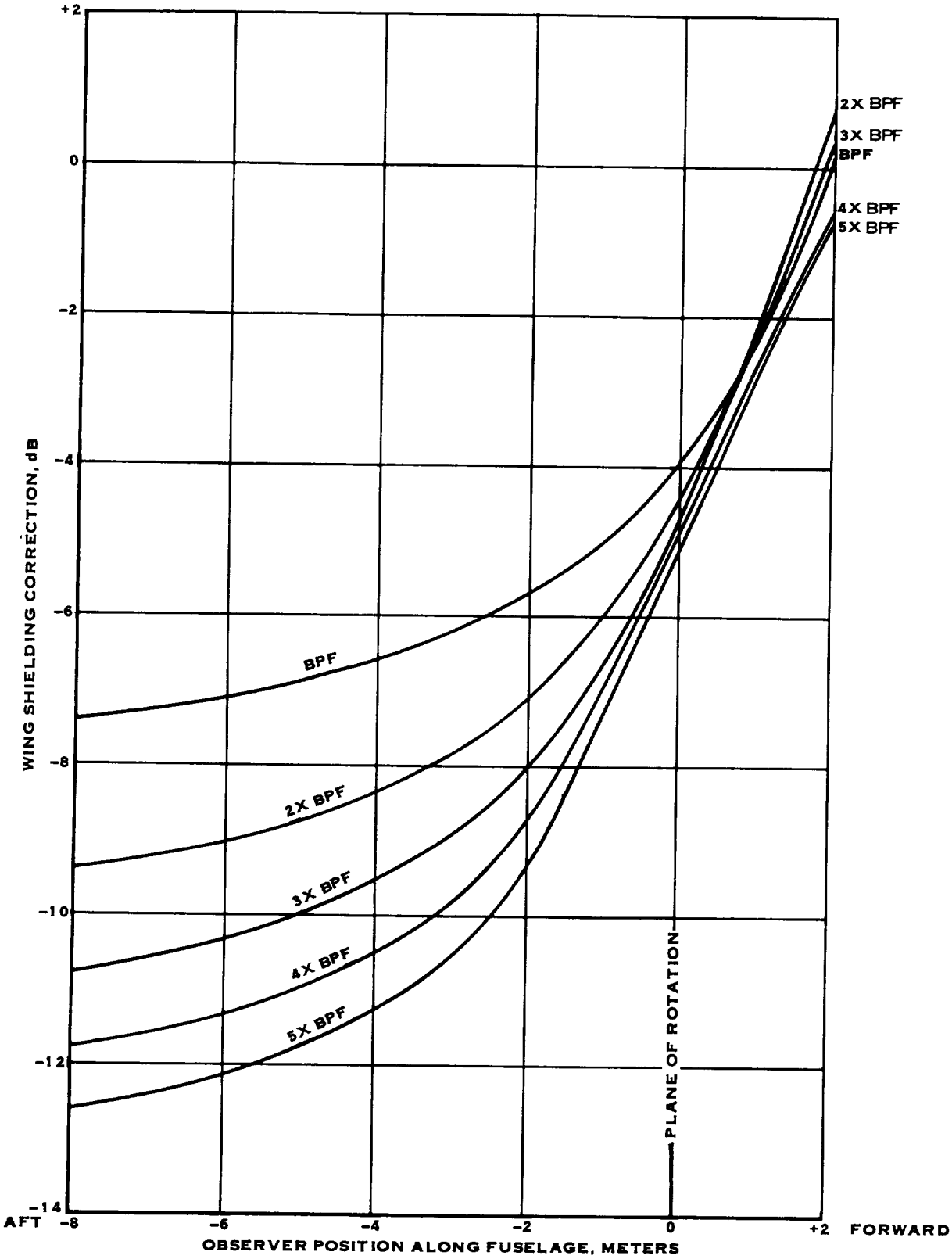

Figure 77 Noise reduction due to wing shielding at 0.8 Mach number. The corrections shown are to be added to calculated noise levels.

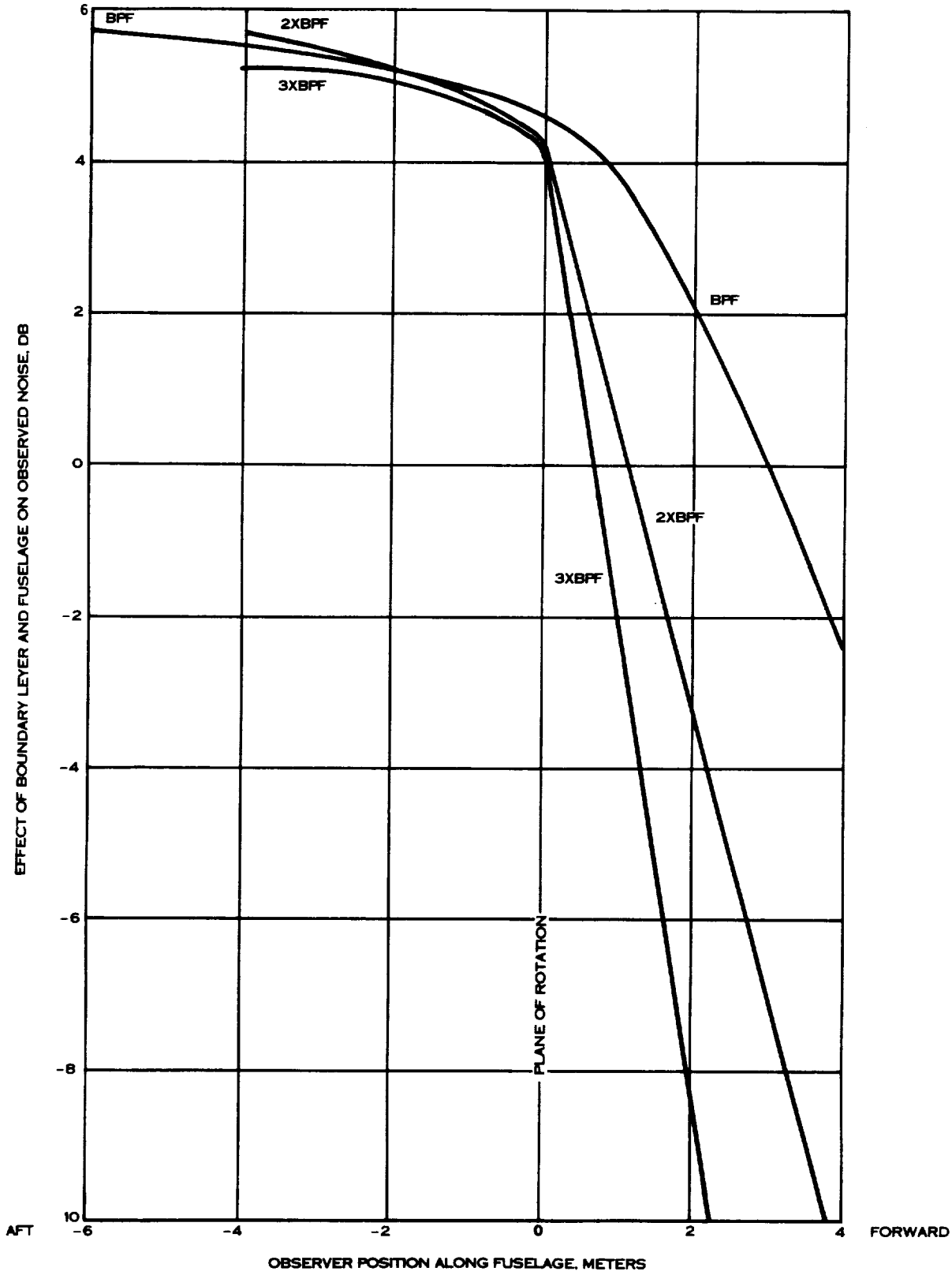

Figure 78 Noise reduction due to refraction by the fuselage boundary layer at 0.8 Mach number. Reflection effects at the fuselage surface have not been included. The corrections shown are to be added to calculated noise levels.

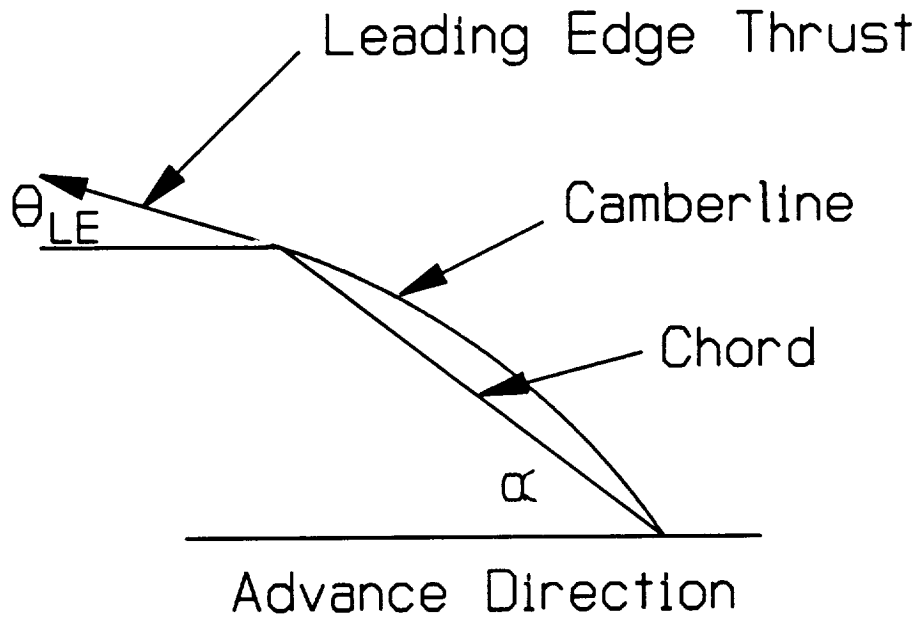

Figure 79 Sketch of section camber line for vortex loading discussion.

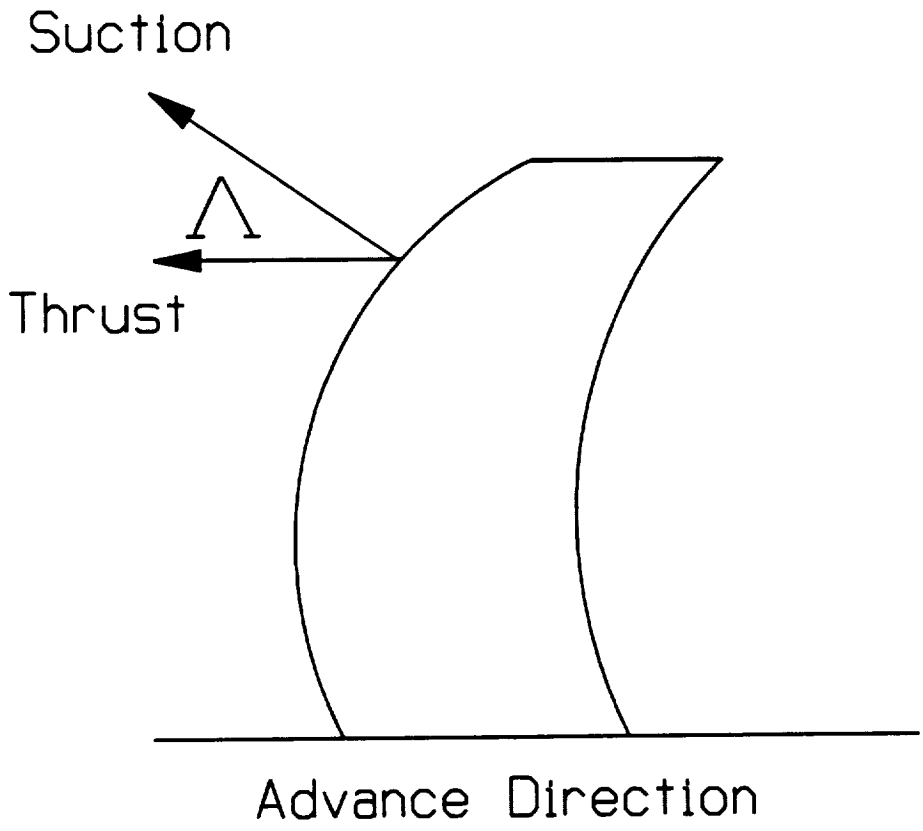

Figure 80 Sketch of blade planform for vortex loading discussion.

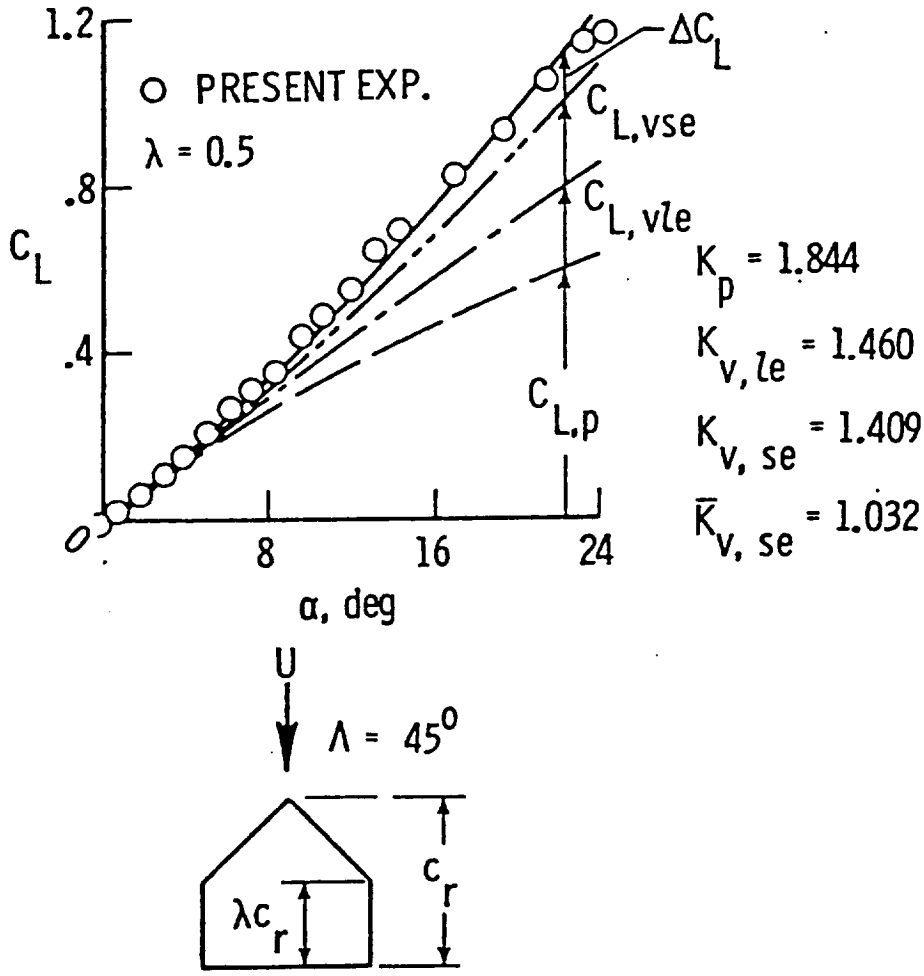

Figure 81. Comparison of measured and predicted wing lift coefficients showing the contributions of vortex lift components (taken from Ref. 11)

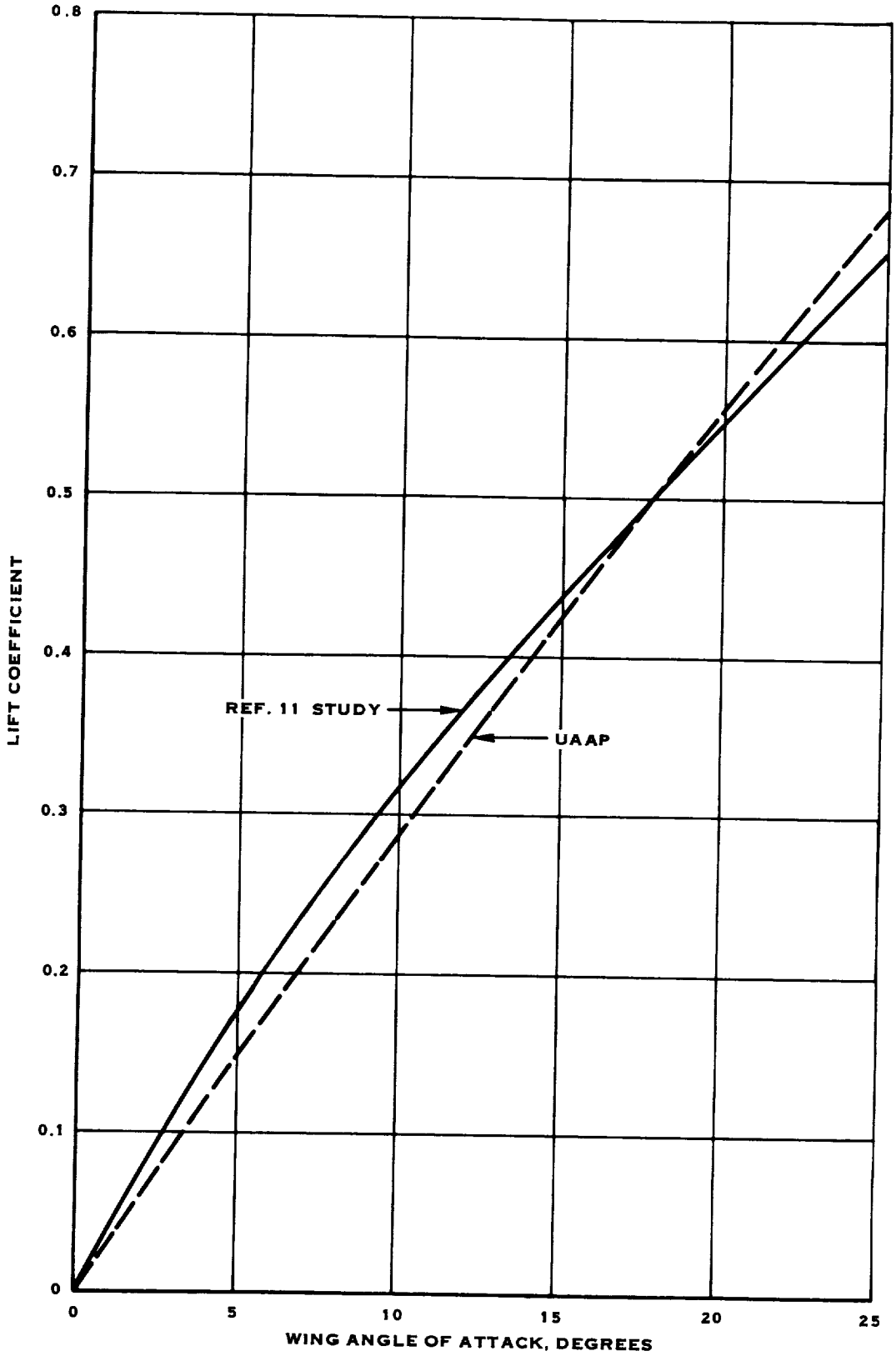

Figure 82. Comparision of wing and propeller potential lift.

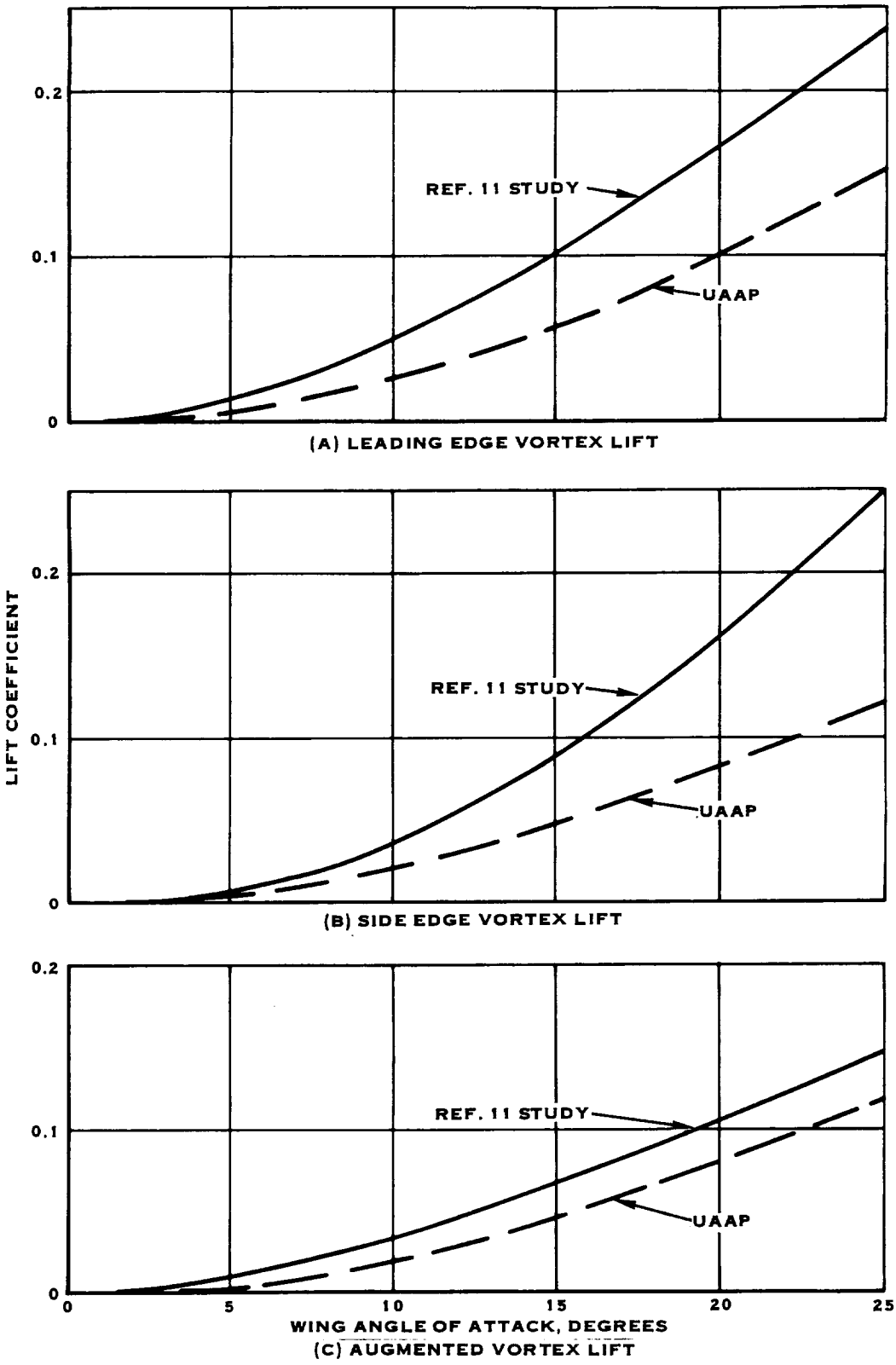

Figure 83. Comparison of wing and propeller vortex loading components.

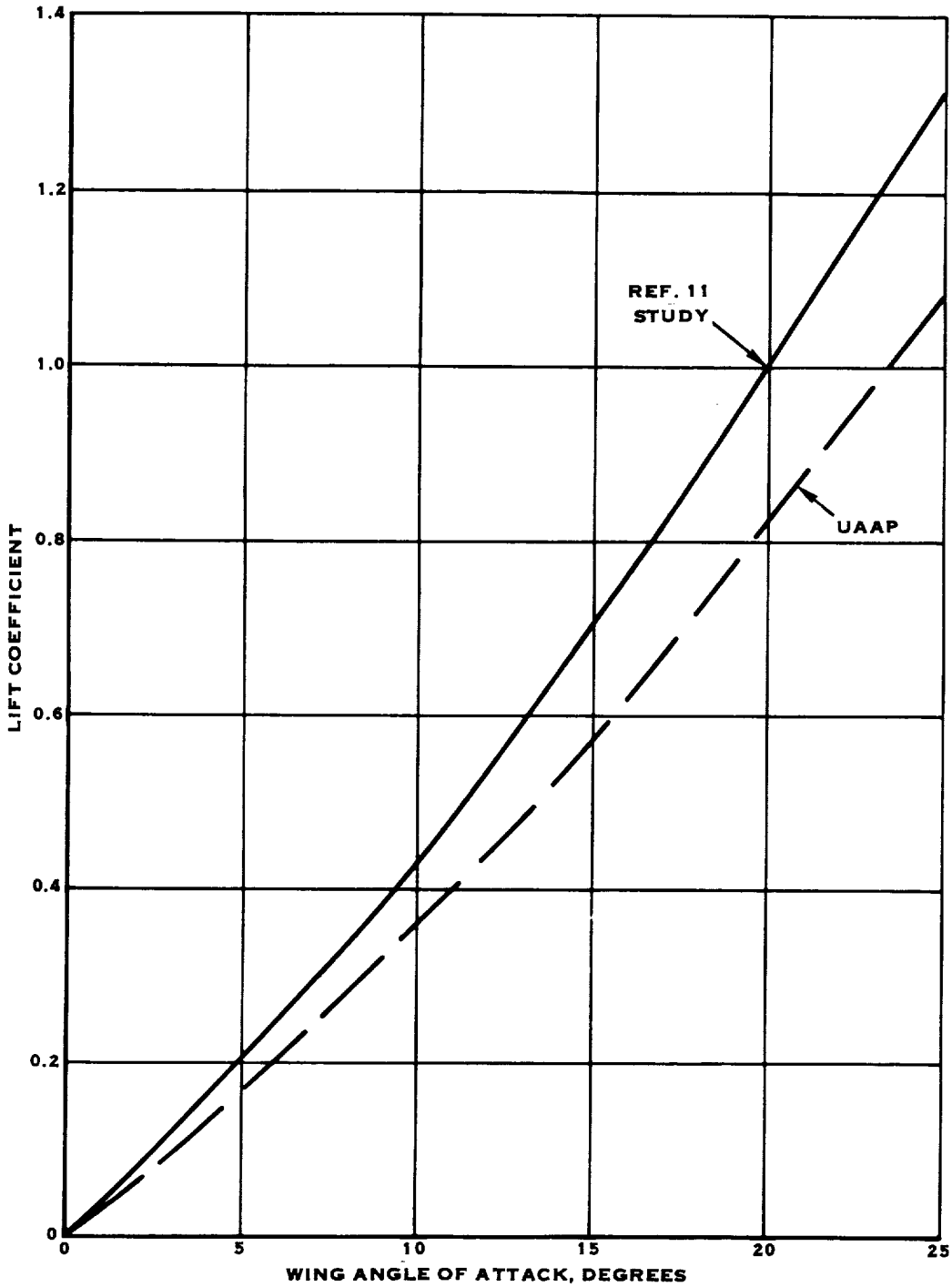

Figure 84. Comparison of wing and propeller overall lift.

NASA
National Aeronautics and Space Administration

Report Documentation Page

1. Report No.	2. Government Accession No.	3. Recipient's Catalog No.
NASA CR 185193		

4. Title and Subtitle	5. Report Date
Unified Aeroacoustics Analysis for High Speed Turboprop Aerodynamics and Noise. Volume III - Application of Theory for Blade Loading, Wakes, Noise, and Wing Shielding.	May 1991
	6. Performing Organization Code

7. Author(s)	8. Performing Organization Report No.
D.B. Hanson, C.J. McColgan, R.M. Ladden, R.J. Klatte	None
	10. Work Unit No. 535-03-01

9. Performing Organization Name and Address	11. Contract or Grant No.
Hamilton Standard Division United Technologies Corporation PO Box 1000 Windsor Locks, CT 06096	NAS3-23720
	13. Type of Report and Period Covered Contractor Report Final
12. Sponsoring Agency Name and Address National Aeronautics and Space Administration Lewis Research Center Cleveland, Ohio 44135-3191	14. Sponsoring Agency Code

15. Supplementary Notes

Project Manager, Bruce Clark,
Advanced Turboprop Project Office, NASA Lewis Research Center, Cleveland, Ohio 44135

16. Abstract

This report presents a unified theory for aerodynamics and noise of advanced turboprops. Aerodynamic topics include calculation of performance, blade load distribution, and non-uniform wake flow fields. Blade loading can be steady or unsteady due to fixed distortion, counter-rotating wakes, or blade vibration. The aerodynamic theory is based on the pressure potential method and is therefore basically linear. However, non-linear effects associated with finite axial induction and blade vortex flow are included via approximate methods. Acoustic topics include radiation of noise caused by blade thickness, steady loading (including vortex lift), and unsteady loading. Shielding of the fuselage by its boundary layer and the wing are treated in separate analyses that are compatible but not integrated with the aeroacoustic theory for rotating blades. The report is in 5 volumes with titles and contractor report numbers as follows.

Volume I. "Development of Theory for Blade Loading, Wakes, and Noise", (CR 4329)
Volume II. "Development of Theory for Wing Shielding", (CR 185192)
Volume III. "Application of Theory for Blade Loading, Wakes, Noise, and Wing Shielding", (CR 185193)
Volume IV. "Computer User's Manual for UAAP Turboprop Aeroacoustic Code" (CR 185194)
Volume V. "Propagation of Propeller Tone Noise Through a Fuselage Boundary Layer", (CR 185195)

17. Key Words (Suggested by Author(s))	18. Distribution Statement
Prop-Fan, High Speed Turboprop, Aerodynamics, Noise, Acoustic Shielding, Vortex Lift, Unsteady Lift, Wakes	General release

19. Security Classif. (of this report)	20. Security Classif. (of this page)	21. No of pages	22. Price*
Unclassified	Unclassified	124	

NASA FORM 1626 OCT 86

*For sale by the National Technical Information Service, Springfield, Virginia 22161